FINAL REPORT

DEVELOPMENT OF TENDON IMAGING SENSOR

FDOT Contract Number: BDV25-977-24
USF Contract Number: 2104 1245 00

Report Prepared by:

Hani Freij
David Dukeman
Alberto A. Sagüés
Christopher Alexander

Department of Civil and Environmental Engineering

Tampa, FL 33620
August, 2019

DISCLAIMER

The opinions, findings, and conclusions expressed in this publication are those of the author(s) and not necessarily those of the Florida Department of Transportation or the U.S. Department of Transportation.

UNIVERSAL CONVERSION TABLE

SI* (MODERN METRIC) CONVERSION FACTORS

APPROXIMATE CONVERSIONS TO SI UNITS					APPROXIMATE CONVERSIONS FROM SI UNITS				
SYMBOL	WHEN YOU KNOW	MULTIPLY BY	TO FIND	SYMBOL	SYMBOL	WHEN YOU KNOW	MULTIPLY BY	TO FIND	SYMBOL
		LENGTH					**LENGTH**		
in	inches	25.4	millimeters	mm	mm	millimeters	0.039	inches	in
ft	feet	0.305	meters	m	m	meters	3.28	feet	ft
yd	yards	0.914	meters	m	m	meters	1.09	yards	yd
mi	miles	1.61	kilometers	km	km	kilometers	0.621	miles	mi
		AREA					**AREA**		
in^2	square inches	645.2	square millimeters	mm^2	mm^2	square millimeters	0.0016	square inches	in^2
ft^2	square feet	0.093	square meters	m^2	m^2	square meters	10.764	square feet	ft^2
yd^2	square yard	0.836	square meters	m^2	m^2	square meters	1.195	square yards	yd^2
ac	acres	0.405	hectares	ha	ha	hectares	2.47	acres	ac
mi^2	square miles	2.59	square kilometers	km^2	km^2	square kilometers	0.386	square miles	mi^2
		VOLUME					**VOLUME**		
fl oz	fluid ounces	29.57	milliliters	mL	mL	milliliters	0.034	fluid ounces	fl oz
gal	gallons	3.785	liters	L	L	liters	0.264	gallons	gal
ft^3	cubic feet	0.028	cubic meters	m^3	m^3	cubic meters	35.314	cubic feet	ft^3
yd^3	cubic yards	0.765	cubic meters	m^3	m^3	cubic meters	1.307	cubic yards	yd^3
NOTE: volumes greater than 1000 L shall be shown in m^3									
		MASS					**MASS**		
oz	ounces	28.35	grams	g	g	grams	0.035	ounces	oz
lb	pounds	0.454	kilograms	kg	kg	kilograms	2.202	pounds	lb
T	short tons (2000 lb)	0.907	megagrams (or "metric ton")	Mg (or "t")	Mg (or "t")	megagrams (or "metric ton")	1.103	short tons (2000 lb)	T
		TEMPERATURE (exact degrees)					**TEMPERATURE (exact degrees)**		
°F	Fahrenheit	5 (F-32)/9 or (F-32)/1.8	Celsius	°C	°C	Celsius	1.8C+32	Fahrenheit	°F
		ILLUMINATION					**ILLUMINATION**		
fc	foot-candles	10.76	lux	lx	lx	lux	0.0929	foot-candles	fc
fl	foot-Lamberts	3.426	candela/m^2	cd/m^2	cd/m^2	candela/m^2	0.2919	foot-Lamberts	fl
		FORCE and PRESSURE or STRESS					**FORCE and PRESSURE or STRESS**		
lbf	poundforce	4.45	newtons	N	N	newtons	0.225	poundforce	lbf
lbf/in^2	poundforce per square inch	6.89	kilopascals	kPa	kPa	kilopascals	0.145	poundforce per square inch	lbf/in^2

*SI is the symbol for the International System of Units. Appropriate rounding should be made to comply with Section 4 of ASTM E380.

(Revised March 2003)

TECHNICAL REPORT DOCUMENTATION PAGE

1. Report No.	2. Government Accession No.	3. Recipient's Catalog No.
4. Title and Subtitle DEVELOPMENT OF TENDON IMAGING SENSOR		5. Report Date August, 2019
		6. Performing Organization Code
7. Author(s) H. Freij, D. Dukeman, A. Sagüés and C. Alexander		8. Performing Organization Report No.
9. Performing Organization Name and Address Department of Civil and Environmental Engineering University of South Florida (USF) Tampa, FL 33620		10. Work Unit No. (TRAIS)
		11. Contract or Grant No. BDV25-977-24
12. Sponsoring Agency Name and Address Florida Department of Transportation 605 Suwannee St. MS 30 Tallahassee, Florida 32399 (850)414-4615		13. Type of Report and Period Covered Final Report 01/01/2016 - 08/30/2019
		14. Sponsoring Agency Code
15. Supplementary Notes		

16. Abstract: Inadequate grouting is associated with corrosion of post-tensioning steel in grouted tendons used in construction applications. This project was conducted to develop a nondestructive method capable of economical, rapid imaging assessment of grout deficiencies of external tendons in the FDOT structural inventory. The method uses electrical impedance measurements by means of a traveling sensor placed on the outer surface of the tendon duct, combined with a magnetic detection method that determines the envelope of the strand bundle in the cross-section of the tendon. Integration of strand position and impedance information was processed to produce a color-coded image of the tendon cross-section that distinctly flags the presence of a full void and provides immediate visual differentiation between sound and deficient grout locations. Other void configurations and regions of unhydrated grout produced a signature pattern intermediate between that of full voids and sound grout. Regions with a higher water content resulted in lower impedance values than those observed with sound grout. Those cases were flagged with proper independent calibration. Tests for validation of the method against gamma ray tomography scans confirmed the ability of the method to reveal the presence of full voids in an image that includes strand position information.

17. Keywords Detection and identification; Electromagnetic properties; Grouting; Image processing; Posttensioning; Sensors; Tendons (Materials).		18. Distribution Statement No Restriction This report is available to the public through the NTIS, Springfield, VA 22161	
19. Security Classif. (of this report) Unclassified	20. Security Classif. (of this page) Unclassified	21. No. of Pages: 142	22. Price

ACKNOWLEDGEMENT / NOTICE

EXECUTIVE SUMMARY

Inadequate grouting has been found to be associated with corrosion of post-tensioning steel in grouted tendons used in construction applications. Local grouting deficiencies include voids where bleed water existed and was later reabsorbed elsewhere or evaporated, regions of chalky low-strength grout, and regions where excessive water content or even free water is present. As tendons are critical structural components, it is important to detect those deficiencies during inspection of bridges in place or under construction. This project was conducted to develop a nondestructive method capable of economical, rapid assessment of grout deficiencies of external tendons in the FDOT structural inventory.

The method uses electrical impedance measurements by means of a traveling sensor placed on the outer surface of the tendon duct. For example, grout deficiencies such as voids result in higher impedance than for sound grout, thus providing a defect signature that can be displayed in a cross-sectional image of the tendon, alerting the inspector to that issue. Such signals are however, dependent on the presence and position of the post-tensioning strands within the tendon cross-section. Without knowing the strand positions, the outcome of grout sensing technologies is subject to uncertainty that increases the likelihood of false positives in the detection of grouting irregularities. Instead, knowing the strand distribution in the tendon cross-section can enable the introduction of adjustments to the data produced by the sensor. That permits distinguishing variations of output due to variations in strand placement along the tendon from changes in the output that are genuinely related to grouting anomalies.

Hence, the method developed here consisted of two components. In the first component, the internal distribution of the steel strands within the tendon duct cross-section is imaged by means sensitive to the presence and location of the steel. Once that steel distribution is known, the second component uses that information to interpret the impedance signals descriptive of the grout that is present between the external perimeter of the tendon and the steel. Therefore, this work sought first to develop for field application a non-intrusive method to image strand position inside the cross-section of external post-tensioned tendons and, second, to use imaged strand data to enable improved use of impedance technology for detection of grouting anomalies and their imaging in the tendon cross-section. The approach included review of the technical literature and design and construction of a strand position imaging system as well as an impedance detection method, and integration of both procedures in a laboratory demonstration unit. Additional tasks included conducting validation tests of the method created here by comparing with the results of established gamma ray tomography assessments.

As the first outcome, an integrated imaging procedure concept for external tendons was created, consisting of a magnetic strand position imaging base and a simultaneous impedance assessment of condition of the grout in the space between the strand and the inner tendon duct perimeter. The strand position imaging concept was demonstrated with a working prototype that features movable magnetic sensors that quickly obtain reproducible records of acting force as a function of angular position in a manner suitable for image processing. Two consecutive deconvolution procedures for strand position detection were implemented that together resulted in recovery of the strand bundle envelope. The result was validated against the known configuration of the tendon test segments used. An alternative exploratory strand position imaging method was also implemented using standard rebar location equipment, allowing for future development of imaging systems with fewer moving parts.

Review of the technical literature confirmed that admittance/impedance measurements of the duct-strand space held the most promise for successful implementation of the integrated imaging sensor concept. In combination with the magnetic strand position information, impedance measurements reported as a function of rotational angle from a start place clearly identified the presence of voids fully extending from the inner wall of the duct to the strand envelope ("full voids"). The full-void region manifested impedance values that were typically two or more times higher than those of regions of sound grout. Integration of strand position and impedance information was processed to produce a color-coded image of the tendon cross-section that distinctly flagged the presence of the full void and provided immediate visual differentiation between sound and deficient grout locations. Other void configurations and regions of unhydrated grout produced a signature pattern intermediate between that of full voids and sound grout. Full voids filled with water (analogous to high water content "soft grout") resulted in impedance values somewhat lower than those observed with sound grout. The resulting modest differentiation was usable to flag that condition with proper independent calibration.

Computer modeling was implemented to predict the tendon response to impedance measurement excitation via the external sensor at changing angular positions. The model used grout parameters, accurately reproducing experimental measurements for both the sound condition and a void filled with air. Different frequencies and plate configurations were explored and assessed. Operation at 500 MHz showed promise for better grout deficiency detection in future generations of the system. A laboratory prototype was successfully implemented, with collaboration from project BDV25-977-52, Field Demonstration of Tendon Imaging Methods, to produce a graphical color-coded image that displayed grout anomalies on a tendon's cross-section, based on the patterns of differentiation obtained experimentally and with the computer simulations.

Tendon cross-section image information obtained with the Tendon Imaging Unit (TIU) and gamma ray tomography provided a significant extent of validation of the TIU instrument application and by extension, of the relevance of the combined use of strand position and impedance measurements for detection of grouting deficiencies.

As an overall product from this project, a low cost, rapid technology for imaging of cross-section or linear scanning of external post-tensioned tendons has been developed, demonstrated, and made ready for deployment in the field under the activities that were conducted under the concurrent FDOT project BDV25-977-52, Field Demonstration of Tendon Imaging Methods.

TABLE OF CONTENTS

LIST OF FIGURES

LIST OF TABLES

1. BACKGROUND STATEMENT

Inadequate grouting has been found to be associated with corrosion of post-tensioning steel in grouted tendons used in construction applications. Local grouting deficiencies include voids where bleed water existed and was later reabsorbed elsewhere or evaporated, regions of chalky low strength grout [1-3], and regions where excessive water content or even free water is present. In those zones, mechanical bonding of strand to the grout is degraded and, more of concern, the strand steel risks corrosion failure. As tendons are critical structural components, it is important to detect those deficiencies during inspections of existing bridges and, if possible, during the construction phase of new bridges so that early remedial measures can be taken. To that end, it is highly desirable to have an imaging method to identify the presence, size, and location of deficient grout zones in a tendon cross-section. The method would be most useful if it were nondestructive, rapid, and economical as well as accessible to personnel without the need of highly specialized training. That way, the method could be practically applied to structures with large numbers of tendons where specialized and costly procedures would be otherwise prohibitive. The prospect of successful development of such method is much greater for the case of external tendons, where there are no obscuring effects from the reinforced concrete that are present immediately around internal tendons. Since external tendons are widely used in FDOT bridges and have exhibited some of the most notable recent corrosion-related failures, availability of imaging technology, even if initially limited to those tendons, would still represent a major advance in corrosion control.

This project was conducted to develop a test method filling the above requirements of economical, rapid assessment of external tendons in the FDOT structural inventory. The resulting first generation imaging method was selected following analysis of a variety of sensing technologies [4-6] with potential for fast operation without excessive cost or health risks. The choice was electrical impedance measurements by means of a traveling sensor placed on the outer surface of the tendon duct, which showed a promising combination of the desired features. It was understood however, that the identifying grout condition signals obtained externally to the tendon duct, as well as their significance, can be sensitive to the presence and position of the post-tensioning strands within the tendon cross-section.

The strands are not uniformly spaced inside the duct cross-section and tend sometimes to crowd against one of the sides. Crowding however, varies along the tendon depending on the proximity to deviation blocks, the way in which the strands were threaded during initial placement at the time of construction, and deviations from a straight cylindrical shape of the duct itself as produced or due to gravity deflection. Detecting that changing pattern will enable creating a more accurate 2D image of the cross-section that can show where the steel strand envelope lies and an appropriate size of a deficiency, if present in the grout space. That information reduces the likelihood of false positives in the detection of grouting irregularities. Moreover, the significance of a detected anomaly can be better assessed depending on whether it concerns a large space of grout between the tendon duct and the steel or, instead, only a thin intervening grout space.

Hence, the method developed here consisted of two components. In the first component, the internal distribution of the steel strands within the tendon duct cross-section is imaged by means sensitive to the presence and location of the steel. The second component uses that information to interpret the impedance signals descriptive of the grout that is present between the external perimeter of the tendon and the steel, and a complete cross-section image is then created.

2. PROJECT OBJECTIVES

Based on the above, an investigation was conducted with the following objectives:

- Develop for field application a non-intrusive method to image strand position inside the cross-section of external post-tensioned tendons.

- Use imaged strand data to enable improved use of impedance technology for detection of grouting anomalies and their imaging in the tendon cross-section. Produce a laboratory prototype.

The objectives were addressed by i) examination of the prior literature to select an appropriate grout assessment technology – eventually chosen to be an electrical impedance method - to supplement the strand position information, ii) development of a strand position imaging prototype, iii) development of an impedance grout assessment method, iv) integration of both methods in a laboratory prototype and v) validation with gamma ray tomography comparisons.

The findings are detailed in the following report sections keyed to each of the above items.

3. LITERATURE REVIEW

<u>Objective</u>

This review seeks to identify and select an appropriate grout assessment technology to complement strand position information in the tendon imaging method. The strand position detection method is addressed in the next chapter of this report.

<u>Categories</u>

While the main objective of this investigation was the development of a tendon imaging method, for completeness this review includes as well general techniques for nondestructive examination of post-tensioned tendons.

Some recent excellent reviews of tendon NDT methods are available, typified by the 2012 report for the FDOT-sponsored project BDK80 977-13 by Azizinamini [4,5]. The authors of that report classify the methods in the following categories, which serve as a convenient roadmap to discuss the material relevant to the present review:

1.   Visual
2.   Magnetic
3.   Mechanical wave/vibration
4.   Electromagnetic wave
5.   Electrochemical
6.   Penetrating radiation

Comparable recent survey information of several of those methods can be found for example in work by Im [6,7] and Iyer [8]. In the following, each of these aspects is considered to select an appropriate grout assessment technology to supplement strand position information.

Note: This review was prepared early during the project execution. Other sources of interest have been published in the interim and are addressed in an update statement at the end of this chapter.

Visual

Visual methods are usually standard examination procedures either by direct inspection or aided by video cameras (including robotic and remote manipulation) which should for the external tendon duct surface normally precede any internal tendon imaging examination. Internal examination of the tendon at accessible points such as in borescope viewing at anchorages are likewise well established; hence these methods will not be further discussed here.

Magnetic

Magnetic methods have traditionally been associated with the detection of corroded strand portions where the metallic state of the strand has been converted into an oxide with usually lower magnetic permeability. This gives rise to irregularities in the magnetic field as an exciting coil passes over that part of the tendon (magnetic flux leakage method), or to irregularities in the residual magnetic field of a previously magnetized strand assembly, or

similar variations thereof [9,10]. While these methods could conceivably be further developed to eventually construct an image of the tendon interior including grout condition, such progress does not appear to be a likely occurrence in the near future. This is especially so, as the magnetic response of the grout itself, which has magnetic susceptibility that is orders of magnitude smaller than that of the steel [11], is likely to be overwhelmed by the presence of the latter.

Magnetic strand corrosion detection methods should not be confused with the magnetic strand location method developed under this project. The latter is not optimized for or easily capable of detecting small strand irregularities; it simply finds strand location under the assumption that much of the metal is not heavily corroded. Conceivably however if there is a segment of the tendon where some of the strands have suffered extensive section loss, with associated loss of attractive force compared with zones on either side of the affected zone, the magnetic location method might provide an additional indication of anomalous behavior by comparison with the strand location image of the adjacent tendon zones. Comparable supplemental indications might be provided as well if the Alternative Exploratory Method using inductance signals (see Part 4 of this report) is used instead.

Mechanical wave/vibration

Mechanical wave and vibration methods can be divided into large scale whole-tendon segment methods and detailed local methods. The first are illustrated by full scale tendon vibration procedures such as those developed by the P.I. [12,13]. In those techniques the entire free length of an external tendon segment is made or allowed to vibrate and the vibration spectrum is analyzed to determine natural modes, and from those the state of tension of the tendon can be inferred. Comparison of the tension of segments on either side of a deviation block, or with a group of comparison peer tendons, can easily reveal deficient tendon segments where the tension is significantly lower than elsewhere, thus flagging those segments for detailed examination including imaging techniques such as those concerned in this project.

Detailed local mechanical examination methods use mechanical waves, ranging from simple manual hammer tapping on the external duct surface to reveal audible indications of voids or other local deficiencies, to more sophisticated impact-echo spectral analysis of the local tendon response to controlled small impacts, to ultrasonic imaging using multiple sensors and excitation point arrays. These techniques have been described already in Ref. [4] and in other surveys [6,7] and specialized studies [14] so reference is made to those sources for details. Application of those methods specifically for imaging of the cross-section of the tendon has been explored to some extent. Earlier work by Iyer [8] with ultrasonic C-scan imaging showed promising results with simplified mockups, and a more extensive 2008 investigation by Krause [15] using ultrasonic echo and specialized processing was able to provide glimpses of the tendon interior even for tendons embedded in concrete, with independent validation from gamma ray imaging. Given these encouraging but still limited results, the use of ultrasonic echo will be examined in detail in the next phase of this project to assess whether, if combined with more precise strand position knowledge, it can allow for sufficient use for determination of grout deficiency locations. As noted in [4] and elsewhere, ultrasonic methods have also been used in attempts to detect corroded locations on individual wires of strands with ends that are accessible at the anchorage, and acoustic emission is also used for detection of strand breakage events. Those two methods however are of limited application for imaging applications of the type addressed by this project and are mentioned here mainly for completeness.

Electromagnetic wave

This broad category includes thermal detection methods as well as those based on dielectric behavior measurements and radar/microwave examinations.

For thermal methods, a very recent review by Milovanovic [16] examines IR thermography for detection and assessment of defects in reinforced concrete, specifically for active IR thermography where the component to be assessed is subject to a momentary thermal load and the subsequently evolving surface temperature map is analyzed to recover the features hidden underneath. Application of infrared thermography to detect grouting defects in tendons has been examined in some detail by Pollock [17] for the challenging case of embedded internal tendons, where detection of grouting voids was reasonably successful for tendons embedded under relatively low concrete covers. The technique appears to be highly promising for application in this project using a traveling thermal excitation source along the exterior of the tendon, as prior knowledge of strand position (enabled by the outcome of this project task) in the external tendons of concern would significantly reduce uncertainty in the interpretation of the results. The method would thus have potential to distinguish between a sound location, a void, or intermediate conditions of grout deficiency. The review in [16] notes the recent development of sophisticated data processing techniques for analysis of the thermal surface data, and application of such data processing methods was given consideration as well in this project, however, it was not chosen to be used as the GS method.

Methods involving electromagnetic measurements associated with determination of dielectric and ionic conductive behavior of the interior of the tendon are among the most encouraging for application in the present project. In its simplest form the measurements can be conducted with a traveling external electrode (or array thereof) on the external surface of the concrete, and determination of the (mostly dielectric) impedance between that electrode and the usually grounded strand assembly would be obtained. The impedance can be obtained over a wide range of frequencies using methods and equipment easily adaptable from electrochemical impedance spectroscopy (EIS) methodology, thus allowing, in the absence of voids, to differentiate between the otherwise dominant capacitive contribution of the polymeric duct and that of the smaller amount associated with the grout itself and its sound or deficient condition. Differentiation is more straightforward when attempting to detect voids given their much greater associated impedance. In all cases, the knowledge of the strand position and associated distance between inside of duct and strand surface using the method developed in this project task is anticipated to significantly reduce uncertainty in the interpretation of the data. Utilization of dielectric/ionic response measurements benefits from extensive literature on the impedance behavior of cementitious materials [18,19], developments in impedance tomography of concrete [20], capacitance measurements to ascertain degree of insulation in European tendon isolation practice [21], numerous preexisting treatments of relevant capacitive and impedance tomography [e.g., 20, 22-28], and increasing interest in the development of traveling sensors for tendons [24]. Consequently, an impedance based method was chosen for implementation in the product developed under this research project.

Ground Penetrating Radar (GPR) /microwave examination methods have been in extensive use for assessment of reinforced concrete [16] and to some extent for detection of tendon positions and internal deficiencies in internal tendons [17]. For the imaging application in this project GPR-related methods were given some consideration but effectiveness, cost, and reliability of this methodology led to decide in favor of an impedance based method.

Electrochemical

In a limited context, electrochemical methods involve assessment of the interface between the strand surface and the surrounding grout. That can be done by measurement of the potential across that interface with or without an intentional disturbance. The first (no disturbance) consists usually of observational half-cell potential or electrochemical noise measurements, which are normally made necessitating contact of an electrode with the grout, following well-established procedures as shown by Taveira [29-31]. The second (intentional disturbance) involves excitation of the interface by means of a transient current as in conventional polarization resistance or EIS measurements [29,31] which can yield information on the rate of corrosion of the steel. However, conventional application of those methods requires either access to (or usual limitation of information to) the anchorage region of the tendon, or breaches of the polymer duct wall to allow for electrodes to be inserted in contact with the grout of the tendon. Hence applicability to the fast imaging outcome sought in this project does not appear to be straightforward.

It might be worthwhile, however, to examine in the future the possibility of conducting vibrating Kelvin Probe (KP) [32,33] measurements of the potential present just outside the polymer duct surface. Those measurements are contactless to that surface (a grounding wire is needed to connect to the strand bundle, but that would present no practical limitation) and could in principle provide an indication of the steel-grout interface potential in the manner of evaluations used to detect undercoating corrosion in coated steel corrosion. In principle, a macroscopic vibrating KP running sensor of the type recently developed by Sagüés [33] for reinforced concrete could be adapted to sample the external surface of the tendon duct, indicating corrosion potential and hence giving information as a function of position along the tendon length on whether the embedded strand is experiencing corrosion. The sensor uses a vibrating disk placed on close proximity but not touching the external duct surface and can be fabricated using available technology [33]. However, that application would involve the challenge of thoroughly neutralizing static electric charges on the duct surface, a task for which feasibility has not yet been demonstrated. Further examination of this alternative should take place in future studies.

Penetrating Radiation

The main techniques under this classification are traditional X-Ray radiography (and associated X-Ray computerized tomography) and Gamma Ray radiography/tomography. The former has been well established and can produce usable images of the tendon cross-section [6] but is outside the scope of the present investigation on account of the expected associated cost, potentially slow implementation, and limited ease of implementation. Gamma ray methods have been less widely implemented than X-Ray methods but have shown greater potential for accurate and sensitive imaging of post-tensioned tendons [15, 34-37]. Due to its cost and complexity, Gamma ray inspection falls likewise outside of the scope of this work, but because of its desirable features it have been selected for conducting limited validation tests as described in chapter 7.

Selection of grout assessment technology

From the above review, electromagnetic wave coupling methods that measure the impedance between an external plate and the steel strand envelope within were deemed to have the most prospects for success and were selected for implementation in this project. The selection was made in the context of supplementing the strand position imaging methodology that was developed as described in the next chapter.

<u>Update</u>

Since the preparation of the above review in the early stages of the present project, investigations then in progress have been since published providing additional insight on the methodologies discussed above. Notably, an NCHRP-sponsored investigation [37] and associated inspection guidelines documentation [38] examined the relative technical and economic factors of a number of nondestructive examination (NDE) methods as they apply to detection of corrosion and grout deficiencies in post-tensioned tendons. The methodologies examined (penetrating radiation methods not discussed here) were

       a) Ground Penetrating Radar (GPR)
       b) Infrared Thermography (IRT)
       c) Electrical Capacitance Tomography (ECT)
       d) Magnetic Flux Leakage (MFL)
       e) Magnetic Main Flux Method- Solenoid (MMFM)
       f) Impact Echo (IE)
       g) Ultrasonic Tomography (UST)
       h) Ultrasonic Echo (USE)
       i) Sonic/Ultrasonic Pulse Velocity (SPV/UPV)
       j) Low Frequency Ultrasound (LFUT)
       k) Sounding (Sound) by hammer impact
       l) Electrochemical Impedance Spectroscopy (EIS)

Some of those methods were oriented to evaluation of the strand corrosion condition and less so, or not at all, for grout condition evaluation. Figure 3.1 has been prepared based on data developed in that investigation, which evaluated the suitability of each method for detecting grout deficiencies, air voids, and excessive water conditions in polymer-ducted external tendons. The method appropriateness for each case was ranked in a 0-10 scale (10 best) based on how accurately the location and the severity of each condition was detected. It is important to note that those rankings do not include the ability of a given method to differentiate between the various deficiencies. For example, sounding provides an alert that either a void or water is present, but not an indication of which of the two it is. Those rankings indicate nevertheless that for the present analysis only a comparison set of methods GPR, IRT, ECT, IE, LFUT and Sounding merits consideration as the other methods received zero ranking.

Because of its recent development, direct performance comparison of the method developed in this project with the other ranked methods under the same conditions in the NCHRP study was not conducted. However, based on the results presented in subsequent chapters of this report, it is estimated that FTIU would have received a high ranking for both location and severity of void detection, with possibly a medium ranking for detection of deficient grout and water (as well as for ability to distinguish between voids and water, not addressed in the chart) if appropriate calibration were possible as discussed in the final report for Project BDV25-977-52, Field Demonstration of Tendon Imaging Methods [39]. Of the comparison set methods ECT was the closest to the technology developed here as it uses electrical impedance [28] for grout deficiency detection. ECT however scored modestly in deficiency characterization. The other methods scored variously, interestingly with the least sophisticated, hammer sounding obtaining one of the highest combined ratings. None of those methods however provided a detailed image of the tendon cross-section, which as noted in the Introduction chapter would have provided highly valuable insight in the interpretation of the data obtained. In some of those methods, especially those that use an axial traveling sensor, that information could be obtained by the addition of a strand envelope imaging ring as that developed in the present project, and integration of the result of the method and strand position into an imaging

scheme also as that developed here.

Elsewhere impedance based applications are receiving increasing attention, including boundary detection technology [40] and other practical use of traveling capacitance sensors [41].
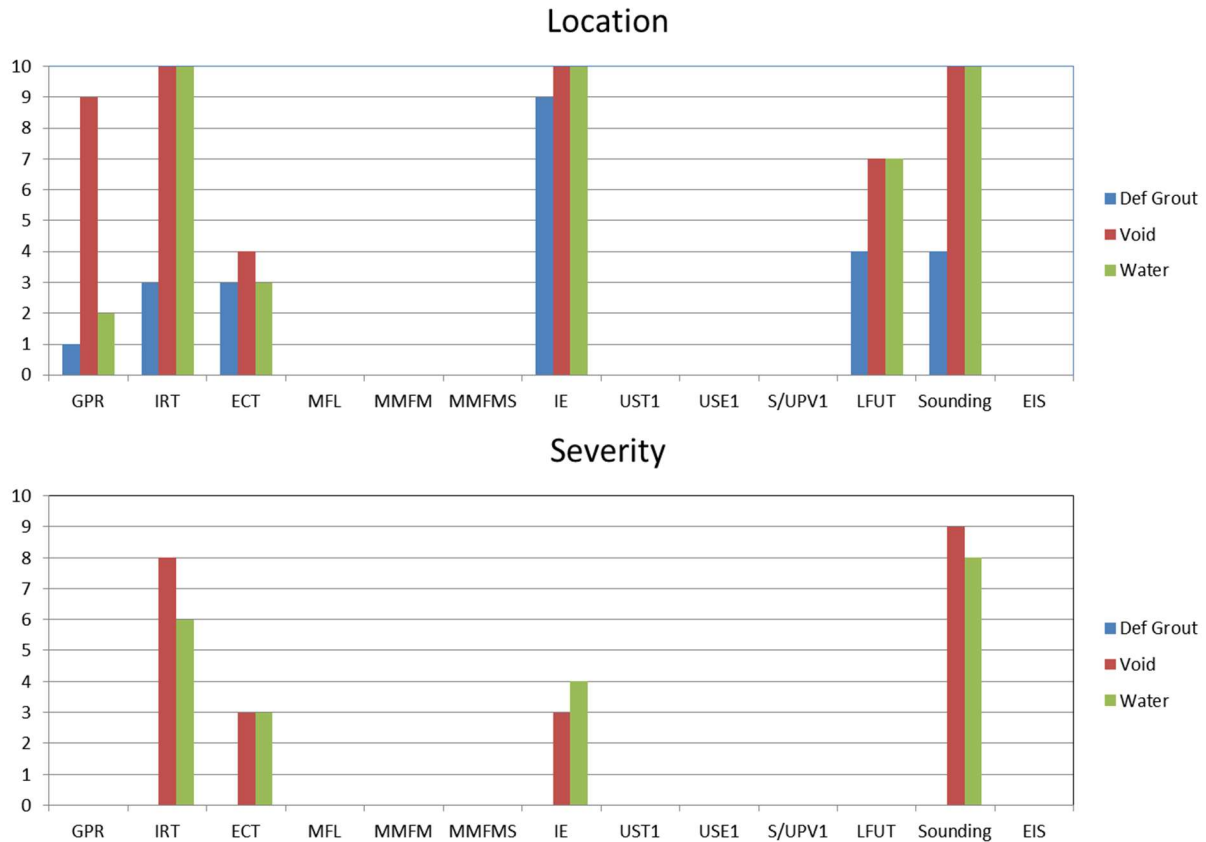
Location

Severity

Figure 3.1 Summary of rankings (10 is best) from the NCHRP investigation [33] for ability of methods to identify location and severity of grout deficiencies, air voids, and excessive water conditions. This summary applies only to evaluation of external, polymer-duct tendons.

Chapter Summary:.

Review of the literature, including an update of recent findings, supported the choice of combined magnetic strand cross-section envelope determination with electrical impedance measurements, for a rapid and economical tendon imaging method to reveal grouting deficiencies.

4. STRAND POSITION IMAGING PROTOTYPE

<u>Design</u>

Overall approach

To achieve the main project objective of developing an economical, fast and easy to operate technology, the imaging process was configured in the form of two complementary steps. First, the position of the strands in the tendon cross-section is obtained by a simple and fast method. Second, the strand position information is used as a basis for reliable implementation of a grout condition evaluation method, selected in the previous chapter as based on impedance to obtain dielectric signatures of grout deficiencies. Prior knowledge of strand position enables faster and more reliable implementation of the second step, which would otherwise incur considerable uncertainty because of lack of direct information on the amount and dimensions of the space present beneath the sensing footprint. Thus, the second step could more reliably differentiate between, for example, a narrow grout space with undesirably low density versus a thicker, normal density space. The two step approach was therefore chosen as a highly promising shortcut to achieve the project objectives. The device presented in this chapter provides the strand position detection functionality necessary for the first step.

Principle of operation

The principle of operation is described in detail in a U.S. patent document [42] so only a brief summary is presented here. In its basic implementation (Figure 4.1) the strand position sensor is a magnet (or array of magnets) fitted with a transducer that measures the attractive force between the magnet/array and the strands.
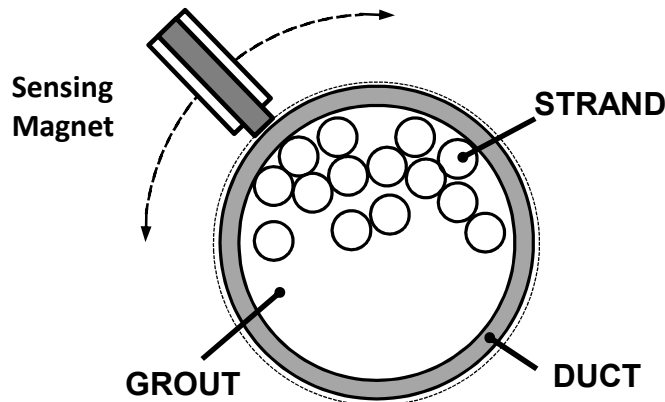
Figure 4.1 Strand arrangement and basic implementation for this method [42].

The sensor is placed in a ring that is made to hug the perimeter of the duct. The ring, or an internal part of it attached to the sensor, is rotated successively so that it covers by itself, or in concert with similar sensors rotating elsewhere in the ring, the entire perimeter of the duct at a given location on the duct longitudinal coordinate. The ring is then displaced successively along various longitudinal positions on the tendon, thus sampling the entire tendon length or

selected parts of it. Rotation and displacement are accomplished by means of manual or motorized motion. For a given longitudinal position in the tendon, the output of the rotational scan is a vector of values of attractive force at successive angular positions. For example, if force is recorded at 1-degree intervals, a vector with 360 values is obtained. The measurement can be performed rapidly and reproducibly. From the vector values, and from knowledge of the strand size, number of strands, and duct wall thickness used for the tendon construction, an indication of the strand layout on each cross-section sampled is then obtained by appropriate deconvolution.

The deconvolution can be done by procedures of various degrees of sophistication, depending on the need for accuracy in strand position determination. In its simplest form, use is made of the observation that for a single short magnet with a field that approaches that of a simple magnetic dipole, the force between a single strand and the magnet follows a high (e.g., 4th) power inverse dependence on the distance between the magnet and the strand. The force vector is then converted into a distance vector, which when displayed in a radial plot yields an indication of the envelope of the strand bundle in the duct cross-section. The precise value of the power-law exponent (n) can be refined by calibration against information from test specimens with known strand configurations.

This principle of operation was embodied in the system that was developed here and is presented subsequently.

Configuration chosen [42].

The system was built to fit tendon segments that were available in the laboratory, but it is emphasized that this choice is not limiting and device sizes to fit larger tendons can be readily implemented. The tendon segments used are from 12-strand tendons constructed and tested in the former FDOT project BC353-44; detailed information is provided in Ref. [13]. The tendon was built with a polyethylene duct of 3.5 in average external diameter and 0.215 in average wall thickness. The ½ inch strands meet ASTM A 416 and are fully embedded in grout. While the strands were distributed evenly at the anchor ends, placement within the cross-section of the tendon segments tested varied from even to strongly lopsided depending on proximity to the bend that existed at a deviation block. Thus, these segments offered an excellent opportunity to assess the performance of the device under various degrees of strand placement non-uniformity.

The prototype sensor was built approximately following the configuration schematically illustrated in cross-section in Figure 4.2. There the sensor is placed around the tendon to be imaged, consisting of duct D which contains multiple strands S and grout G (which may be sound or contain deficiencies) filling the remaining space. The key elements of the sensor are subassemblies each containing a magnet 1 held at a distance h from the external duct surface by means of a magnet carriage 4 that rides on wheels 3 and is held in place against the duct by an arrangement of studs 7 and springs 8. Those permit the magnet carriage to move radially following any irregularities in the roundness of the duct D, while maintaining a fixed azimuth position with respect to the main sensor ring 9 which rotates around the tendon and causes the wheeled magnet carriages to rotate with the ring 9. Ring 9 for this prototype was built as a solid ring as it is simply inserted at one end of the laboratory test tendon pieces. For implementation in the field, the ring will be a multi-part piece for placement around the tendon, with the parts reunited via a combination of hinges and/or assembly braces. For the present realization which contained two subassemblies located at opposite sides of the tendon, the ring is rotated around the tendon by hand in a back and forth, 180-degrees clockwise and counterclockwise manner so that the footprint of the magnets each cover one half of tendon perimeter, thus covering the

equivalent of one entire rotation around the tendon duct perimeter. Laboratory prototypes presented in Chapter 6 of this report use only one magnet to better accommodate the complementary impedance instrumentation in one compact demonstration package. The dual magnet embodiment is nevertheless implemented in this section with a view to demonstration and future development of more efficient systems.

The radial force acting on each magnet due to attraction to the strands and to the radial component on the weight of the magnet is sensed by transducer 2 and continuously transmitted via cable 5 to the signal processing unit 6.
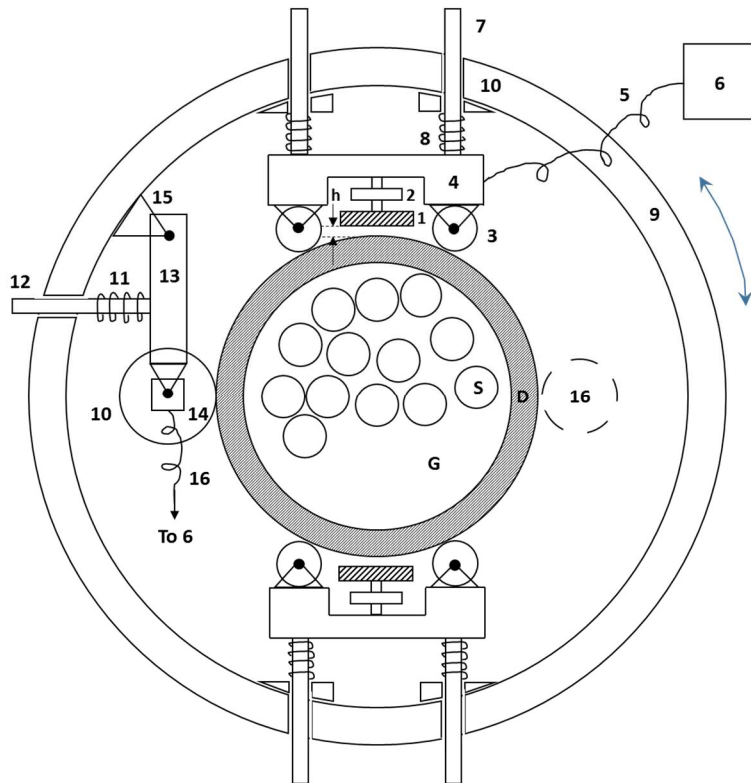
Figure 4.2 Approximate prototype configuration. The bottom carriage shares the same part designations (omitted for simplicity) as the upper carriage. [42].

A freely rotating wheel 10 covered with soft rubber coating and contacting the surface of the duct, pressed against it by a lever 13, support 15, spring 11 and stud 12, has an axial position transducer 14 that communicates with cable 16 to signal processing unit 6. The signal thus encoded provides a running numeric indication of the radial position of the magnet carriages as they turn around the tendon. That numeric position indication is continuously stored in the signal processing unit 6 together with the force indications from both magnets, as well as a time stamp. In the present embodiment, acquisition of those data takes place approximately 10 times per second, and time for a hand-actuated one-half rotation is in the order of 5-10 seconds, but those choices are not limiting and faster rotations are feasible.

An additional wheel or wheels 16 can be introduced to ensure that while rotating, the center of the main ring 9 is approximately coinciding with the centerline of the tendon, therefore limiting the span of motion that is accommodated by studs 7 and 12 and springs 8 and 11. Moreover, hand operation can be readily replaced by a motorized system that uses wheel or

wheels 16 for propelling the back and forth motion. Likewise, increasing the number of magnet carriages and magnets can be readily implemented to reduce the extent of needed rotation to cover the duct perimeter and hence reducing measurement time.

Cables 5 and 16 do not interfere with the back and forth rotation motion. The processing unit 6 is, in the present implementation, a pair of small electronic control boards adjacent or attached to the ring 9, and those boards are connected to a laptop computer via a USB cable. However, there is no limitation in implementing a wireless scheme e.g., by a Bluetooth® protocol, so that the control boards (as well as any rotation motor) can be battery operated and the entire sensor communicates with computer without the need of cables. Ring 9 is in the present embodiment a Plexiglas® tube section approximately 2 inches long. To sample various locations of the tendon the ring is moved by hand from one location to the next, but there is no limitation of attaching the ring to a battery operated motor so the unit can crawl over the length of tendon to be examined and automatically sample consecutive locations, thus providing a three-dimensional indication of strand locations on the entire external portion of the tendon.

The raw output of the measurement at a given location is a profile of force acting on each of the magnets, and of angular position of each magnet with respect to a predefined starting angle, as a function of time of acquisition. The component of the force due to magnet weight is a known function of angular position and the mass of the magnet, and is readily subtracted from the total force by calculation. A similar subtraction can be made for any equivalent inertial force on the magnet resulting from rotational motion if it is rapid enough to be significant.

Construction

Physical implementation is shown in Figure 4.3. For simplicity, operational trials were made on vertically placed tendon segments, so as to avoid need for magnet weight corrections given that in this case the weight is perpendicular to the magnetic force and it is not reflected in the transducer reading. A gravity-force correction feature will be built into future versions of prototype software. The tendon segments used were ~ 12 in long, and the sampled region was near the center of the segment.

The magnet-duct gap h was approximately 2 mm and the wheel-to-wheel contact distance was approximately 50 mm. With those dimensions the subassemblies were able to travel over the entire tendon perimeter without contact between magnet and duct, despite slight departures from ideal circular perimeter in the tendons evaluated.
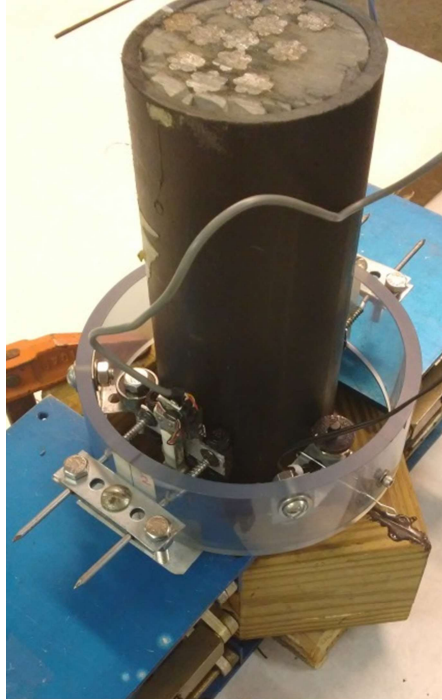
Figure 4.3 Initial physical implementation [42].

The magnets were ceramic disks with a magnetic moment in the order of 0.34 A-m^2, and the force transducers were of a modified cantilever miniature type with ~1 N a maximum force capacity, which was about one order of magnitude higher than the largest expected forces in the system, while still providing reading precision in the order of 1% for those high force levels. The combination magnet and sensor was calibrated with known weights to obtain a conversion constant for translation of signal levels to force. The angular position transducer provided sub-mm precision readings of wheel contact position on the perimeter, yielding angular readings with better than 1-degree resolution.

Operation

The prototype sensor acquired data reliably and reproducibly. Figure 4.4 illustrates graphically the raw output of a measurement conducted with the prototype placed near the center of a short (~12 inch long) tendon segment. In these examples the rotation was carried out for a full 360° back and forth cycle, to produce additional data that served to calibrate one magnet output against the other. For subsequent regular operation only a 180° cycle is used. The tabular data consists of lines each with a time stamp, reading of indication of force acting on the magnet in Carriage 1 (Force 1), reading for Carriage 2 (Force 2), and reading of position sensor converted into rotation degrees starting from a reference mark. The mark corresponded typically to the point of highest elevation on the duct perimeter of the tendon when it was put in service. The results of the force-related readings as well as the position readings are plotted as a function of the time from the start of the hand-operated rotation cycle.
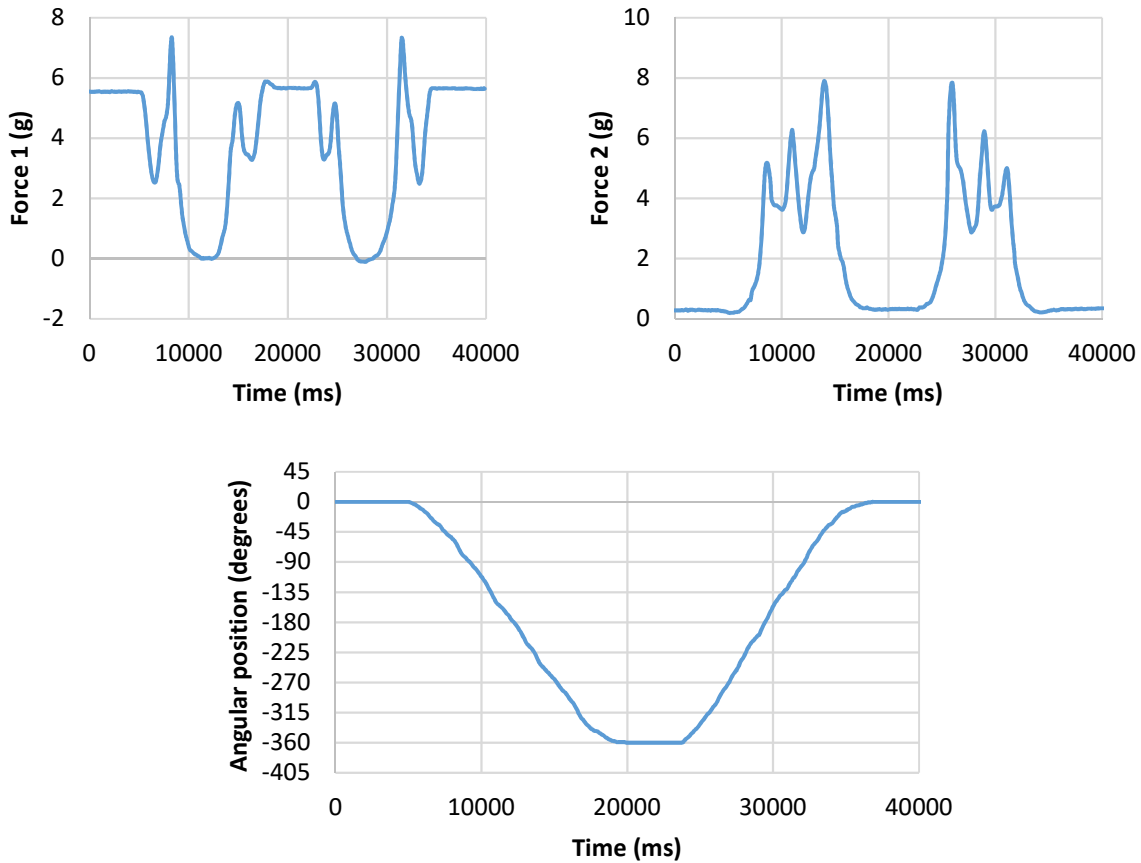
Figure 4.4 The upper two graphs show the two sensor outputs for each carriage, where Force 1 and Force 2 (in gram-force) are plotted versus time. The variation of forces as a function of position on the tendon duct perimeter reflects variations on how far the steel strand envelope is beneath each position. The lower graph shows the angular position versus time as the run is being conducted.

The peaks in the force-related plots correspond to moments where the magnet rotated above a strand that was closer than the rest to the inner perimeter of the duct, thus resulting in greater attractive force. The lowest values correspond to regions where the steel was farthest from the magnet. Each 360° rotation took in the order of 20 seconds, for a total of ~40 seconds total acquisition time.

Figure 4.5 illustrates reliability and reproducibility of the results, showing a high degree of similarity between the peaks and troughs in each run.

14
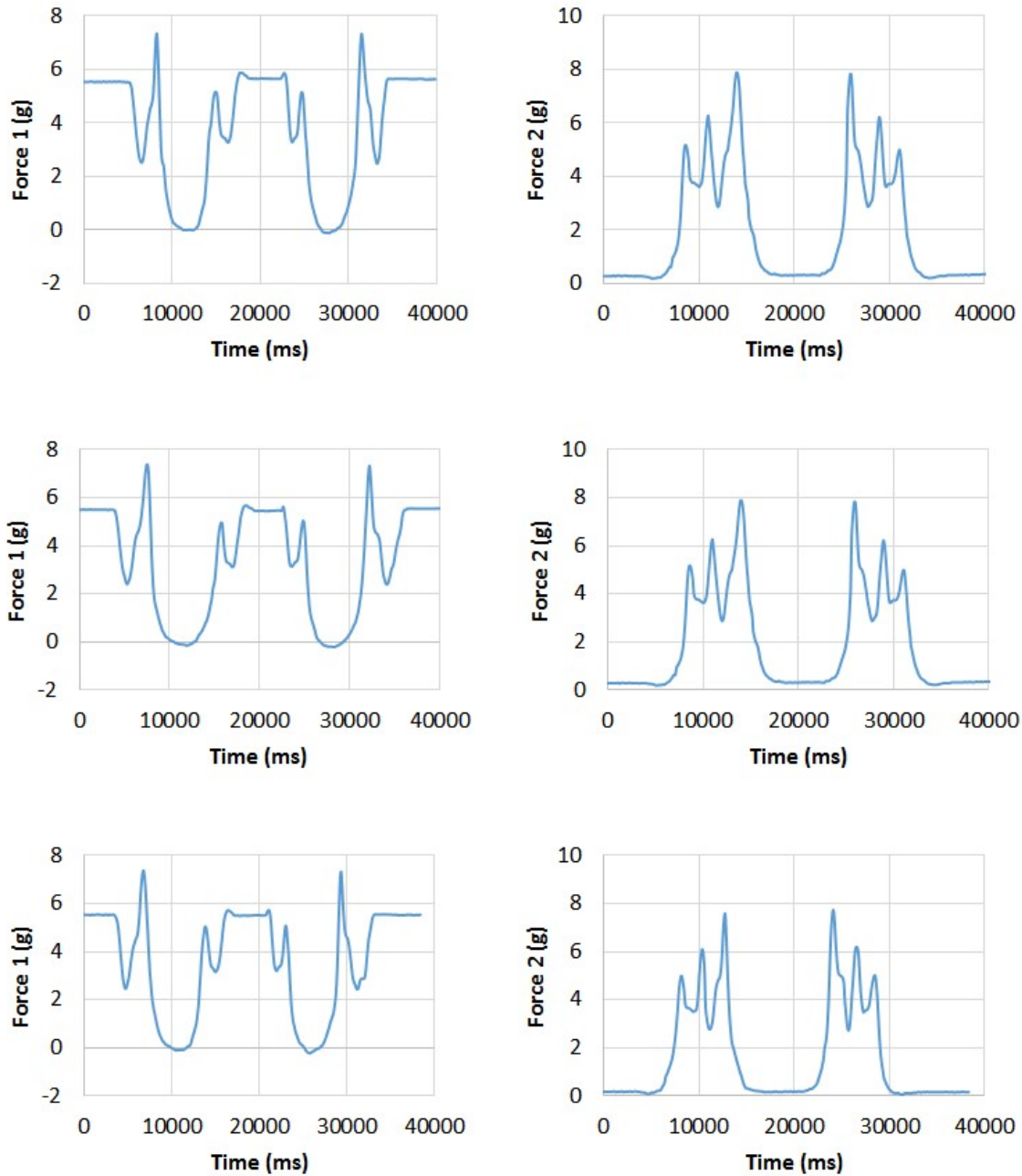
Figure 4.5 Example of three replicate runs performed on the same tendon duct.

Additional measurements were made with the carriages separated from the assembly to determine characteristic response of the force measuring system to a sudden change in force. These tests quantified the response of the system to a step excitation, information necessary for the deconvolution signal processing detailed in a subsequent section. The measurements consisted first of placing an 8-in long ½ in tendon strand segment perpendicular to the magnet axis and at a mutual surface-to-surface distance of approximately 1 cm. After the resulting force reading stabilized, the strand segment was suddenly distanced from the magnet (distance typically changing from ~1cm to >10 cm in <1/10 sec). Figure 4.6 exemplifies the result of one

of those tests; analysis of the result and application to deconvolution of the data are detailed later.

The unit step response for the subassembly, A(t) is calculated from the data as the value F/Fmax as a function of time passed from the moment the force step was applied.
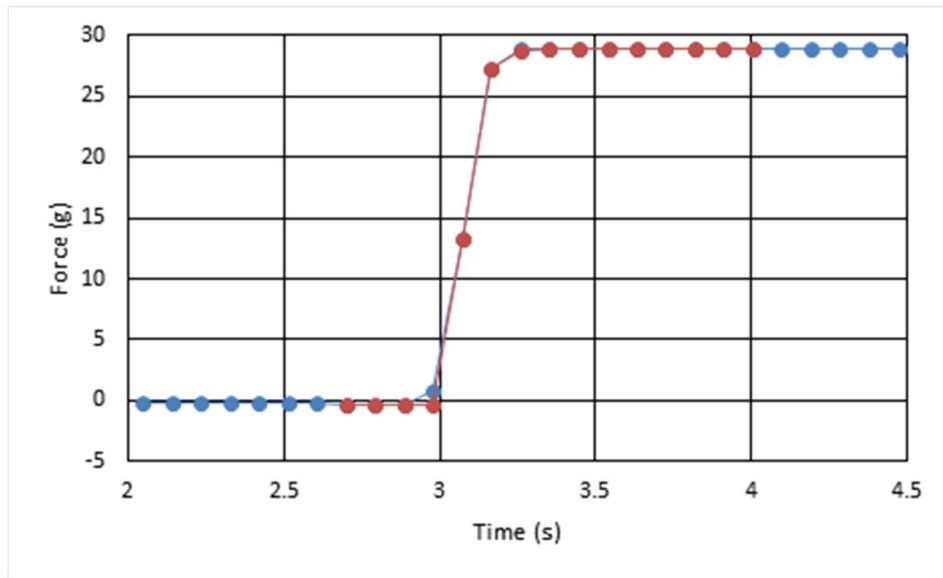
Figure 4.6 Response of the force sensor to a step change in force acting on the sensor. The response is auto-zeroed at the start and converted into a positive number after step application. In this example, the step took place at ~3 seconds after start of data acquisition, and the force change was ~29 gram-force. Red symbols and line show fit to the response per Part 3, with characterizing stabilization time τ~ 0.041 s.

<u>Alternative Exploratory Method</u>

As noted elsewhere [42], strand positioning information can be obtained by alternative procedures using, for example, inductance changes (related to changes in overall magnetic flux in a system) akin to commonly used rebar location instrumentation. For examination of this concept exploratory measurements were conducted by adapting a James Instruments, Inc. Model C-4956 R-Meter® with a custom non-conductive clamp so that, as it rotated, the meter sensor was kept parallel to the longitudinal axis of the tendon with the two magnetic sensing heads, which are typically in contact with the external reinforced concrete surface but were instead kept separated from the external tendon duct surface by a distance of 3/16 in as shown in Figure 4.7.
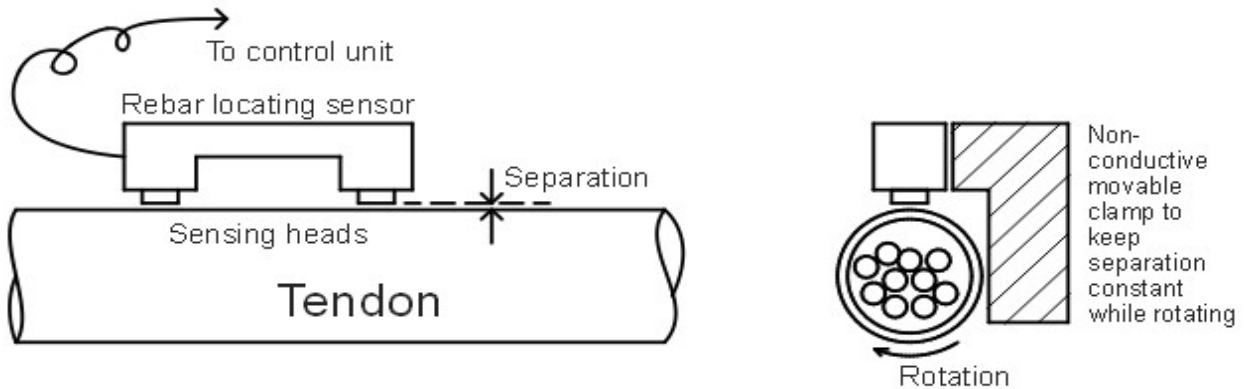
Figure 4.7 Schematic of the Model C-4956 R-Meter® placement.

The heads are ~½ x ½ in square and 5.5 in apart from each other (on center). The sensor center was placed at least 8.5 in away from the tendon segment end to reflect a longitudinally unbiased positioning. The instrument signal reading was recorded as function of the tangential position of the sensor at 10 degree intervals.

Given the large dimensions of the sensor, tests of the concept were not made in the small tendons used for the rotating magnet unit, but were instead made on 4 thicker tendon samples obtained from the FDOT John Ringling Causeway Bridge. The samples have 22 strands grouted within a polymeric duct of ¼ in wall thickness and an outer diameter of 4.5 in. Results are illustrated in Figure 4.8, which shows general semi-quantitative agreement with the cross-section location of the strand envelope.

While not implemented in the final sensor design in this project, further evaluation of this approach merits attention in future research. Issues to explore should include potential for reliable quantitative imaging of strand position and use with thinner tendons, as well as use of multiple sensors to avoid need for rotating moving parts.
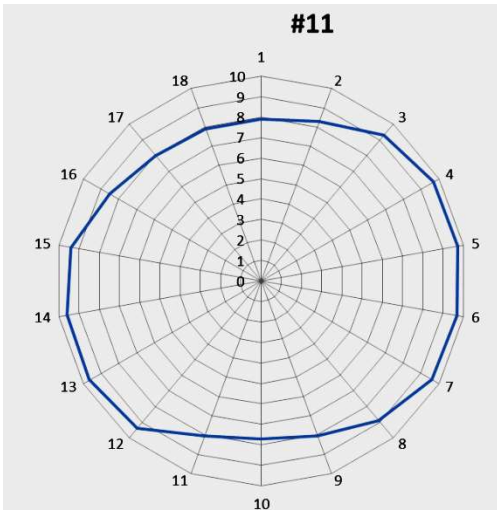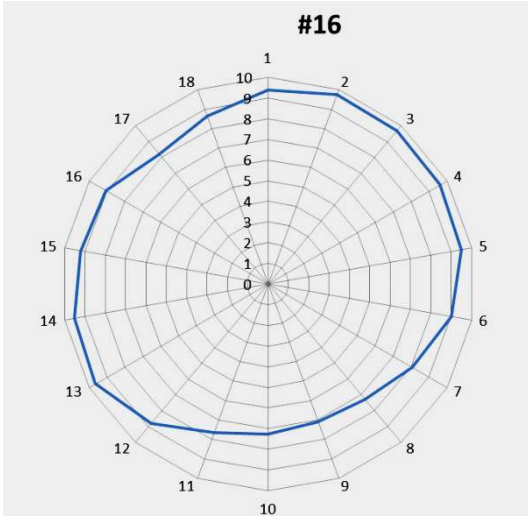
Figure 4.8 Results of semiquantitative strand configuration evaluation using an inductance device applied to two tendon samples from the John Ringling Causeway Bridge.

Data processing and recovery of strand positions in the form of an image.

The prototype sensor provided an output text file that included for each line time, tangential position, and force indication for both magnets. Calibration trials obtained data using a test tendon section for an entire 360 degree rotation (plus a small 6 degree extra rotation to account for any minor axial disparity between magnets). One of the subassemblies was designated as a master unit, and response from the other subassembly was position-translated and multiplied by an adjustment factor to obtain an identical equivalent response for a given position for either subassembly. The adjustment translation and multiplier factors were noted and stored for subsequent use in the data processing program. From then on tendon measurements were limited to back and forth 180 degree rotations of the overall sensor, with the output conditioned per the previously determined adjustment factors.

The transducing system used provides automatic zeroing of all measured values at the start of the test.

The conditioned output data was further processed by deconvolution of the response to account for the native delay of the combined magnet-force transducer system when responding to an external excitation. Assuming linear system behavior, for a given subassembly the resulting measured force response $Fm(t)$ at time t from the start of the measurement is convoluted with the step response $A(t)$ of the subassembly via:

$$Fm(t) = \int_0^t \frac{\partial Fa\,(l)}{\partial l} A\,(t-l)\,dl = \frac{\partial Fa}{\partial t} * A \qquad \text{(Eq.1)}$$

where $Fa(t)$ is the actual value of the force acting at time t, the symbol $*$ is used to express convolution of the two variables per the integration shown, and l is a dummy integration variable An equivalent, more convenient formulation is given by Goldman [43]:

$$Fm(t) = \int_0^t Fa\,(l) \frac{\partial\,(A\,(t-l))}{\partial t}\,dl = Fa * \frac{\partial A}{\partial t} \qquad \text{(Eq.2)}$$

where it is assumed that $A(0) = 0$, consistent with the step response illustrated in Figure 4.6.

Calling $FT(f(x))$ the Fourier transform of the function $f(x)$, the following useful property applies for well-behaved functions:

$$FT(f1 * f2) = FT(f1) \cdot FT\,(f2) \qquad \text{(Eq.3)}$$

where $\cdot$ is the multiplier sign, referring to a term-by-term product of the respective Fourier transforms. Hence, referring to Eq. (2) and since $A(t)$ is determined experimentally from which $dA(t)/dt$ is obtained numerically or by fit to a modeling function, $Fa(t)$ can be recovered from the data by performing:

$$Fa_{recovered}(t) = IFT \frac{FT(Fm(t))}{FT(dA(t)/dt)} \qquad \text{(Eq.4)}$$

where IFT is the inverse Fourier transform operator and the division sign refers to a term-by-term division of the terms of the functions operated upon.

The above functions are conducted as digital operations performed on the data arrays using a MATLAB platform. Appropriate scaling factor modifiers to Eqs. 1- 4 were introduced as needed. The result is an array containing the recovered force Fa vs. time during the

19

measurement. Using the data array relating angular coordinate to time during the measurement, the result is then expressed as a double array including Fa as function of the angular coordinate for the entire tendon duct perimeter around the cross-section examined. The function $A(t)$ was assumed to consist of a simple exponential increase on t/τ, where τ is a seed value equal to the characteristic time obtained as first approximation by fitting of responses such as that in Figure 4.6. The value of τ was further empirically refined by best fit of the recovered back and forth scan data in initial calibration tests.

The next step is to convert the force information into information on the depth of the strand bundle envelope beneath the inner surface of the tendon duct, as function of the angular position within the cross-section and creating an imaging plot of the result. The method chosen for that conversion is to assume for simplicity that there is a power law dependence between Fa recovered for a given angular position, and the local distance at that angular position between the magnet and the strand envelope. That approximation reflects the power law dependence of the force acting between ideal magnetic dipoles aligned on the same axis [44], or between a magnetic dipole and a large nearby susceptible medium [11], as a function of the intervening characteristic distance z. For those systems the force varies proportional to ~ z^{-4}.

To get further insight on the effective magnet-to-strand force dependence, model calculations were made on a COMSOL Multiphysics® platform simulating the system shown in Figure 4.9, for the simplified case of only one strand in the proximity of the magnet. For those calculations the magnet was assumed to have a permanent   volumetric magnetization of 750 (kA/m) and dimensions as shown representative of those used in the prototype. The strand was assumed to have an effective high susceptibility of 4000 (non-dimensional) and a representative diameter as shown, with a length many times greater than the diameter. The calculations were made for cases were z ranged from 1 cm to 4.75 cm, also representative of those anticipated in the prototype operation.
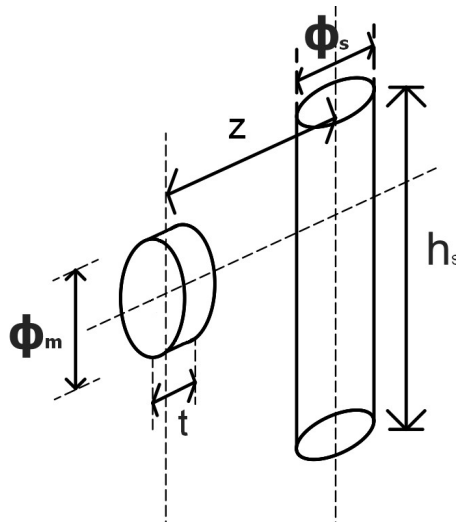
Figure 4.9 Simulation of bar-magnet system

Figure 4.10 summarizes the results, projecting a dependence on z that approximated a $z^{-4.9}$ power law. Figure 4.11 shows the approximate power law dependence that applies when a nominal magnet-steel distance z' is defined as that between the center of the magnet and the point on the steel surface closest to the magnet (z'=z-r where r is the radius of the steel bar). In that case the operating exponent reduces to n'=~3.2 for relatively short bar-magnet distances.
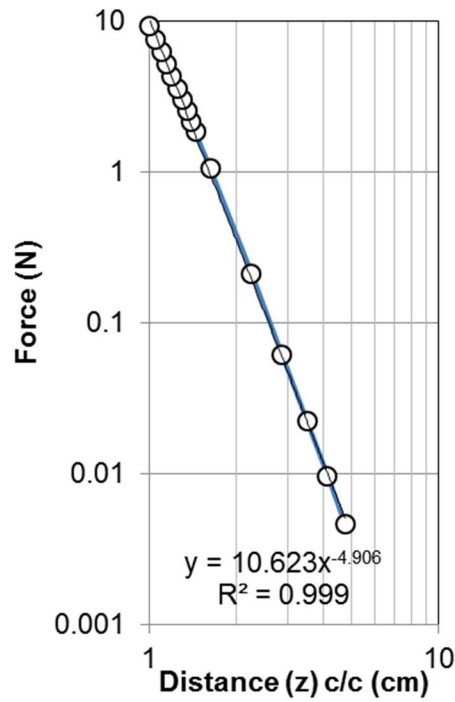
Figure 4.10 Model simulation results of Force (N) vs. z, the center-center distance between the magnet and the steel rod.
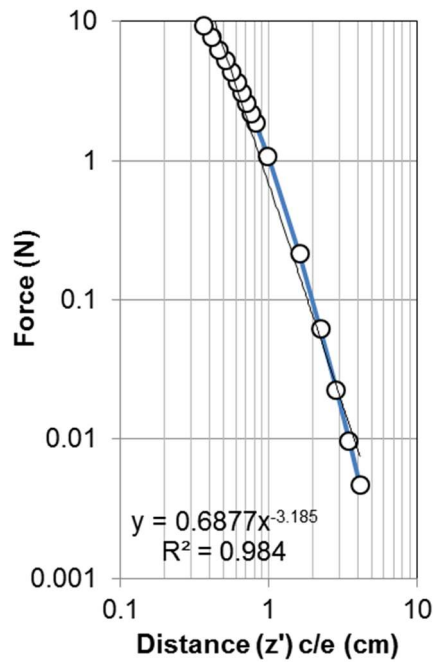
Figure 4.11 Model results of Force (N) vs. z', the center-to-edge distance between the magnet and the steel rod, the trendline is a nominal abstraction roughly indicative of characteristic response in the interval examined.

21

For practical application of the above, an effective value for n' was obtained by best fit to the experimental results. The force vs. angle data from five tendon section samples were obtained, and the results were converted to nominal magnet center-to-strand envelope distance z'_n arrays using trial values of n' starting with a seed value of ~4. Those results were converted into nominal strand envelope radii from the center or the tendon cross-section using the known values of the external tendon diameter, the magnet thickness, the value of h used in the prototype, and a proportionality constant k obtained by calibration using the force F_{me} acting on the magnet for an angular position where a strand was in direct contact with the inner wall of the tendon. Calling w the magnet thickness, for that situation, the constant k has the value

$$k = F_{me}\, z'^{n'} = Fme\, (w/2 + h + Pt)^{n'} \qquad (Eq.5)$$

where Pt is the polymeric duct wall thickness (known from design).

Independent direct measurements of photographs of the tendon segment cross-sections evaluated yielded the actual values of z'_t for each of the individual strands on the strand bundle envelope of each tendon segment. The sum of the squared differences $(z'_{ni}-z'_{ti})^2$ (with i ranging from 1 to the number of strands delineating the strand bundle envelope) for each tendon sample was then minimized by choice of the optimal value of n' using the Excel® Solver procedure. The procedure yielded values of n' ranging from 3.1 to 3.7, with an average value of 3.25 and a standard deviation of 0.4. The value 3.185 was then adopted as a uniform master value to be used for processing the data of all the tendons.

The result of processing the data is shown in Figure 4.12, which demonstrates examples of good quantitative agreement by superposition of the recovered and actual strand bundle position for the tendon segments examined. The standard deviation of $z'_{ni}-z'_{ti\ was}$ in the order of <1 mm, corresponding to a typical percentage coefficient of variation in the order of only ~5%.

Additional correction for the effect of small, but sometimes significant, magnetic susceptibility of the grout has been estimated in work related to the development of the field unit in FDOT contract BDV25-977-52, Field Demonstration of Tendon Imaging Methods [39].

Chapter Summary

The objective of this part of the project was achieved with the development and implementation on a working prototype of a method to recover and image strand positions by means of rapid external measurements with a technique that is simple and suitable for practical production. The recovery is reproducible and accurate to the extent that the result is useful for using the position data to interpret the results of the impedance method selected in chapter 3 to assess grout condition. Chapter 6, where both methods are integrated, presents further improvement of the strand position imaging prototype, including the use of a gyroscope-based angular position detector that eliminates the need for the position measuring wheel.
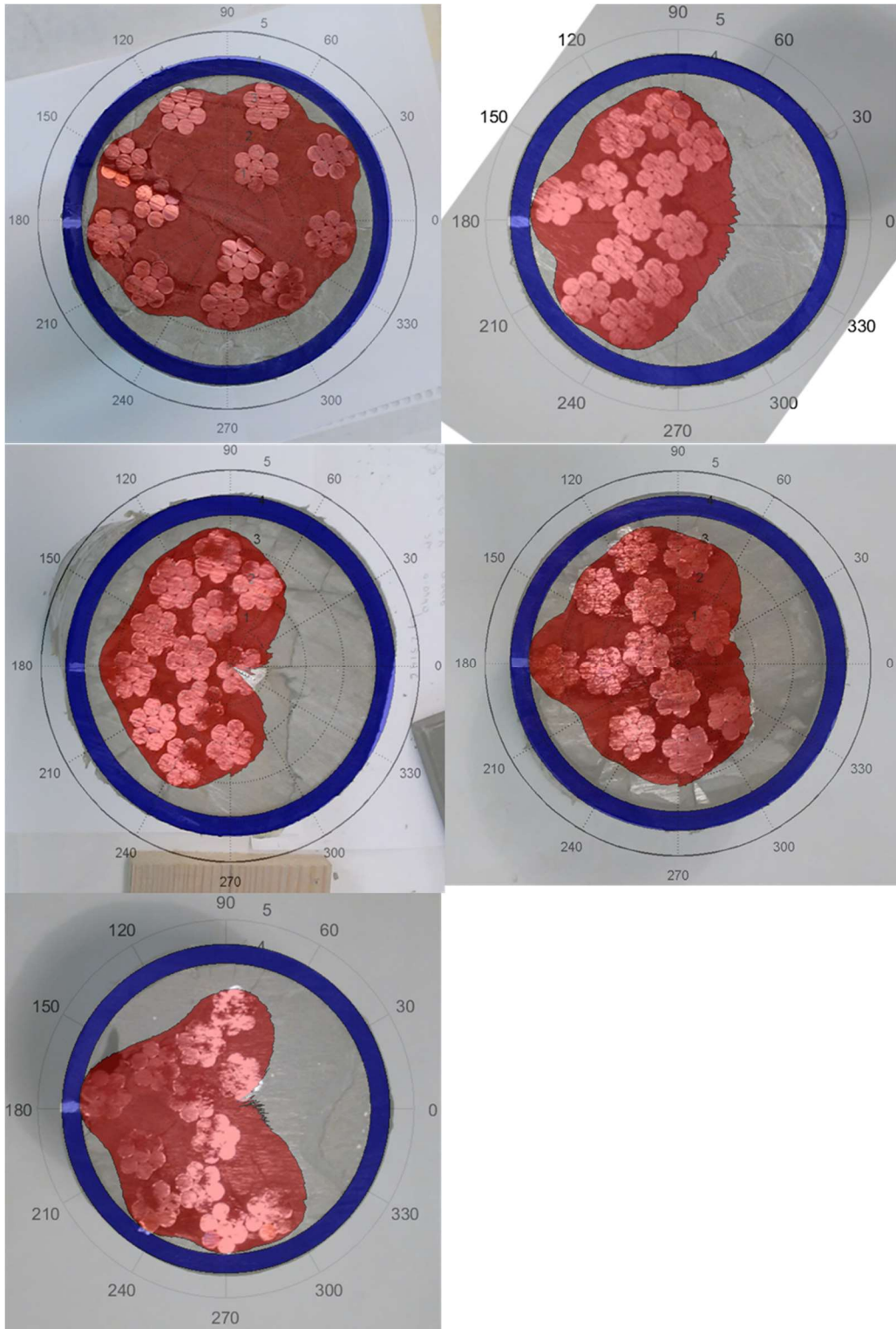
Figure 4.12 Examples of strand envelope recovery on cross-section of various tendon segments examined. Duct outer diameter is ~3.5 in; duct wall section represented by the blue ring. The recovered envelope (red) has been superimposed on an actual picture of the tendon segment cross-section at the end of the segment.

5. GROUT ANOMALY DETECTION USING IMPEDANCE SENSOR

Approach and challenges

The applicability of an impedance electromagnetic coupling method was examined in the manner shown in Figure 5.1, left, for application to typical external tendons encased in a polymer duct.
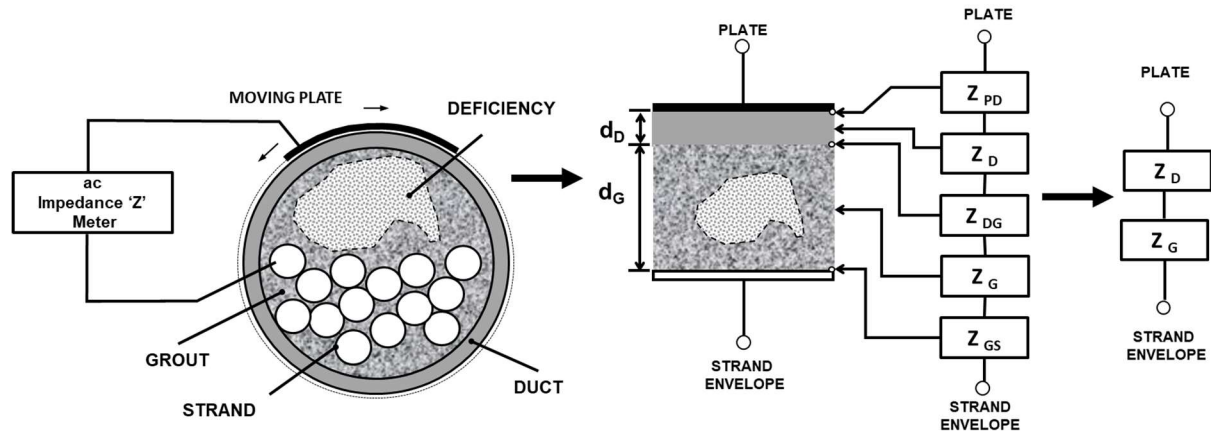
Figure 5.1 Left: Electromagnetic coupling test method arrangement. The moving metal plate is shaped to fit the external duct surface. Center: Simplified composite dielectric/conductive configuration. Right: Further simplification

In this scheme, measurements are made of the *ac* impedance Z between an external conductor plate (of limited angular spread and extending longitudinally for ~ 1 duct radius) in contact with the outer surface of the duct, and a conductor connected to the strand bundle. The strand bundle is electrically interconnected at the anchor points so it can be assumed to be electrically continuous and behaving approximately as a conductor bounded by the strand bundle envelope. Rotating the plate around the duct perimeter and measuring Z as function of rotation angle yields an angular impedance profile. At every angle the Z value depends on the combined impedances of the polymer duct, the grout space between the inner surface of the polymer duct and the strand bundle envelope, and finally the respective metal-medium interfaces. The grout space can include sound grout and deficiencies if present, so it behaves as a composite material, which may be treated on first approximation as a homogeneous medium with average properties equivalent to those of the composite.

On further simplification, the high frequency electrical behavior of the system for a given angular position of the plate may be abstracted (Figure 5.1, center) as being that of a simple parallel-plate capacitor with a layered dielectric/conductive fill space. The curvature and unevenness of the plate, tendon cross-section and strand bundle surface are ignored, as are any current spread deviations from a simple one-directional current flow scheme. The total impedance of the series combination of layers is the sum of each of the components. Those components are the plate-duct interfacial impedance Z_{PD}, the duct layer impedance Z_D, the duct-grout space interfacial impedance Z_{DG}, the grout space composite layer impedance Z_G, and finally the grout space-strand envelope interfacial impedance Z_{GS}. By operating at a high enough frequency (e.g., MHz range or above) the impedances of the interfaces may be considered to be negligible [45], so only the duct and grout space impedance components (Z_D

and Z_G) merit consideration, leading to the further simplified abstraction in Figure 5.1, right. The measured impedance in this case is then for that series combination

$$Z = Z_D + Z_G \qquad\qquad\qquad \text{Eq.(6)}$$

As the duct material is normally quite uniform in composition and thickness, the impedance component Z_D may be regarded as being approximately the same at all angles, and hence it can be subtracted from the measured value of Z leaving for consideration just the grout space component Z_G. Z_G depends on the local grout space thickness d_G and the grout composite condition. The thickness dependence could be discounted by knowledge of the strand envelope position at each angle. After discounting for thickness effects, the remaining (condition) portion of Z_G serves as an indicator of any deviation from normal grout behavior at that angular location. As it will be shown later, that component can be highly sensitive to some deficiencies such as voids or zones of unhydrated grout. Those deficiencies would result in a markedly greater value of Z_G compared to that for sound grout. Other deficiencies such as a high water content in "chalky" grout [1-3] would be manifested instead by a lower value of Z_G. In either case, the presence of a deficiency, and to some extent its nature could be flagged by appropriate coloring or pattern in a graphic representation of the cross-section The strand position information together with that indicative of grout condition can then be combined into a 2D image descriptive of the strand-grout configuration and deficiencies if any at that location. Repeating the process at various longitudinal tendon positions yields a 3D survey of the inner arrangement and condition of the strand and grout composite.

The ability of this concept to reveal grout deficiencies is in part a function of the anticipated nature and relative values of Z_D and Z_G, discussed next.

The HDPE duct material is a well-known dielectric insulator so in the parallel plate approximation the portion beneath the plate footprint behaves closely as a simple equivalent circuit capacitor of value

$$C_D = \frac{\varepsilon * \varepsilon_o * A}{d} \qquad\qquad\qquad \text{Eq. (7)}$$

where

C_D is the capacitor value in farads (F).
ε is the dielectric constant of the medium (ε_D approximately 2.2 for HDPE [46]).
ε_o is the permittivity of space 8.854×10^{-12} F/m.
A is the footprint area of the capacitive plate in m^2.
d is the depth of the medium (in this case d_D per Figure 5.1 center) in m.

Hence Z_D approximates purely capacitive behavior of the form

$$Z_D = \frac{1}{j * \omega * C} \qquad\qquad\qquad \text{Eq. (8)}$$

where

$j = \sqrt{-1}$
$\omega = 2 * \pi * f$
f is the frequency of the alternating current used for the measurements.
Z_D is the impedance in ohms (Ω).

Normal sound grout has a hydrated cementitious matrix with a pore network partially filled with a conductive pore solution. In the meso scale (mm-cm) the electrical behavior of grout at a given *ac* test frequency f can be approximated as that of a homogeneous medium with an effective electric conductivity σ and dielectric constant ε_G [47,48], with impedance related to those properties. That behavior can be represented at that frequency by an equivalent parallel combination of a capacitor and a conductor, both with dimensions corresponding to the grout space and material dielectric constant and conductivity representative of the grout condition. The capacitance C_G (the circuit value corresponding to the capacitor) is calculated per Eq. (7) with d=d_G and ε = ε_G and A the same footprint area of the capacitive plate. For conventional treatment, the conductor is represented as an equivalent resistor, with a resistance value R (ohms) given by

$$R_G = \frac{dG}{A*\sigma_G} \qquad\qquad\qquad \text{Eq. (4)}$$

where

σ_G is the electric conductivity of the grout in $(\Omega m)^{-1}$.

The impedance of the grout space Z_G in ohms (Ω) is therefore.

$$Z_G = R_G + \frac{1}{j*\omega*C_G}$$

As it is shown in Appendix A, at the test frequency chosen for the application (1 MHz as a practical compromise) typical values of σ_G and ε_G are, for sound grout, in the order of $3*10^{-3}$ $(\Omega m)^{-1}$ and 50 respectively. For the system examined here typical dimensions are in the order of A=$2.5*10^{-3}$ m^2, d_D=$6*10^{-3}$ m and d_G= $2*10^{-2}$ m. Thus at the operating frequency of 1 MHz the equivalent circuit parameters have values in the order of C_D~8 pF, C_G~40pF and R_G~4 kΩ, corresponding to |Z_D| ~ 19 kΩ and |Z_G|~3 kΩ, for sound grout. While Z_G and Z_D are differentiated in phase angle by about $\pi/4$, clearly Z_D is the dominant component of the series combination in the case of sound grout filling the grout space.

If the grout space includes same void presence, it may be viewed as a composite material with effective average dielectric constant and conductivity. Those parameters are related to those of sound grout by a combination rule dictated by the geometric arrangement of the voids. For uniformly distributed, relatively small voids the combination may simply approach a linear combination of the conductivity and dielectric constant of normal grout and void space. For a given pore network configuration and degree of hydration, both average dielectric constant and conductivity tend to increase in value with increasing water content, because of the greater degree of pore interconnection as well as the high dielectric constant of water. Conversely, as the fraction of voids approaches unity, σ tends to zero and ε to 1.

For such "full void" limit situation, Z_G would become nearly purely capacitive, and given the dimensions considered above, |Z_G| would become several times greater than |Z_D| and hence a dominant component of the measured impedance. Under full void conditions the simple series combination imagined in Figure 5.1 (right) is no longer a close approximation of the system behavior, because a sizable part of the current is diverted to paths on each side of the capacitive plate. Precise evaluation of the full void condition and intermediate cases is examined experimentally and by computer modeling later in this chapter. Nevertheless, this

preliminary evaluation shows good prognosis for the detection of full voids, via a sizable increase in impedance as the plate travels over the region.

Other intermediate conditions would be expected to translate into recognizable impedance response signatures as well. Poorly hydrated grout (very low to no water present) would result likewise in conditions closer to those of an air-filled void. Conversely, if there is excess water regions (as in so-called soft or chalky grout [1-3]) those parameters are expected to increase relative to the normal grout. That increase would lower the value of the impedance of the grout space to less than the already low value of normal grout relative to that of the polymer duct. Hence, cases of high water content are expected to present a greater challenge for detection than cases of low water or full voids. The extent to which that challenge was met, and possible ways of improving detection ability by future development, are discussed later in this chapter.

Two concurrent approaches were used to evaluate the ability to detect grout deficiencies with impedance measurements in the light of the above discussion. The first consisted of experimental demonstration measurements with a traveling plate placed on small tendon sections with and without grout voids and other deficiencies to serve for modeling validation and calibration, and to obtain values of the relevant performance parameters. The second consisted of computerized physical modeling of the expected impedance behavior with and without a simulated grout deficiency, to aid in identifying key performance factors. The methodology and outcome of those approaches is presented next.

Experimental Investigation

Methodology

Two series of experiments are presented in this report. A First series used conventional impedance measuring equipment and a point-by-point setup dedicated to impedance tests only. A Second series was conducted with the tendon imaging unit prototype described in Chapter 6 and used for the validation tests detailed in Chapter 7.

Physical Configuration

For the First series of experiments two replicate custom tendons (named Tendon #1 and #2) were cast with a void in the center for experimental testing of impedance on the variations of grout conditions in a given tendon.

The cast tendons were ~30 inches long with ~3.5 inch nominal outer diameter. The high-density polyethylene was ~0.22 inches (5.6 mm) thick. The tendon segments included 12 ½ inch steel strands (7 wire) lumped towards away from the center

EUCO Cable Grout PTX was used to cast the tendons. Table 5.1 lists the grout mixture proportions. Mixing was conducted per manufacture's specifications [49], including a water-to-grout powder ratio within specified limits.

Table 5.1 – Grout mix proportions

EUCO Cable Grout PTX	21.67 lb
Water	5.053 lb
Water/grout ratio	0.233

The specimens had a central 4-inch-long semi-circular void at the center, with a void volume ~215 cm^3. The imperfect semi-circular void has a width of ~2.9 inch. To create the central void a piece of Styrofoam was put at the location specified. The Styrofoam was held on center of the tendons by a ¼ inch screw that kept it centered when the grout was poured. After the grout cured, the Styrofoam was then melted with a finite amount of acetone.

The void starts at an angular position of ~90^0 to ~270^0 (~180^0). Angle designations are as seen in Figure 5.2-b.

The preparation of custom simulated tendon test pieces allow for controlled removal and repositioning of intentionally introduced defects (air, un-hydrated grout, water), without substantially affecting the condition of the rest of the tendon segment.
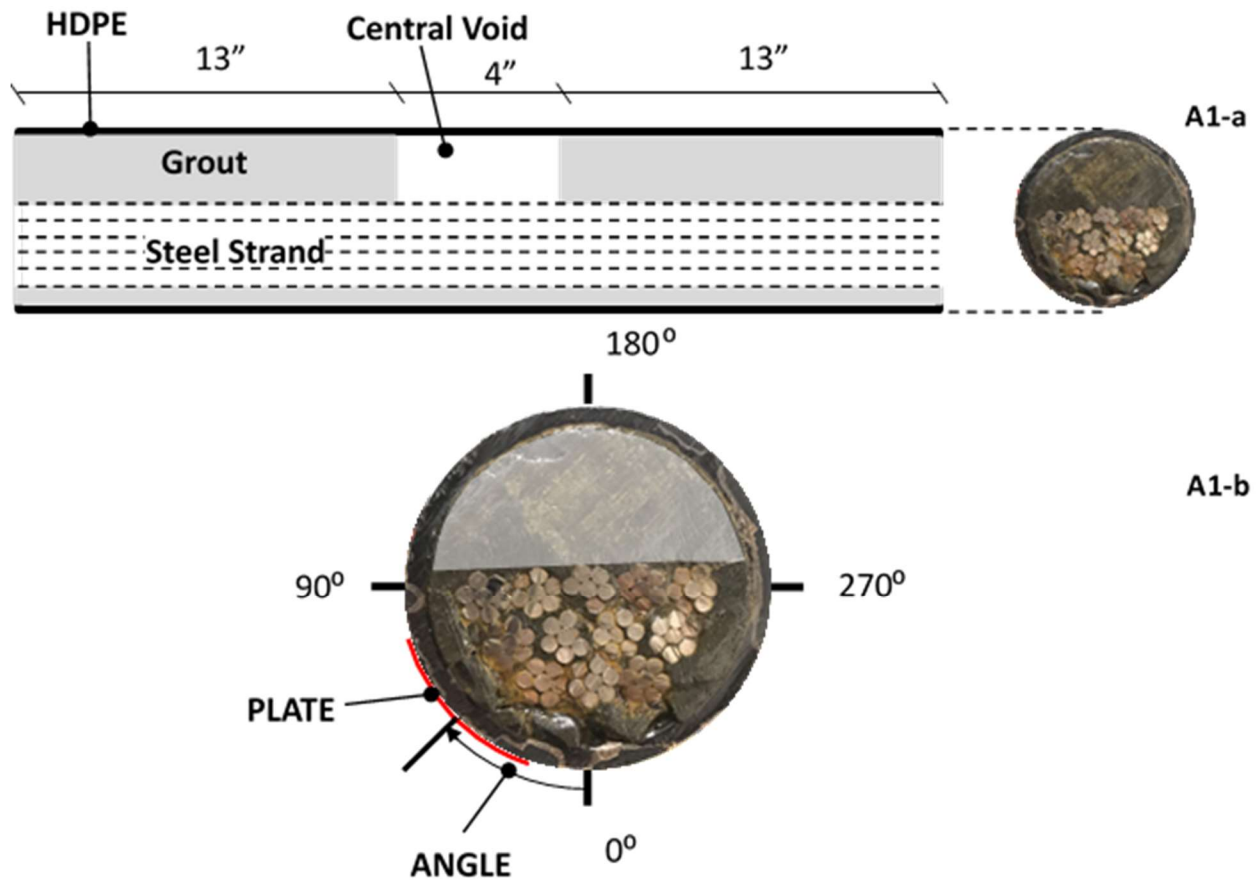
Figure 5.2 - Plan view of a custom cast tendon's geometrical features (A1-a); cross-section of the cast tendon (A1-b). Strands are lumped. Central void is highlighted.

For the Second series of experiments a group of four specimens (named Ducts A, B, C and D) covering a variety of grout conditions and deficiencies was used. Those specimens were prepared for the validation tests against Gamma Ray Tomography GRT results, addressed in Chapter 7. Reference is made to the specimen configuration and tendon imaging description given there. Results relevant to establish the effect of grout deficiencies on the impedance response are presented here.

Experimental Setup and Test Conditions

For the <u>First series</u> of measurements a Hewlett-Packard 4192A LF impedance analyzer was used to measure the modulus of impedance of the system prototyped as described schematically in Figure 5.3 and pictured in Figure 5.4. The results are presented as function of angular position of the duct in impedance (ohms) with a frequency of 1 MHz. The frequency was chosen due to ease of implementation when the imaging prototype was being developed, and a higher frequency (e.g., GHz range) can be implemented with advantage (see later on this chapter) but requires a more sophisticated hardware implementation strategy. While both real and imaginary components of the impedance were measured in the preliminary experiments, the modulus of impedance was the value used as the main descriptor. This choice reflects the ease of implementation in the prototype described later, as it was found to provide sufficient information for assessing key aspects of grout condition.
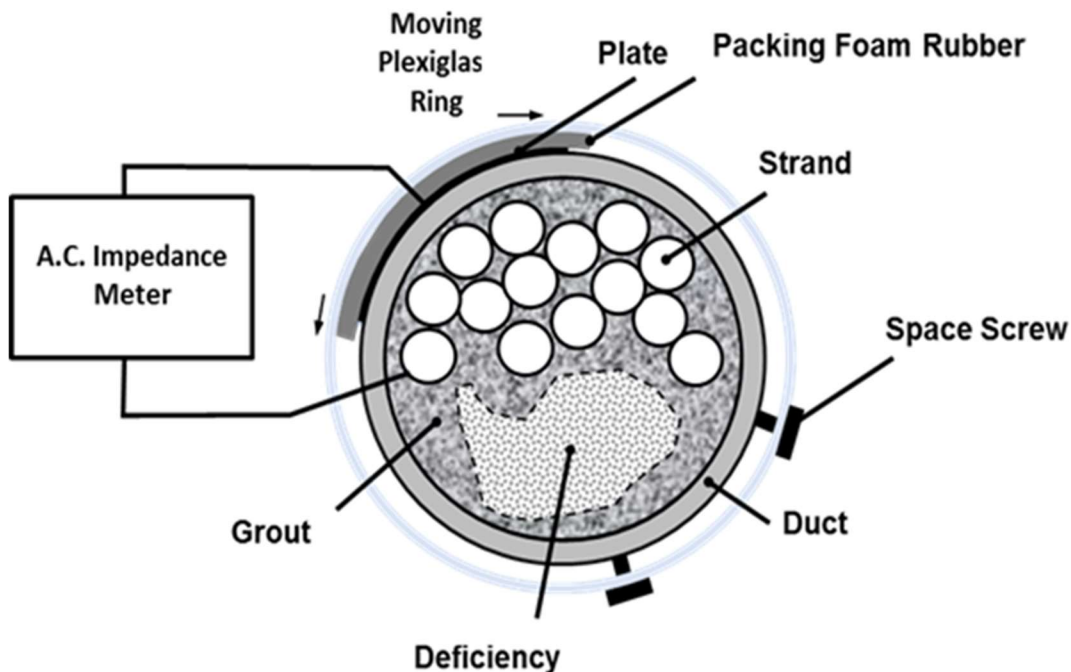
Figure 5.3 Electromagnetic coupling test method arrangement. Use of a plastic frame, pressure foam pad, and spacers for stable movement of the sensing plate on the outer duct perimeter.
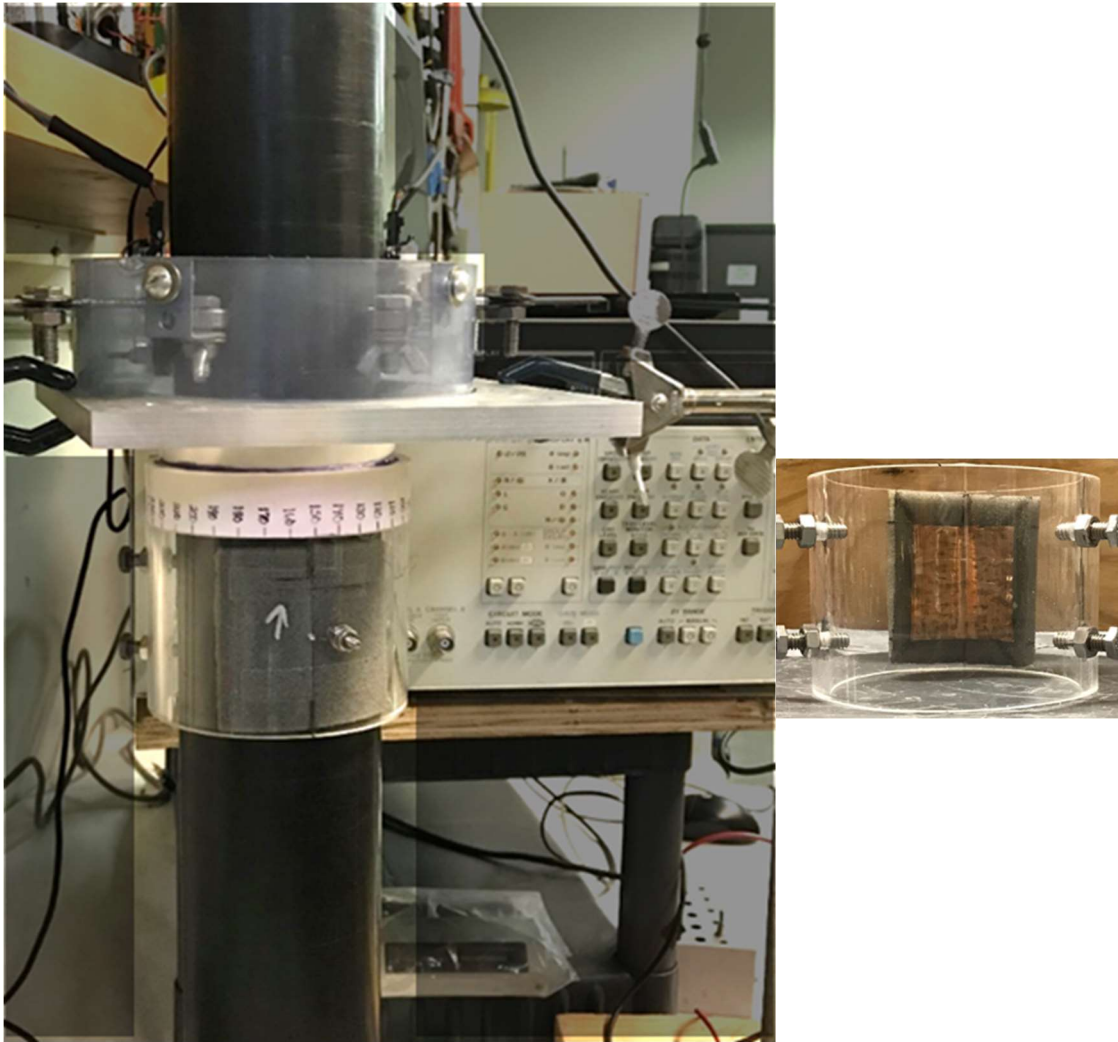
Figure 5.4 Left: Experimental prototype arrangement for steel strand location detector prototype and impedance module for tendon measurements. Right: inner part of the impedance module with a 5 cm x 5 cm copper plate.

Measurements were performed in a two-conductor mode using the Model HP 16047A two-conductor test fixture and short (~12 cm long), ~0.15 mm diameter wires each connecting to the capacitor plate and strand assembly respectively. The capacitor plate was a square of 0.12 mm thick copper plate, 5 cm x 5 cm, curved to fit the outer diameter of the tendon segment to be tested. Foam rubber backing was used to press the plate against the surface of the tendon duct. The Plexiglas ring with the plate rotated periodically so the center of the plate was precisely placed consecutively over various marked angular positions around the tendon perimeter. Impedance was recorded while the system was at rest at each position before rotating to the next. Readings showed little sensitivity to modest changes in distance of the tendon to the front of the apparatus or the laboratory table, which was not metallic.

Each specimen to be evaluated was prepared by first ensuring that all strands were interconnected as they would be in an actual field situation. The steel strands at one end of the tendon segment were connected using a galvanized piece of steel and structural wire to ensure the connectivity of the strands. Then a threaded rod was connected to the galvanized metal piece extending to the outside of the tendon segment to provide a robust connection between the steel strand assembly and an aluminum plate. The connector (Figure 5.5c-d) was threaded against the center of the aluminum plate. A thin wire was attached to the connector with an alligator clip, giving a sliding contact to the wire that led to one of the terminals of the impedance analyzer. The sliding contact allowed for rotation of the Plexiglas around the tendon segment without entanglement of the wire. The wire leading to the other impedance analyzer terminal was connected to the capacitor plate. The capacitor plate was held steady with a fixed upward orientation on top of the tendon segment as it was rotated. After the grout cured, both ends of each tendon were coated with clear polyurethane to minimize moisture evaporation.

Impedance measurements were conducted at 10° intervals around the tendon segment perimeter, at a frequency of 1 MHz and excitation amplitude of 1 V rms. Ages in days after specimen casting are noted for each data set.
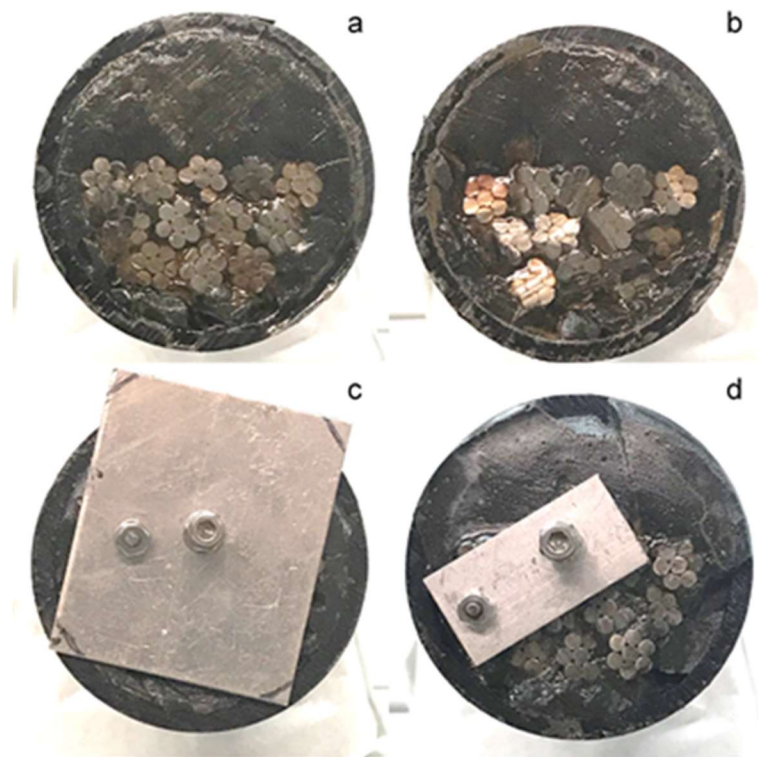
Figure 5.5 (a-b) Cross-section profile of the custom-built Tendons #1 and #2. (c-d) Cross-section of the back end of tendons #1 and #2.

Test conditions for the First series of experiments included the following:

- Tendon cross-section with normal, sound grout fill ("Sound"). This condition was examined by operating the rotating impedance sensor in a region of the tendons halfway between the edge of the central void and the end of the tendon (~ 1.5 tendon duct diameters clear from either).

- Cross-section with an air-filled void with dimensions indicated in Figure 5.2a, achieved by operating centered on the void region ("Void").

- The void and placement indicated above but filled with unhydrated grout, simulating a spot resulting from an unmixed grout plug sent into the tendon ("Unhydrated Grout").

- The void filled with pure copper shot (graded sizes from ~ 1 mm to 5 mm in diameter, ~800 g) simulating the partial presence of a conductive medium in the tendon cross-section, as in the case of bleed water. A dry conductive fill was chosen to allow for a reversible change of conditions in continuation tests ("Conductive Fill").

Measurements were taken at various ages after casting the cylinders, indicated in the captions of the corresponding figures displaying the results.

Test conditions for the Second series of experiments included regions of sound grout, voids, voids filled with unhydrated grout, voids filled with water, and regions of high water-to-grout "soft" grout (see Chapter 7). There was some variation of strand arrangement and void geometry from one specimen to the other, but the nature of the conditions (with the exception of "soft" grout) was repeated in one or multiple instances. All tests reported for the Second series were conducted at an age of 105 days after casting. All tests conducted at 1 MHz.

Table 5.2 – Test conditions for the Second series of tests with Ducts A to D

Grout / Void Condition	Sound	Void	Unhydrated	Water	Soft
A	●	●	●	●	
B	●	●			●
C	●	●	●	●	
D	●	●	●	●	

Results

First series: Tendons #1 and #2.

Figures 5.6, 5.7 and 5.8 illustrate respectively the real, imaginary and modulus of impedance vs. angular position of the sensing plate on the specimen, with the sensor placed on each of the four conditions indicated above. Those figures show the data for Tendon #2, for which a full set of data was available first. Appendix B shows that the trends were reproducible when determined with replicate Tendon #1 at a later specimen age. Additional results given in Appendix B showed further trend reproducibility and repeatable behavior for two conditions (sound and void) in consecutive measurements at comparable ages.
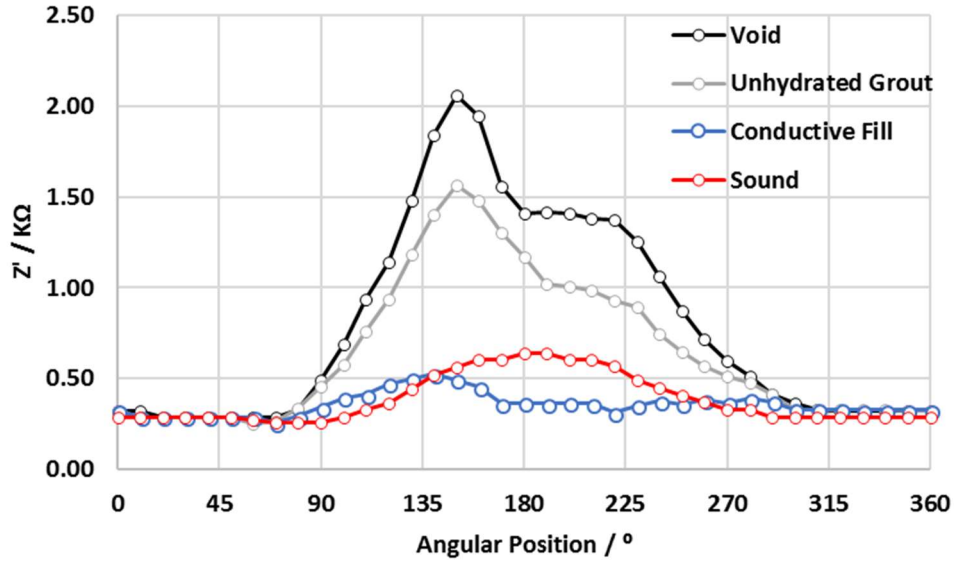
Figure 5.6 Real part of the complex impedance vs. angular position for Tendon #2 (age 166 days for void and sound, 163 days for unhydrated grout, and 169 days for conductive fill) at center with section filled with air, unhydrated grout, and conductive fill. Impedance results for a sound cross-section also included. All experimental results in this and subsequent figures are for a frequency of 1 MHz.
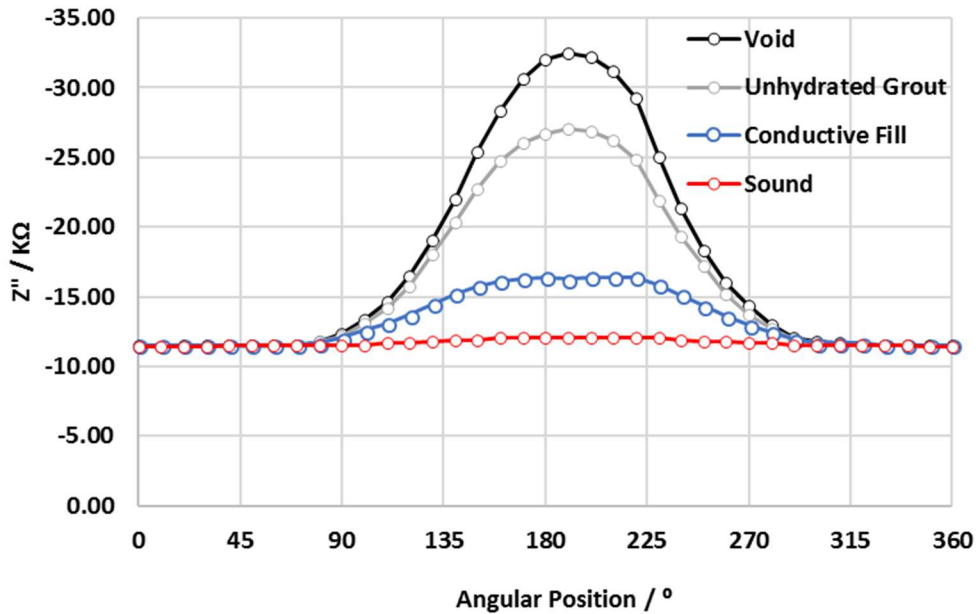
Figure 5.7 Imaginary part of the complex impedance vs. angular position for tendon segment #2 (same ages as in Figure 5.6) at center with section filled with air, unhydrated grout, and conductive fill. Impedance results for a sound cross-section also included.
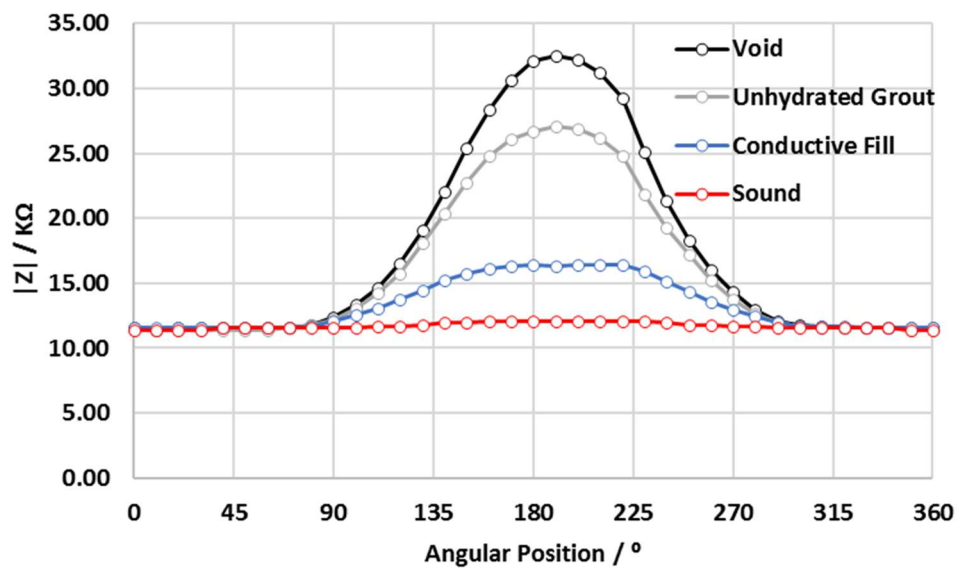
Figure 5.8 Modulus of impedance vs. angular position for tendon segment #2 (same ages as in Figure 5.6) at center with section filled with air, unhydrated grout, and conductive fill. Impedance results for a sound cross-section also included.
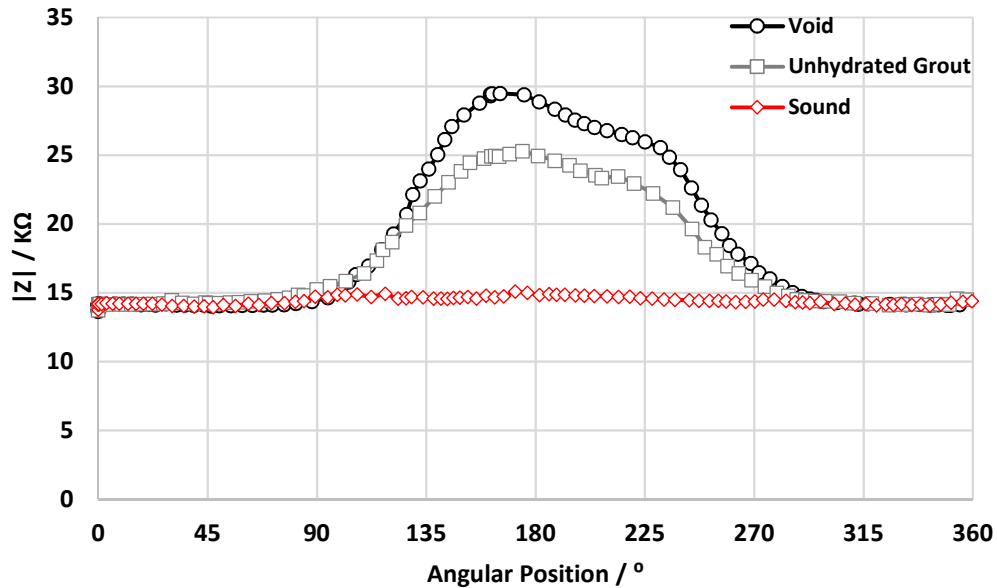
Figure 5.9 Modulus of impedance vs angular position for tendon A, at the same void (Position P1) that had air (age 36 days) and then was filled with unhydrated grout (age 55 days). Impedance results for a sound cross-section (P2) (age 55 days) also included. All experimental results in this and subsequent figures are for a frequency of 1 MHz.
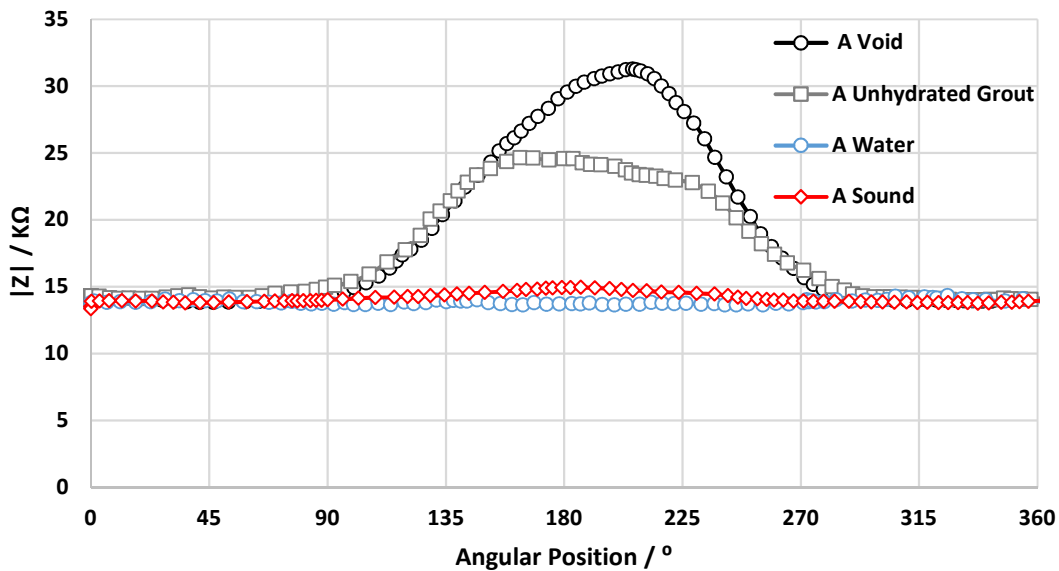
Figure 5.10 Modulus of impedance vs angular position for tendon A (age 105 days) for void (Position P3), unhydrated grout (P1), water (P5), and sound cross-section (P2).

35
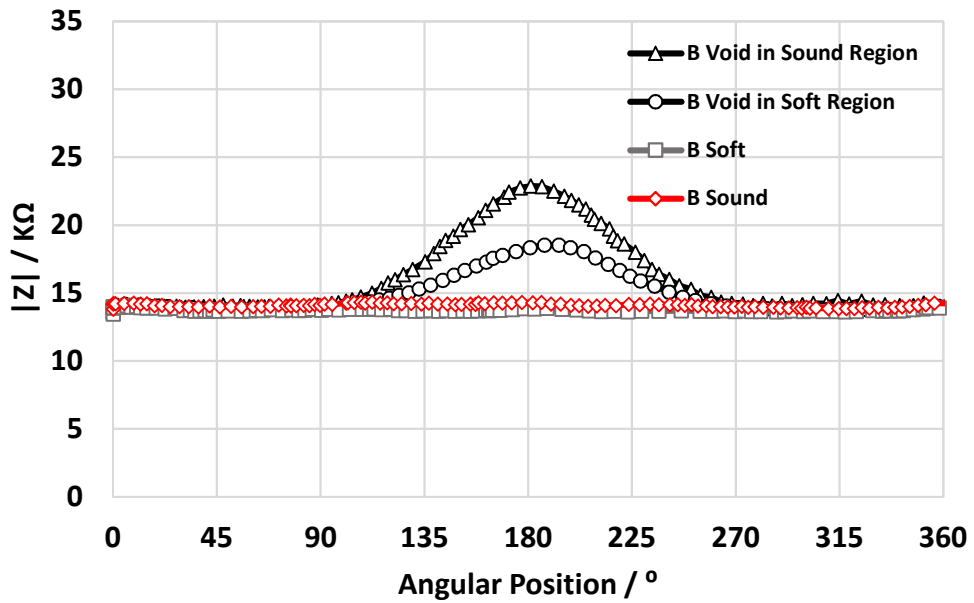
Figure 5.11 Modulus of impedance vs angular position for tendon B (age 105 days) for the different cross-sections; void in soft (P1) and void in sound grout (P4), soft (P2), and sound grout (P3).
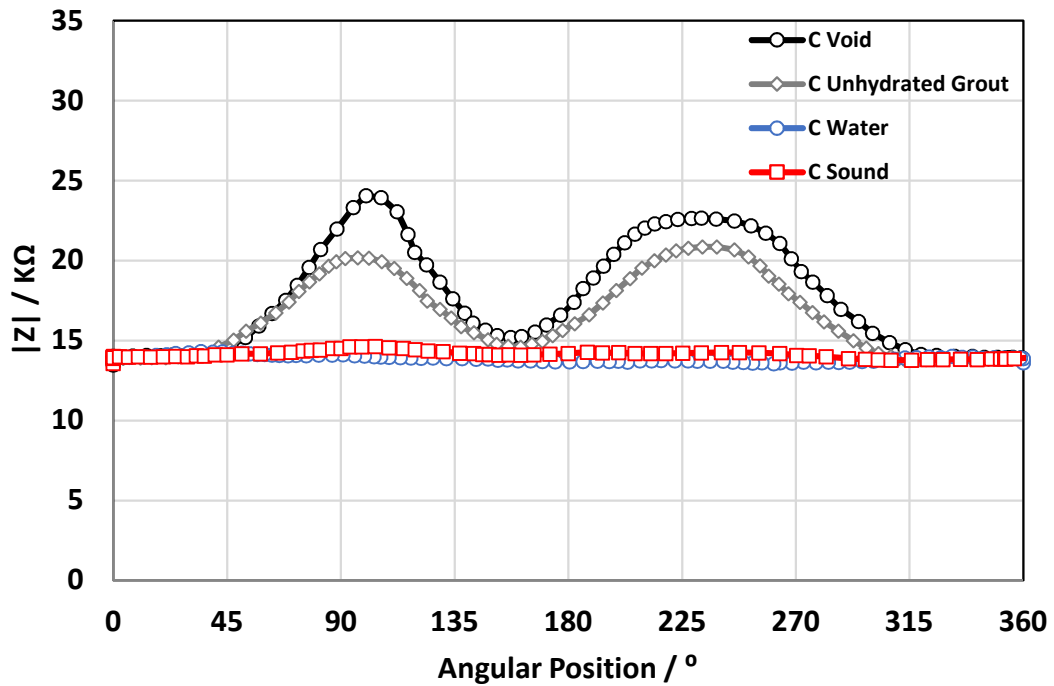
Figure 5.12 Modulus of impedance vs angular position for tendon C (age 105 days) for the different cross-section; void (P3), unhydrated grout (P1), water (P5), and sound grout (P2).
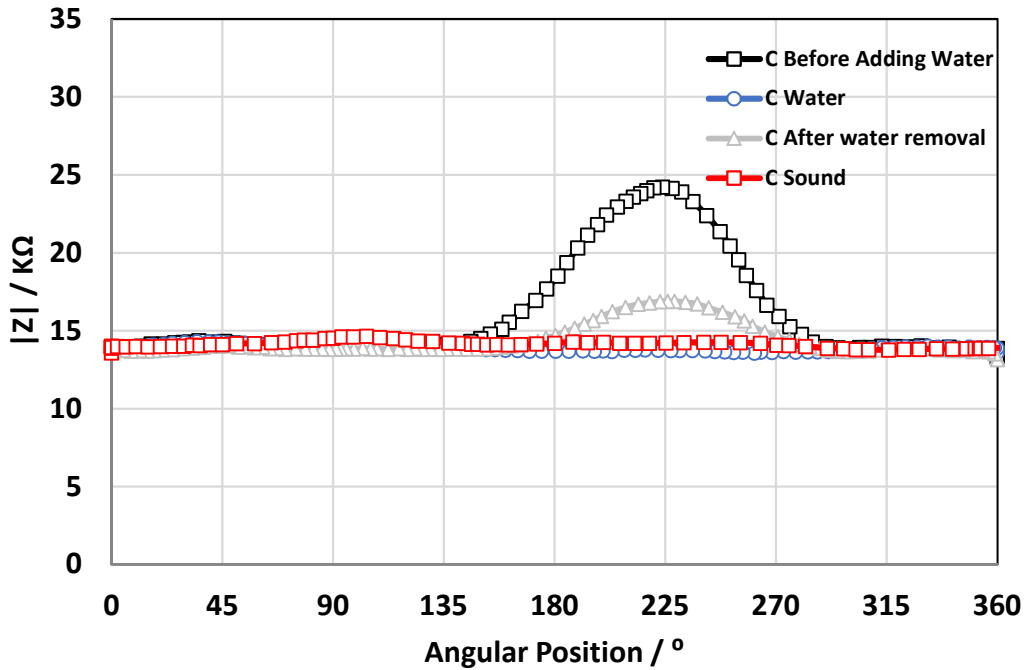
Figure 5.13 Modulus of impedance vs angular position for tendon C (age 105 days) for the same void (P5) before adding water, when water was added, and ~30 min after the water was removed. Impedance results for a sound cross-section also
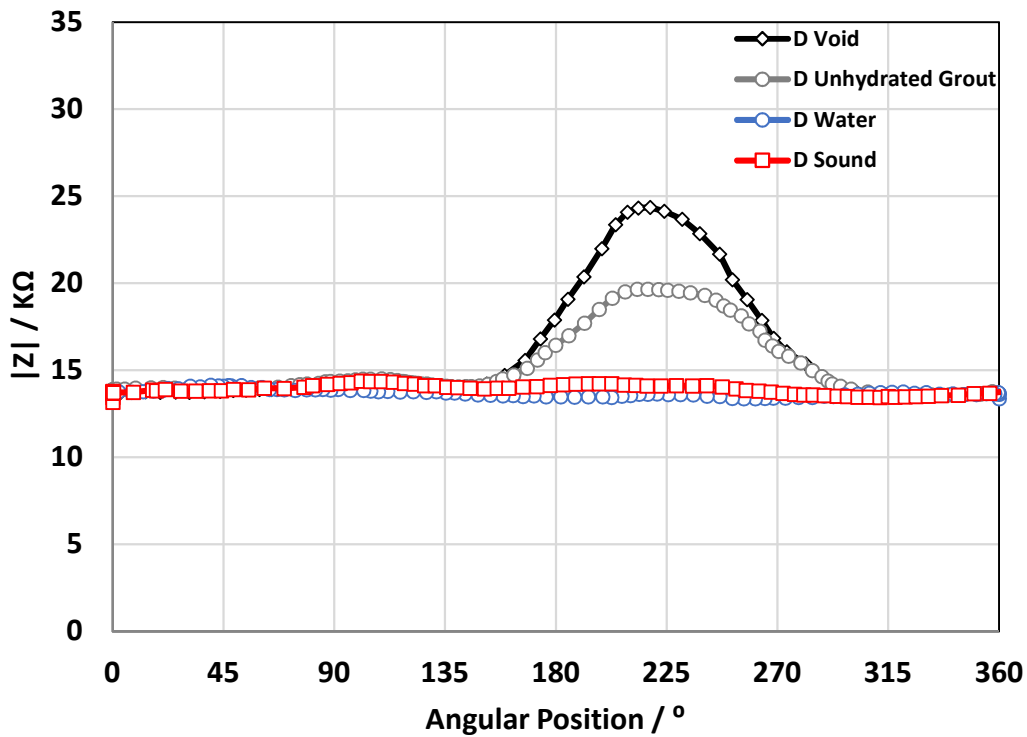
Figure 5.14 Modulus of impedance vs angular position for tendon D (age 105 days) for the different cross-section; void (P3), unhydrated grout (P1), water (P5), and sound grout (P2).
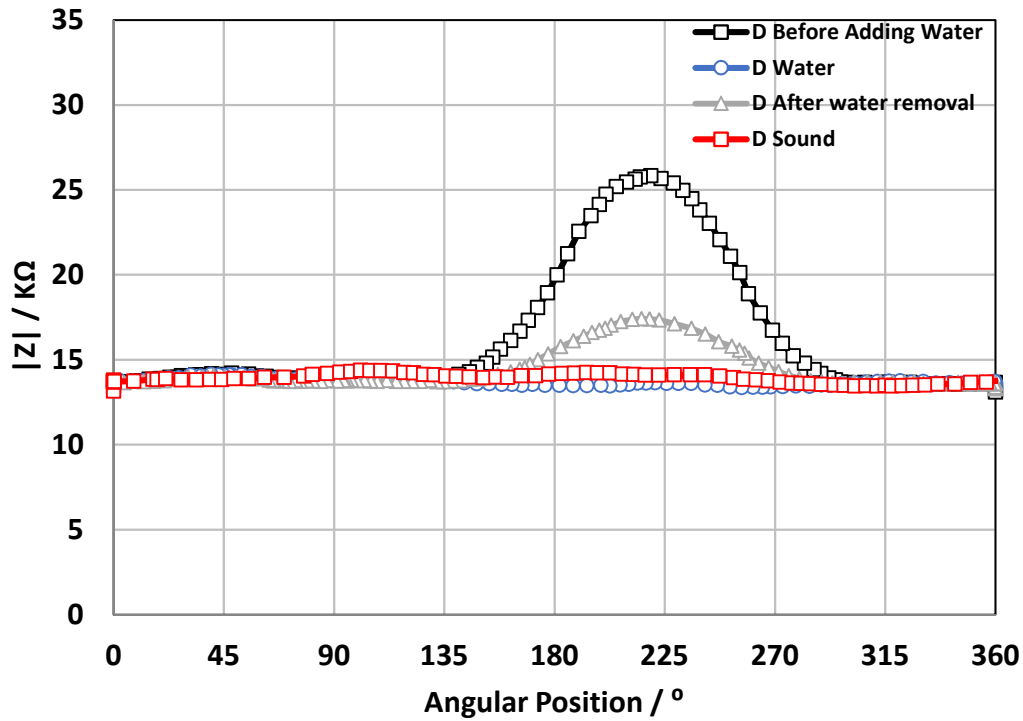
Figure 5.15 Modulus of impedance vs angular position for tendon D (age 105 days) for the same void (P5) before adding water, when water was added, and ~10 min after the water was removed. Impedance results for a sound cross-section (P2) also included.
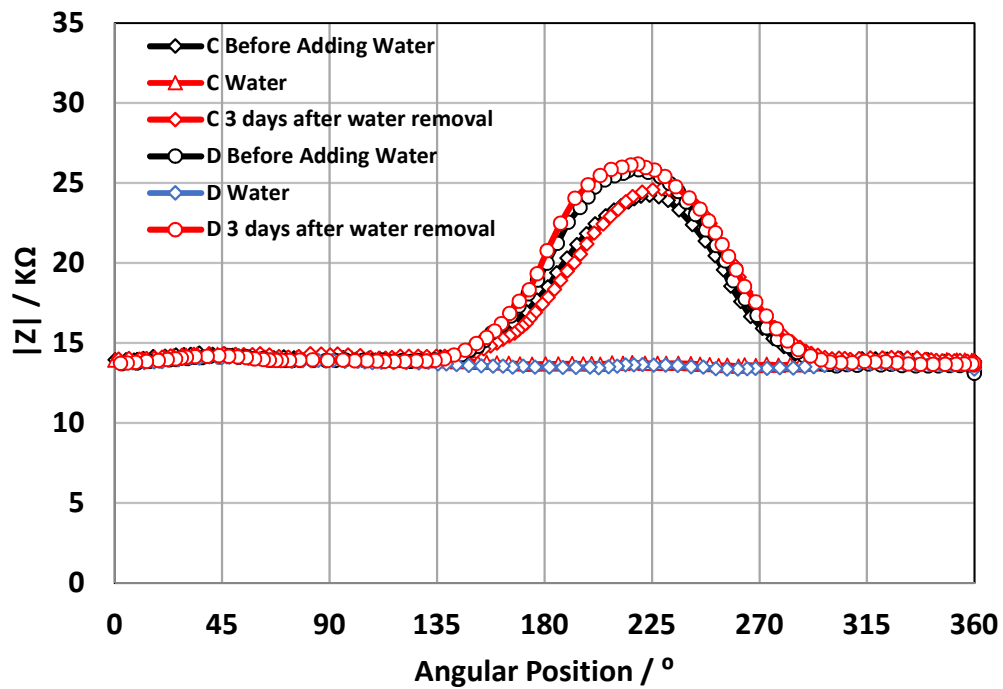
Figure 5.16 Modulus of impedance vs angular position for tendons C and D (age 105 days) for the same void (P5) before adding water, when water was added, and 3 days after the water was removed.

Discussion

The <u>First series</u> results showed promising evidence of feasibility of the impedance measurements to reveal grout variations in a stable and reproducible manner, with low data scatter. The modulus of impedance when the sensor was over sound grout (Figure 5.8) showed, as expected from the earlier arguments, a value that increased only relatively slightly when the sensor moved over the positions where the grout thickness was greatest, consistent with the impedance of the polymer duct being dominant. The impedance modulus value in those conditions, about 12kΩ, was also in the order of that estimated earlier for a comparable geometry and plate dimensions, with any differences easily explained by latitude in the value of effective dielectric constant, duct wall thickness, and deviations from an ideal parallel plate system.

As shown in Figure 5.6, more sensitivity to variations in sound grout thickness can be obtained in the real part of the impedance, which is dictated in large part by the ohmic component of the grout impedance. However, the real component in that case is typically < 5% of the imaginary component, thus requiring highly precise measurements to give meaningful results. The impedance modulus value (very close to the imaginary component value) provided nevertheless highly useful information as shown next. Since impedance modulus-only measurements can be readily implemented in an economic field device, that measurement was therefore selected as the main metric for grout variations detection in the following. Full real/imaginary impedance measurements are therefore pending for future development as more sophisticated instrumental approaches become more viable.

The impedance sensor reporting the impedance modulus reliably identified the position of the full air void by showing a marked increase when the sensor angular position matched that of the center of the void filled with air (Figures 5.6, 5.7,5.8). The modulus increase was by a factor of two to three times when compared to the impedance over the grout in sound condition (Figure 5.8). That extent of increase also was consistent with the estimates made earlier, keeping in mind that some ac current diversion would take place by coupling with the conductive path on the sides of the void.

The impedance modulus when the sensor was over the void filled with unhydrated grout showed an increase by a factor of about 2 when compared to the impedance over the grout in sound condition (Figure 5.8). Some of this increase can be expected from less efficient packing in the dry grout powder compared with grout mixed with water, as unhydrated grout has a density of ~1.2 g/cm^3 compared to ~2 g/cm^3 for hydrated grout with 0.25 w/g. However, much of the effect was anticipated from the absence of water in the unhydrated grout, which would result in a lower effective dielectric constant and a much lower conductivity than those for the hydrated grout. The overall effect was an impedance modulus values in between those of sound grout and a full void, somewhat closer to the latter, and in any event clearly detectable.

Intriguingly, when the void was filled with the copper pellets (conductive fill) the impedance modulus also showed an increase, by a factor of ~1.5, over that of sound grout. This is the opposite of what would have been expected if the grout had been fully replaced by a more conductive medium. This apparent inconsistency can be explained by noting that the copper pellets, used to fill the void, do not fully cover the surface of the void on the inner side of the HDPE, thus introducing multiple air gaps in the zone of contact. Consequently, the local impedance is significantly higher than would have been if continuous contact existed. Therefore, the impedance for the conductive fill case was still lower than that of the void or unhydrated grout, but not quite as low as that of the sound grout. This experience indicates that the method ability to detect highly conductive fill conditions is strongly limited if voids are present near the

39

inner duct interface. Related issues are investigated in the modeling work section presented later on.

The Second series results covered a number of conditions most of which were replicated in two or more specimens, yielding mutually confirming results attesting to consistent reproducible trends. All the results concern impedance modulus only, as they were obtained with the imaging unit as configured for field tests.

The impedance trends (disregarding minor variations as the grout aged after casting) were consistent with the behavior observed in the First series regarding the differentiation between full voids and sound grout regions, with the impedance modulus of the former being consistently larger - by about a factor in the order of 2- than that of the latter (Figures 5.9 to 5.15). Also consistent with the First series findings, the presence of unhydrated grout was manifested by impedance values intermediate between those of sound grout and a full void, somewhat closer to those of the latter (Figures 5.10, 5.12 and 5.14).

The Second series provided the added opportunity to observe the behavior of voids filled with water. Figure 5.10 shows the behavior of sound grout compared with that of a full void in the center of the specimen (Duct A), a void filled with unhydrated grout, and a void filled with water. The latter had impedance values that were modestly but distinctly lower than those of sound grout, reflecting the high dielectric constant of water and a degree of ionic conductivity due to alkaline leachout from the grout in contact with the water. Similar effect of water filling is noted in Figures 5.12, 5.13 (analog presentation to that of Figure 5.10), 5.14 and 5.15. Unlike the case of the conductive copper pellets in the First series, the water closely filled the entire void space, leaving no significant gap near the inner duct surface and therefore allowing for the full effect of the highly permittivity/conductive medium to be manifested in the measured impedance changes.

Figures 5.13, 5.15 and 5.16 show cases where the impedance at a void was monitored before and while it was filled with water, as well as after the water was allowed to drain out of the filling hole. Introduction of the water had the effect noted earlier of lowering the impedance at the filled region to a value even earlier than that of sound grout. Removal of the water caused, as expected, an increase in the local impedance toward values approaching the values prevalent earlier. The increase however was not immediate. As shown in Figures 5.13 and 5.15 only a partial increase had taken place minutes after water removal. Only after a few days following removal the impedance approached the earlier, dry regime values (Figure 5.16). This behavior suggests that shortly after the bulk of the water had been removed from the void there was still a quite conductive layer of electrolyte on the inner surface of the duct in the void region. The resulting efficient path for ac current diversion, around the main capacitive path beneath the sensing plate footprint, would then lower the overall impedance compared to that of the earlier full void condition. The restoration to earlier values after a few days may then be explained by gradual evaporative or sorptive dissipation of the inner wall water film into the surrounding hardened grout.

The presence of dual voids reaching the inner wall of the duct in Duct C was clearly manifested in the impedance diagrams in Figure 5.12, as well as the effect of unhydrated grout and water filling. It is noted that the inner void in Duct D was not clearly manifested, consistent with the findings of the computer modeling section, and as discussed in more detail in Chapter 7. The limited tests with normal vs. soft grout (Figure 5.11) showed that a full void is detectable in both grout cases, but that differentiation under void-free conditions is poor. Further examination is presented in Chapter 7.

<u>Computer Modeling Investigation:</u>

Approach

In this section, the outcome of the previous sections of this chapter will be used to generate models to validate the impedance experimental measurements and further investigate frequency, plate size configurations, and different grout deficiencies.

The finite element modeling platform COMSOL Multiphysics ® V. 5.2 (COMSOL) was used to simulate the impedance behavior of the tendons at different set conditions. The modeling process investigated the following three issues, split into sections:

Section 1: Model approach validation by appropriate selection of modeling assumptions and materials properties to reproduce experimental measurements of impedance of the cast 3.5-inch nominal outer diameter tendon segments.

Section 2: Examination of the effect of plate dimensions and configuration on the ability to detect voids of various sizes and locations within the tendon cross-section.

Section 3: Examination of the effect of operating frequency on the ability to detect grout deficiencies of various configurations.

For all the modeling sections, the following terminology applies:

- Zpeak: the highest point of the modulus of impedance values in a graph plotting impedance as a function of angular position.

- Zbackground: the modulus of impedance values measured as a function of angular position for a tendon with sound grout. Zbackground is constant if the distance from the strand bundle to the inner duct surface is constant.

- Zratio: the ratio Zpeak / Zbackground. In general, the greater the Zratio, the larger the void present, with special cases noted.

Section 1: Model Validation

Model Parameters and Configurations

The steel strand configuration was first obtained by using the steel strand location detector prototype, and then, the data were imported from MATLAB to COMSOL via ImageJ (transforming a shape to a Cartesian coordinate system). Table 5.3 lists the relevant model parameters.

Figure 5.17 shows the cross-section and top view of the 3.5-inch nominal diameter tendon segment that is assessed in the models. The capacitor plate is shown in blue.

The 3D model in this and the following sections uses the Electric Currents Comsol module and assumes ac current conservation in the solid domains (polymer duct, grout) as well as in the surrounding air envelope, fixed ac potentials on the strand envelope and capacitive plate surfaces, current continuity in the medium interfaces, and isolation in the external air envelope surface.

41

Figures 5.18 and 5.19 show the two different tendon segment conditions: sound condition, and air void respectively. The modeling results are then plotted along with the experimental values for the various conditions.

Table 5.3 – Model nominal input parameters for Section 1.

Parameter	Symbol	Value	Units	Notes
Air space diameter	d_{AIR}	18	cm	
Air space length	l_{Air}	50	cm	
Grout domain diameter	d_G	7.99	cm	
Grout domain length	l_G	30	cm	
Steel strand diameter	d_{SS}	6.25	cm	
Packing factor	PF	90.7	%	
HDPE thickness	t_H	0.635	cm	
Capacitor plate length and arc length	CP_L, CP_{AL}	5, 5	cm	Extends 70 degrees tangentially
Capacitor plate thickness	t_{CP}	0.012	cm	
Air dielectric constant	ε_{AIR}	1	-	
HDPE dielectric constant	ε_H	2.2	-	
Grout dielectric constant	ε_G	52.27	-	At 1 MHz
Grout resistivity	ρ_G	394.19	Ω-m	At 1 MHz

Model Results

The experimental and model values of impedance (Figures 5.20-5.23) show a great deal of similarity, confirming the suitability of the grout electrical conductivity and relative permittivity parameter values that were determined with the procedure detailed in Appendix A. Hence the model and parameter values choices were deemed to be a useful tool to examine the different plate configurations and void configurations in the next section.

It is noted that the model output for the air filled void (Figure 5.23) showed a small shift relative to that obtained experimentally. This may be due to a slight rotational shift of the Styrofoam piece when the grout was cast. However, these deviations are thought to be of secondary importance given the similar Zratio between the experimental and model responses.
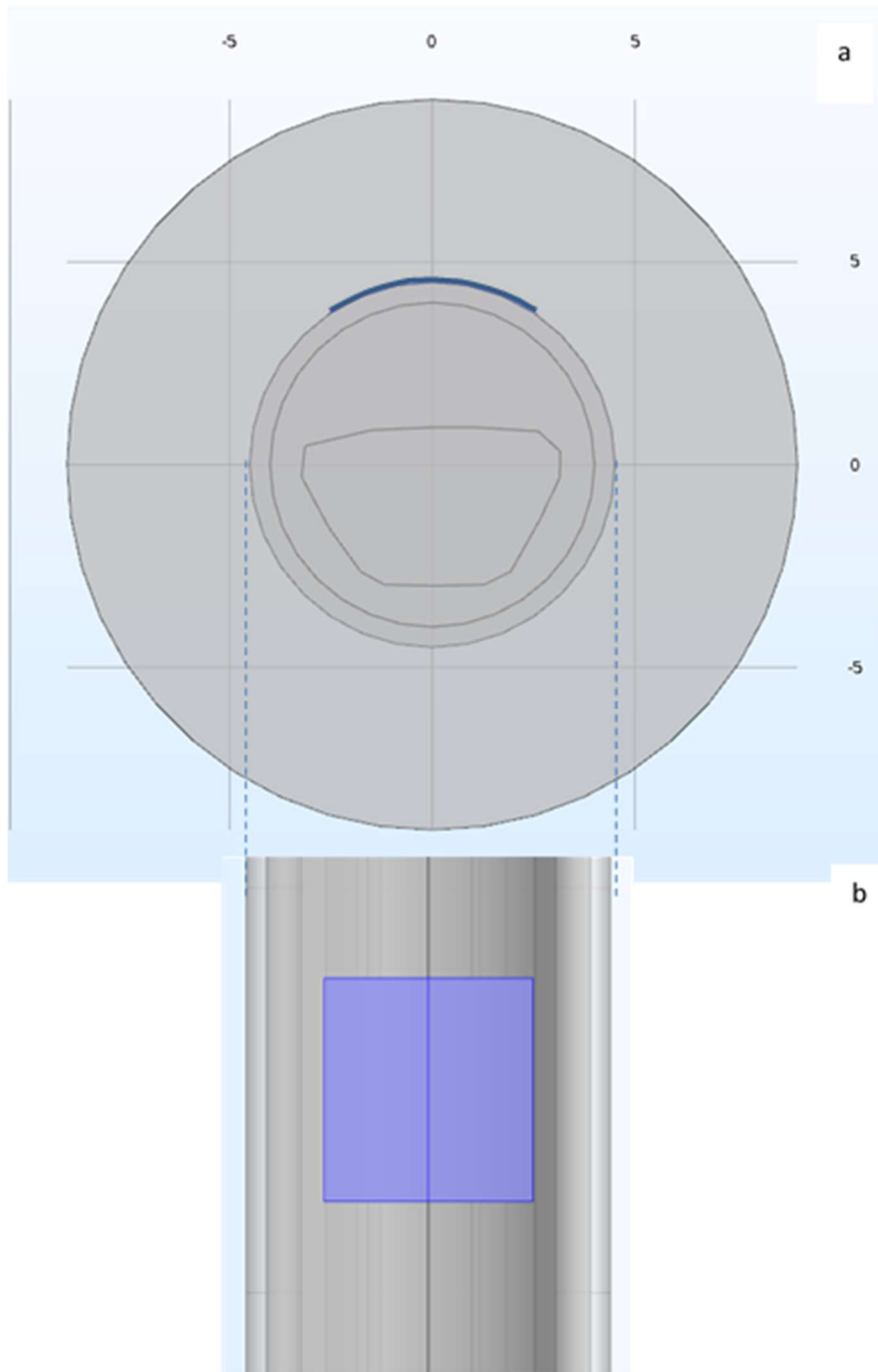
Figure 5.17 (a) – Cross-sectional view of 3.5-inch (8.9-cm) nominal outer diameter tendon with steel strand envelope imported from steel strand location detector prototype. The tendon is surrounded by a 9-cm radius air cylinder to represent field and laboratory conditions. (b)– Top view of 5 cm x 5 cm plate used for model (edge view on (a)). Grid scale is in cm.
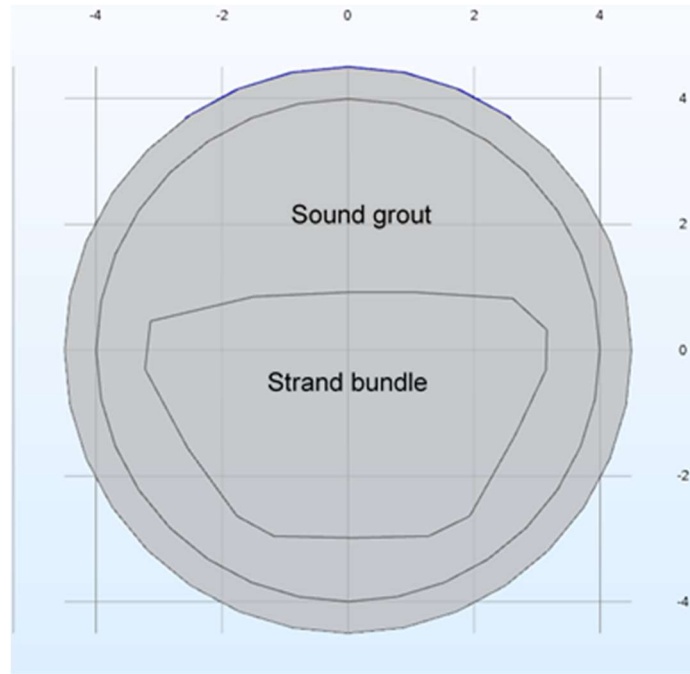
Figure 5.18 Cross-sectional view of 3.5-inch diameter with sound grout.
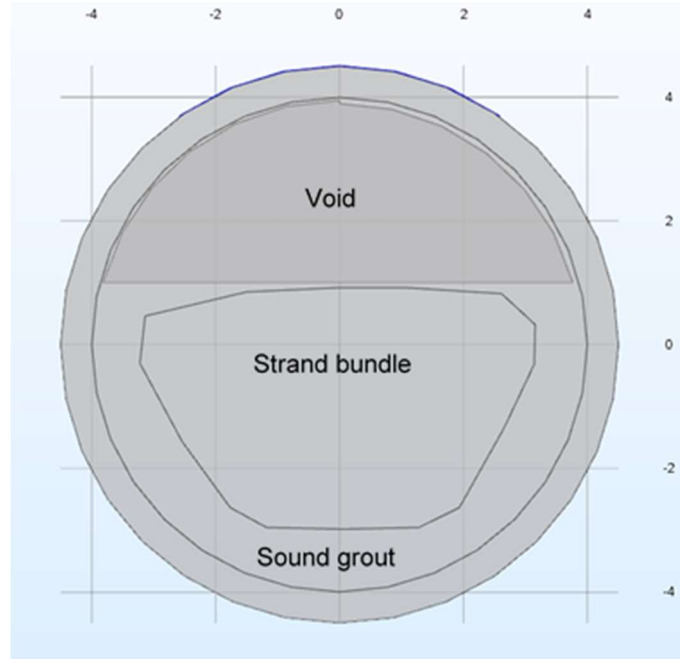
Figure 5.19 cross-sectional view of 3.5-inch nominal diameter tendon with a 4-inch long air-filled void at the center.
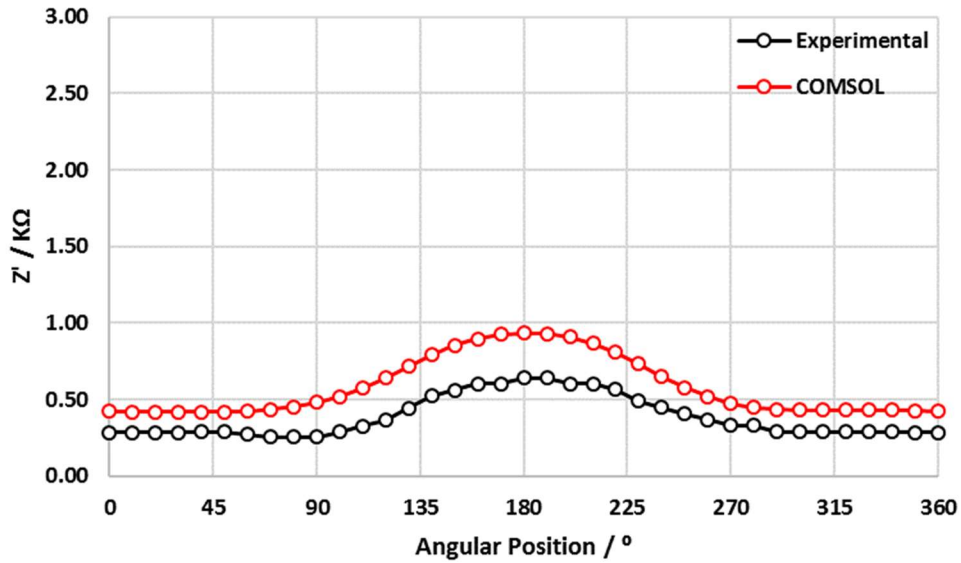
Figure 5.20 Real impedance value vs. angular position of the tendon (sound grout) showing the experimental values (from Figure 5.6) and the model values at 1 MHz for the profile in Figure 5.18. The model results follow the experimental trends.
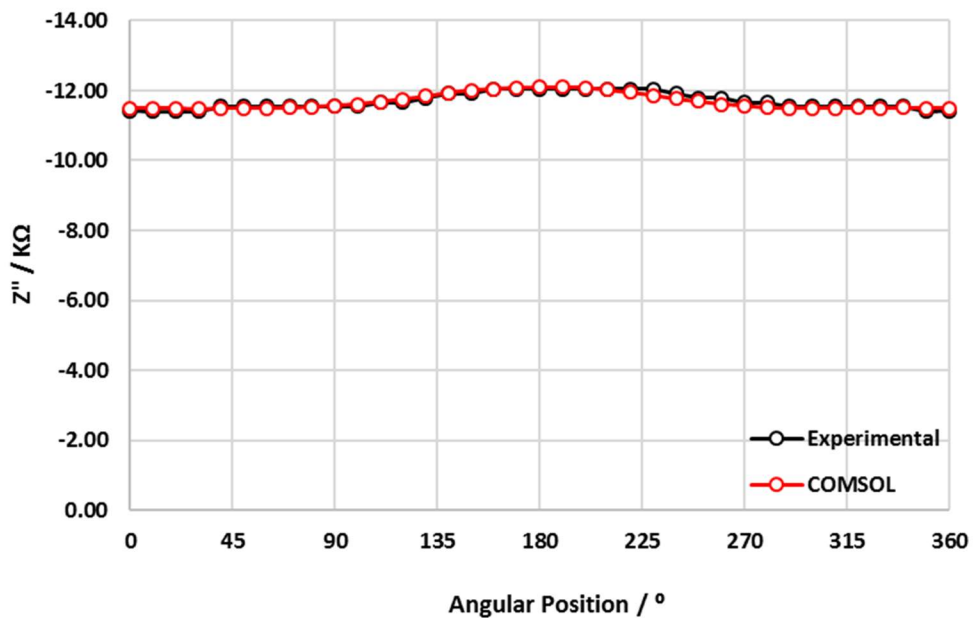
Figure 5.21 Imaginary impedance value vs. angular position of the tendon (sound grout) showing the experimental values (Figure 5.7) and the model values at 1 MHz for the profile in Figure 5.18. The model results follow the experimental trends.
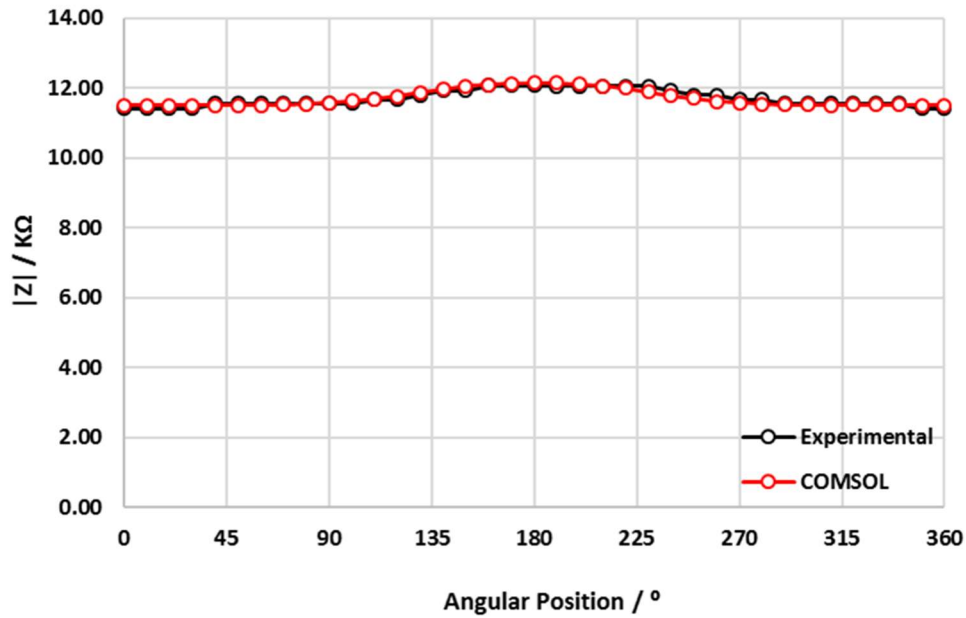
Figure 5.22 Modulus of impedance vs. angular position of the tendon (sound grout) showing the experimental values (from Figure 5.8) and the model values at 1 MHz for the profile in Figure 5.18. The model results follow the experimental trends.
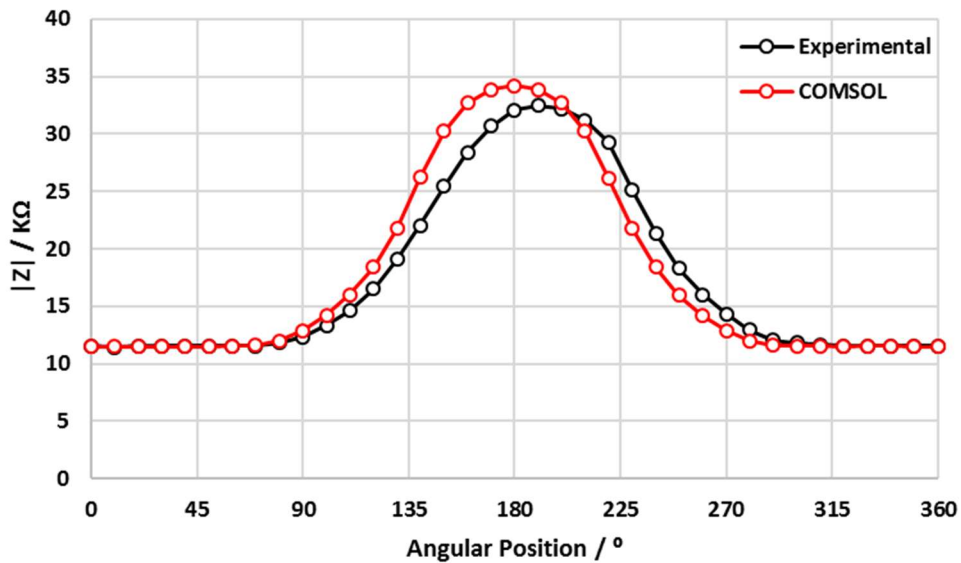
Figure 5.23 Modulus of impedance vs. angular position of the tendon (with air void) showing the experimental values (from Figure 5.9) and the model values at 1 MHz for the profile in Figure 5.19. The model results follow the experimental trends.

46

Section 2: Ability to Detect Voids - Model Exploration

After the validation of the selection of modeling assumptions and material property values by showing consistency with the experimental measurements, scenarios were explored that supplement the limited set of conditions that can be examined experimentally. Those include determining the effect of plate dimensions on imaging of grout deficiencies (in this case, air filled voids), and the possible advantage of using a guarded electrode plate configuration.[A]

Model Parameters and Configurations

For this set of models an idealized circular central 12-strand bundle configuration was chosen. Strand cross-sections (simplified as ½ inch diameter circles) were assumed to be close-packed, resulting in an area packing factor of 90.7%, yielding an idealized bundle diameter of 2.25 inch. The parameters for the tests are given in Table 5.4.

Table 5.4 – Model nominal input parameters for Section 2.

Parameter	Symbol	Value	Units	Notes
Air space diameter	d_{AIR}	18	cm	
Air space length	l_{Air}	50	cm	
Grout domain diameter	d_G	7.99	cm	
Grout domain length	l_G	30	cm	
Steel strand diameter	d_{SS}	2.25	cm	
HDPE thickness	t_H	0.505	cm	
Capacitor plate length 1 and arc length 1	CP_L, CP_{AL}	5, 5	cm	
Capacitor plate length 2 and arc length 2	CP_L, CP_{AL}	5, 2.54	cm	
Capacitor plate thickness	t_{CP}	0.012	cm	
Air dielectric constant	ε_{AIR}	1	-	
HDPE dielectric constant	ε_H	2.2	-	
Grout dielectric constant	ε_G	52.27	-	At 1 MHz
Grout resistivity	ρ_G	394.13	Ω-m	At 1 MHz

[A] The guard electrodes send current to the strand bundle but only the current from the central electrode is used in computing the value of the impedance. This configuration assists in avoiding uncertainty from current straying on a wider pattern than the footprint of the central electrode.

The following models are for a void that spans an angular slice 58 degrees wide in the tendon cross-section. The void size and shape were laid out in three variations:

1. Full: the void starts at the steel strand envelope edge and extends all the way to the HDPE inner surface (Figure 5.24).

2. Outer: the void starts at an intermediate radius in the grout and extends to the HDPE inner edge (Figure 5.25).

3. Inner: the void starts at the steel strand envelope and ends at an intermediate radius in the grout (Figure 5.26).

Three different plate configurations were addressed:

1. A full 5 cm x 5 cm plate which covers 70 degrees of the tendon at a time (Figures 5.24-5.26and 5.30-5.32.

2. A 2.54 cm x 5 cm plate which covers 20 degrees of the tendon at a time (Figures 5.27-5.29).

3. A guard-electrode composite plate which splits the 5 cm wide configuration into a 20 degree central portion and two 25 degree guard electrodes on each side [50] (addressing the void configurations in Figures 5.24-5.26 or 5.27-5.29)

Conditions examined were coded, for example:

T70 58 Full indicating plate spanning 70 degrees (standard 5 cm x 5 cm plate), with a Full void spanning a 58-degree slice.

T20 58 Outer indicating plate spanning 20 degrees (2.54 cm x 5 cm plate), with an Outer void spanning a 58-degree slice.

T70P at 20 58 Inner indicating a guard electrode composite plate configuration partitioned at 20 degrees (the central electrode is 2.54 cm x 5 cm plate), with an Inner void spanning a 58-degree slice.

Additional void configurations were addressed in models for a larger duct diameter (4 inch nominal diameter) more typical of field tendons, for narrow and wide plate configurations (Figures 5.30-5.32). The simulations represented voids that may occur at the top of the grout cross-section due to insufficient grout filling.

The cross-sectional areas and void angular slices were:

Void #1: area ~4.12 cm^2, angular slice ~73° (Figure 5.30).
Void #2: area ~2.44 cm^2, angular slice ~61° (Figure 5.31).
Void #3: area ~1.06 cm^2, angular slice ~46° (Figure 5.32).

The modeling results are plotted in Figures 5.33-5.37.

Model Results

Based on the results shown in Figures 5.33-5.37 the following was concluded:

- Full and Outer voids are easily identified using any plate configuration (Wide plate, narrow plate, and guard electrode plate system).

- The plate arc length did not seem to greatly impact the results. However, it is noticed that the Zratio of the modulus of impedance for the void over the modulus of impedance of the sound grout (background impedances) increased (a more desirable outcome) when the plate arc length was smaller. The guard electrode plate configuration showed even greater ratios of modulus of impedance of void with respect to sound grout.

- All the above configurations are feasible for possible eventual implementation, with choice beyond a simple plate depending on evaluation of the benefits to be derived vis a vis complexity of instrumentation.

- Inner voids were harder to detect but still showed a noticeable change in the modulus of impedance. That occurrence would still likely show as an anomaly that when put together with the data from the Steel Strand Location Detector Prototype could alert the user of an issue needing attention.
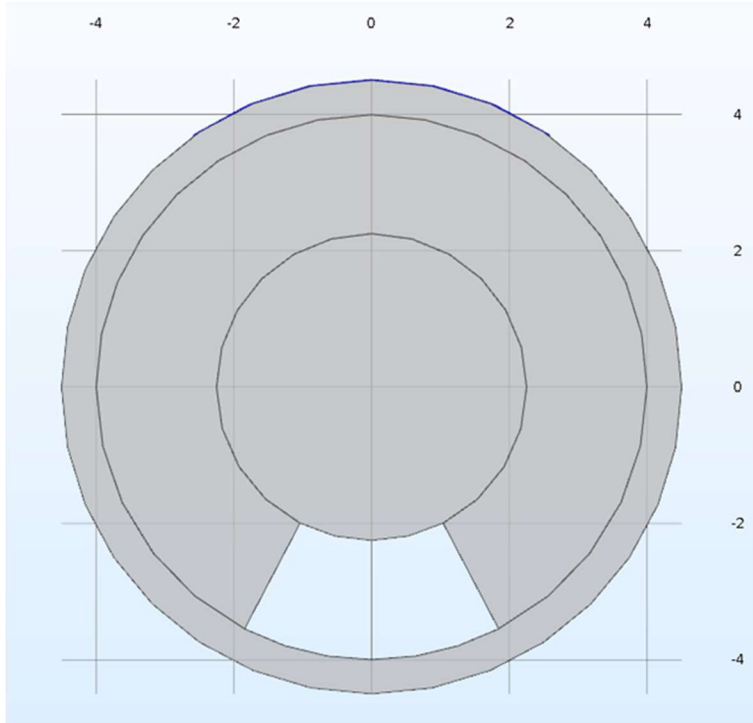
Figure 5.24 Cross-sectional view of 3.5-inch nominal diameter tendon, with a Full 58-degree void. The plate (blue line on perimeter) is 5 cm x 5 cm.
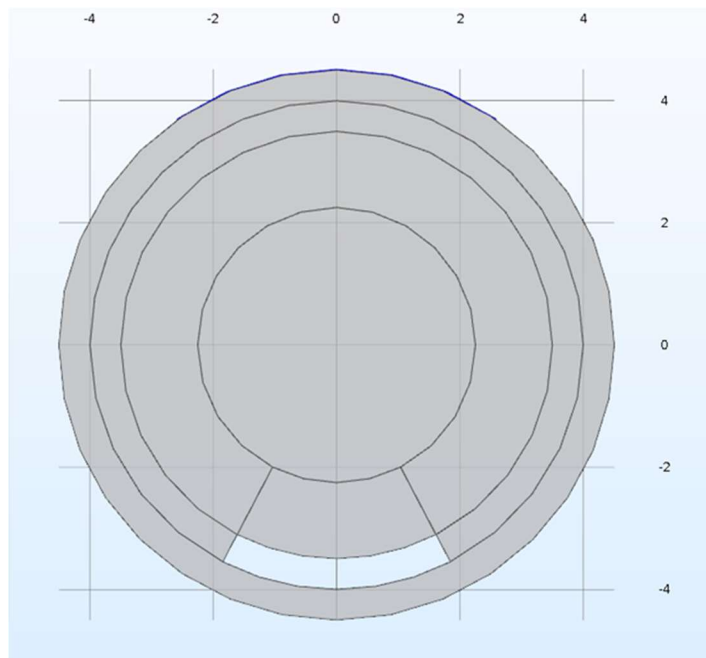
Figure 5.25 Cross-sectional view of 3.5-inch nominal diameter tendon, with an Outer 58-degree void. The plate is 5 cm x 5 cm.
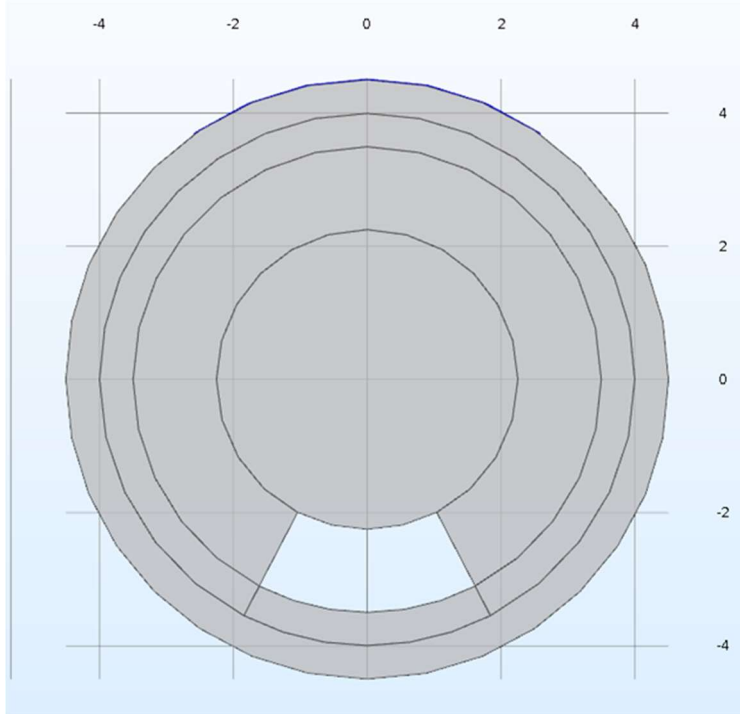
Figure 5.26 Cross-sectional view of 3.5-inch nominal diameter tendon, with an Inner 58-degree void. The is plate 5 cm x 5 cm.
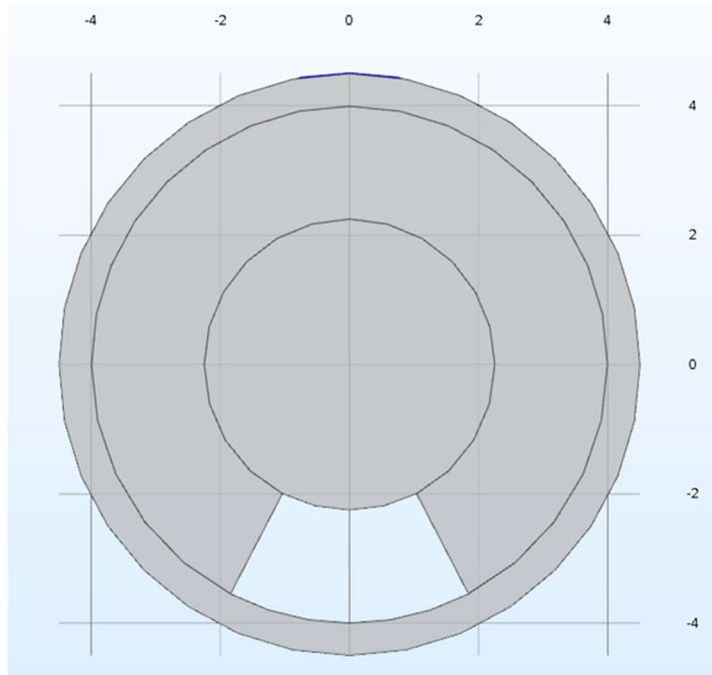
Figure 5.27 Cross-sectional view of 3.5-inch nominal diameter tendon, with a full void. The plate is 2.54 cm x 5 cm.
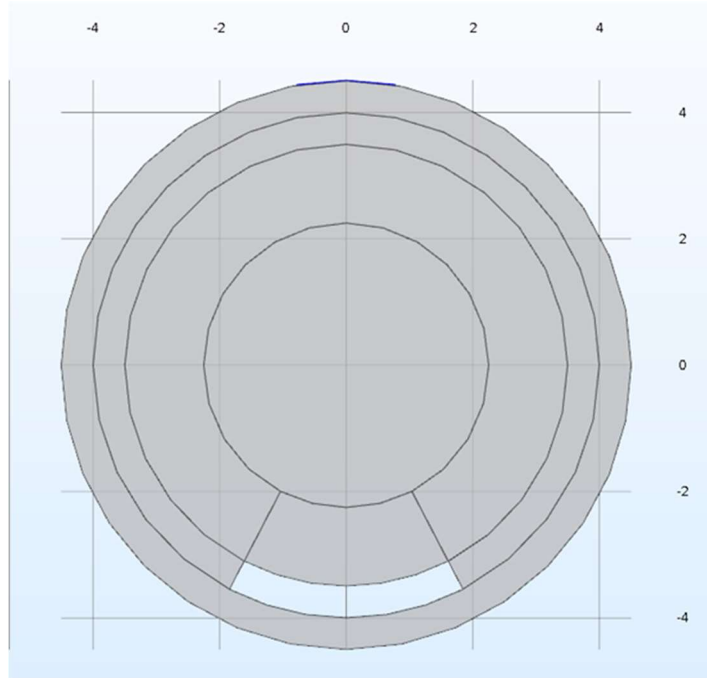
Figure 5.28 Cross-sectional view of 3.5-inch nominal diameter tendon, with an outer void. The plate is 2.54 cm x 5 cm.
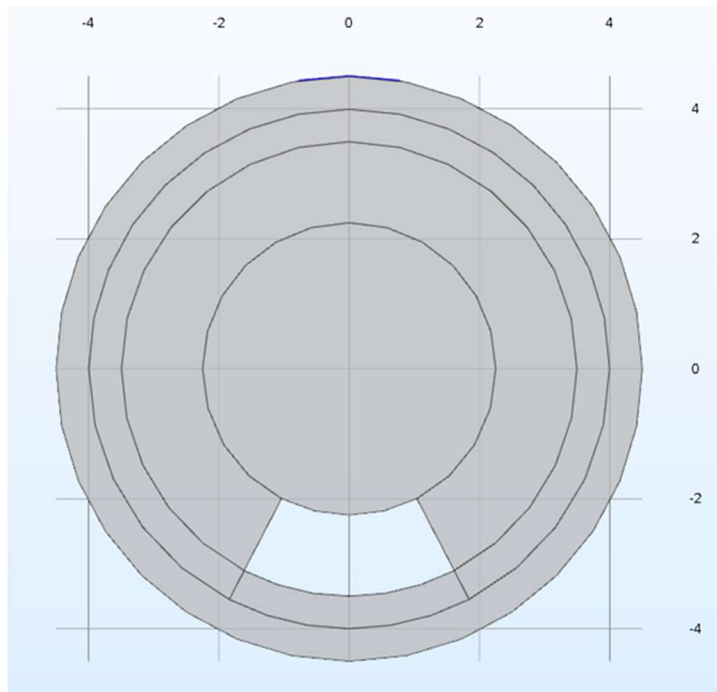
Figure 5.29 Cross-sectional view of 3.5-inch nominal diameter tendon, with an inner void. The plate is 2.54 cm x 5 cm.
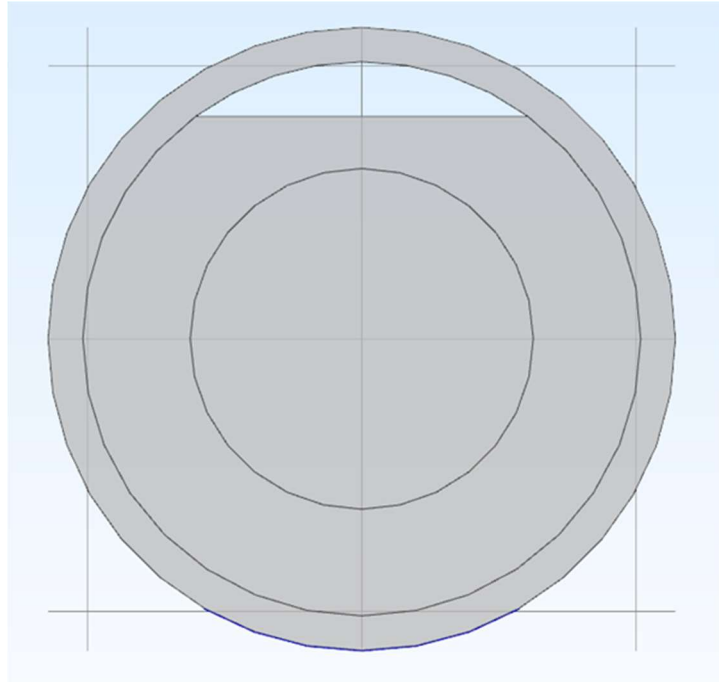
Figure 5.30 Cross-sectional view of 4-inch nominal diameter tendon, with Void #1. The plate is 5 cm x 5 cm.
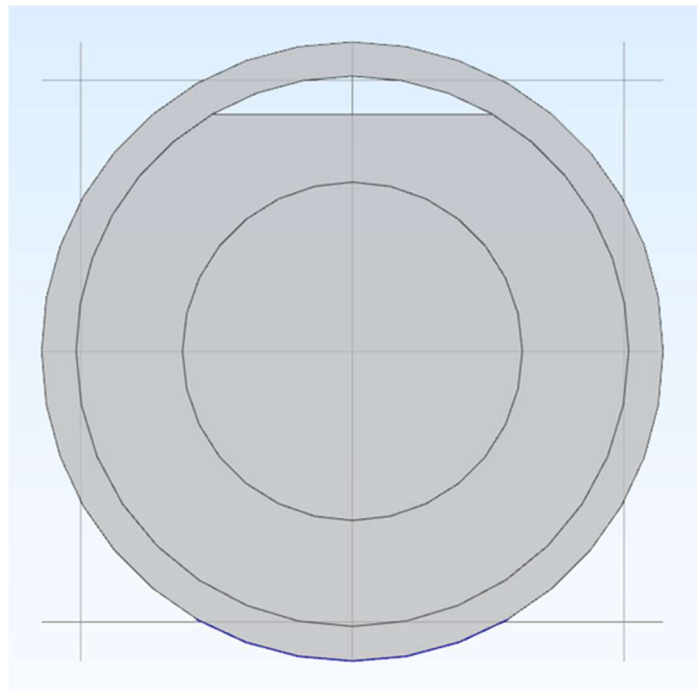
Figure 5.31 Cross-sectional view of 4-inch nominal diameter tendon, with Void #2. The plate is 5 cm x 5 cm.
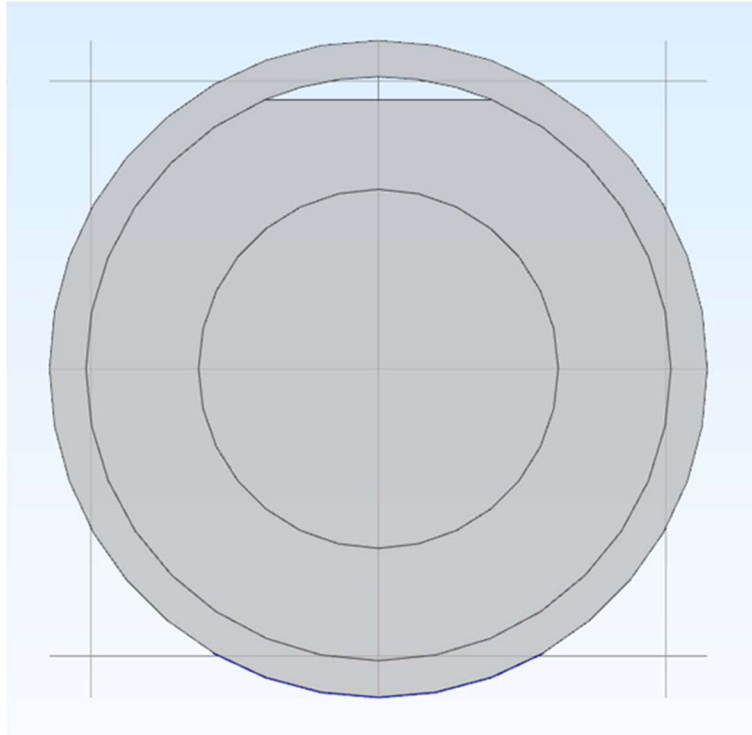
Figure 5.32 Cross-sectional view of 4-inch nominal diameter tendon, with Void #3. The plate is 5 cm x 5 cm.
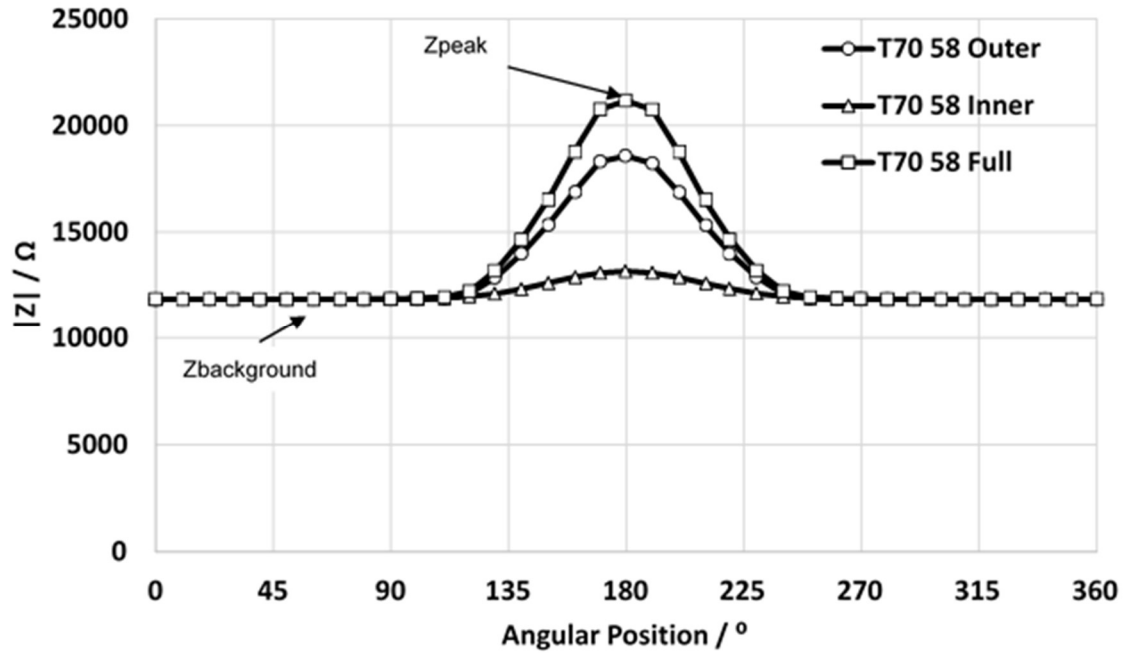
Figure 5.33 Modulus of impedance vs. angular position of the tendon showing the model values for a full, outer and inner void at 1 MHz for the profiles in Figure 5.24-5.26. The plates used for these models are 5 cm x 5cm.
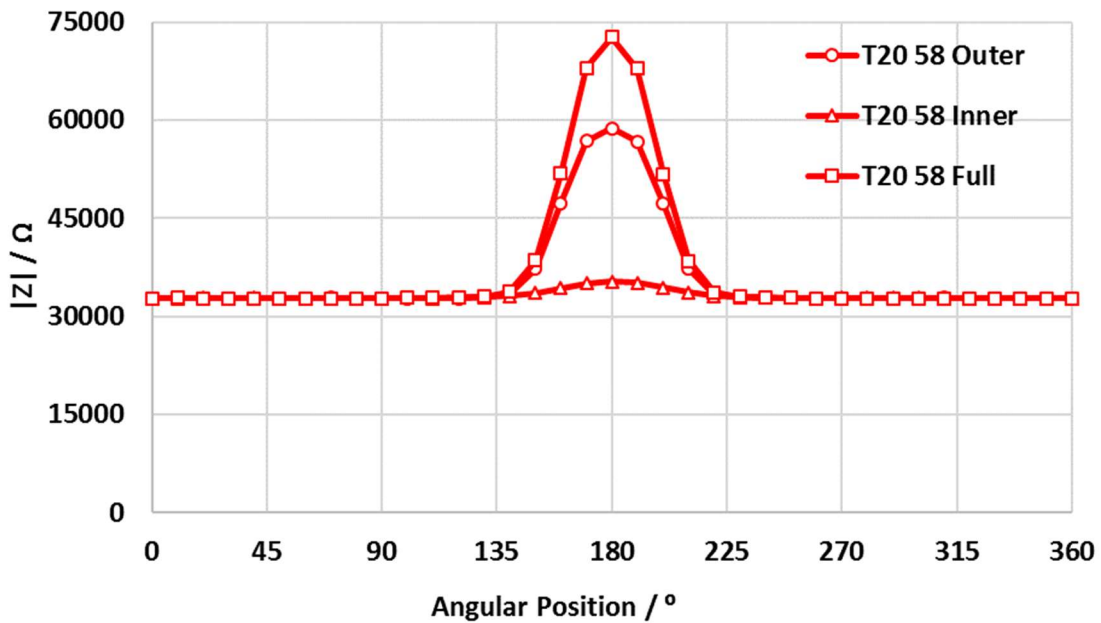
Figure 5.34 Modulus of impedance vs. angular position of the tendon showing the model values for a full, outer, and inner void at 1 MHz for the profiles in Figure 5.27-5.29. The plates used are 2.54 cm x 5 cm.
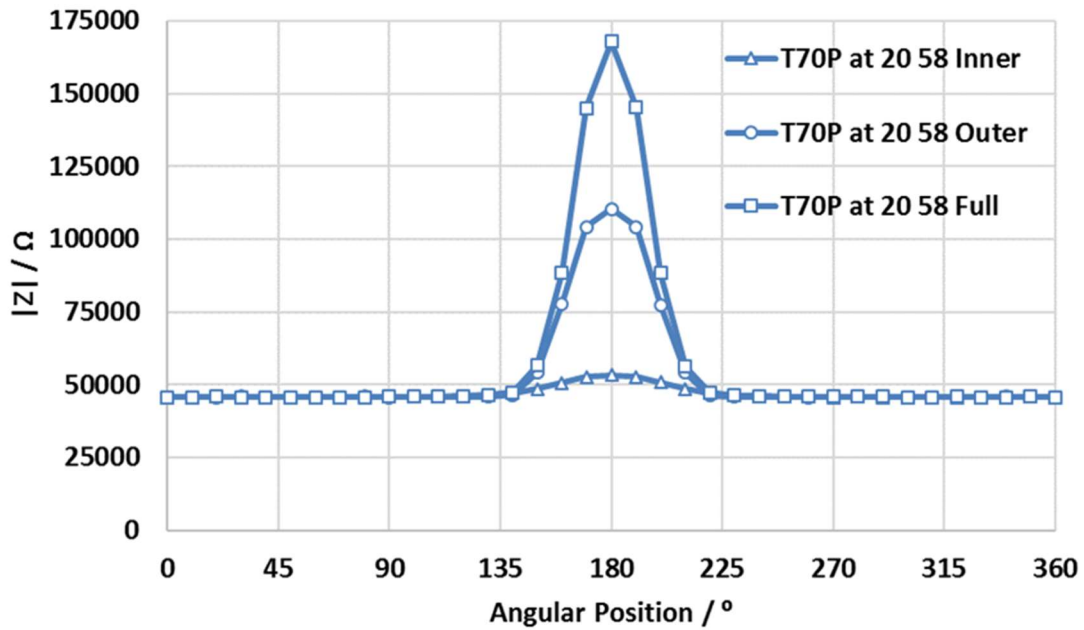
Figure 5.35 Modulus of impedance vs. angular position of the tendon showing the model values for a full, outer, and inner void at 1 MHz for the profiles in Figure 5.24-5.26. The plates used are guarded.

For the three void sizes as seen in Figures 5.30-5.32 the impedance output of the models at 1 MHz was calculated using the two capacitor plate configurations (5 cm x 5 cm & 5 cm x 2.54 cm). Using the smaller plate configurations showed a better impedance profile for each of the voids assessed. The impedance profiles are seen in Figures 5.36-5.37.
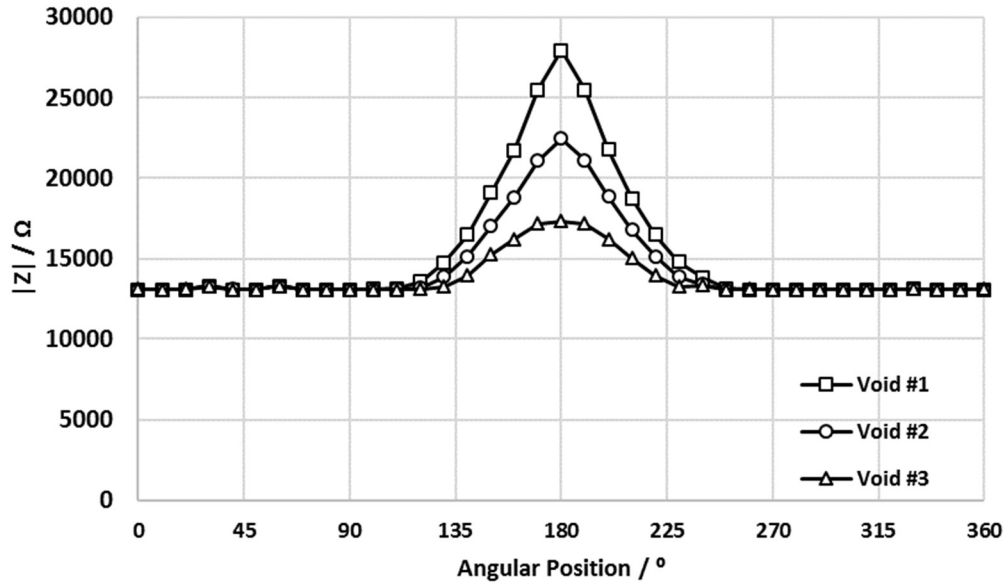
Figure 5.36 Modulus of impedance vs. angular position of the tendon showing the model values for three different-size voids at 1 MHz for the profiles in Figure 5.30-5.32. The bigger the void, the higher the modulus of impedance value. The plates used for these models are 5 cm x 5 cm.
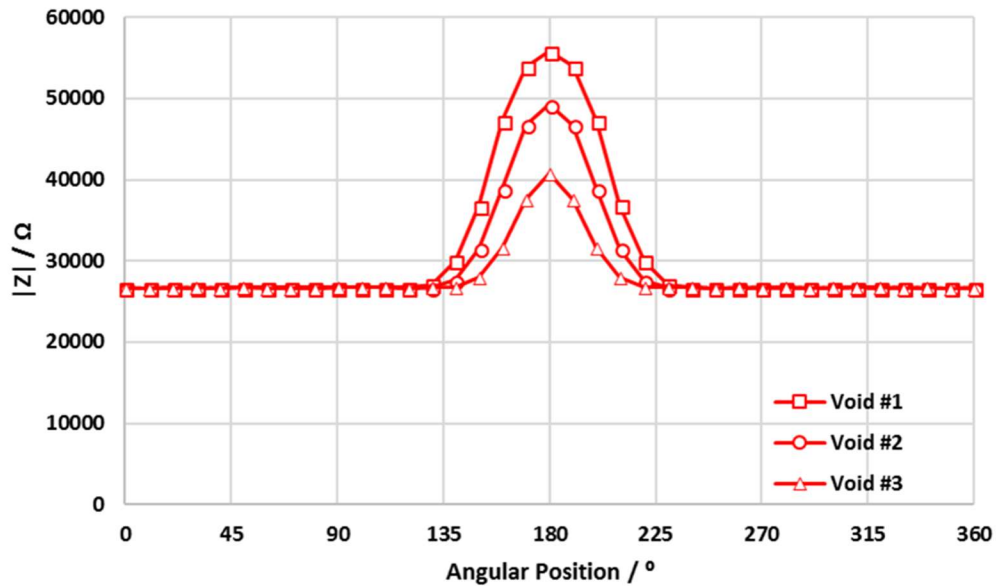
Figure 5.37 Modulus of impedance vs angular position of the tendon showing the model values for three different-size voids at 1 MHz for the profiles in Figure 5.30-5.32. The bigger the void, the higher the modulus of impedance value. The plates used for these models are 2.54 cm x 5 cm.

Section 3: Higher Frequency Exploration

Model Parameters and Configurations

The previous section established the effect of plate dimensions and configuration on the ability to detect voids of various locations within the tendon cross-section. The next step, addressed here, was to determine the effect of the operating frequency on the ability to detect grout deficiencies of various configurations, for possible optimization of the method. Conditions examined are summarized in Table 5.5.

The reason for using higher frequencies is that while the impedance of the HDPE duct wall decreases quite predictably with f^{-1} (HDPE being a nearly ideal dielectric), the impedance of the grout tends to decrease with f-n, given the CPE behavior of the grout (Appendix A, Eq. 8). Since n<1, then, as the test frequency increases, the impedance of the grout filling the duct will tend to increase relative to that of the duct wall, making it easier to reveal deficiencies of the grout, compared with the case of lower test frequencies. Consequently, model calculations were conducted for elevated frequencies of 10 MHz (an easily achievable condition without the need of sophisticated equipment) and 500 MHz (somewhat more complicated to implement but still within the range of commonly available ultra-high frequency (UHF) communications equipment).

The calculations were conducted for two groups of idealized tendon and grout configurations, per the Table 5.6 listing. The first group (tendons 1, 2 and 3, with configurations shown in Figures 5.38-5.40, respectively) were 4-inch nominal diameter tendons (approaching field usage) with voids of decreasing size extending from the inner wall of the duct toward a central idealized strand bundle, having configurations designated –following notation from the previous section– as full (tendon 1) and outer (tendons 2 and 3). For these tests, the capacitor plate was chosen to be 2.54 cm wide and 5 cm long, designated as a narrow (N) plate. The second group (tendons 4, 5, and 6) corresponded to the configurations already introduced in Figures 5.24-5.26, respectively, fitted with capacitor plates 5 cm wide and 5 cm long, hence designated as a wide (W) plate. The voids in this second grout group included three cases designated as full, outer, and inner, as in the previous section. Moreover, two ways of calculating impedance at higher frequencies were used. The first used the CPE constants per the data in Appendix A. The second used data from the literature for independent tests conducted at 500 MHz and as reported by Soutsos et al. [51], symbolized here by the acronym NGH.

Model Results

The results for the first group are show in Figure 5.41. The logarithmic scale permits comparison of the relative differentiation at the various frequencies. The results show that there is virtually no change in relative response when varying frequency from 1 to 10 MHz; for all three voids, the dominant factor is the presence of the void directly after the polymer duct wall; the thinner the void, the lower is its impedance, so the central hump is least manifested for the Tendon 3 case. At 500 MHz, all three maxima at the void position are depressed in the same relative amount so not much relative differentiation is observed. Hence, for voids of this type (directly after the duct wall), the increase to much higher test frequencies than 1 MHz did not appear to provide much benefit.

Table 5.5 – Model nominal input parameters for Section3

Parameter	Symbol	Value	Units	Notes
Air space diameter	d_{AIR}	18	cm	
Air space length	l_{Air}	50	cm	
Grout domain diameter	d_G	10.16	cm	
Grout domain length	l_G	30	cm	
Steel strand diameter	d_{SS}	6.25	cm	
Packing factor	PF	90.7	%	
HDPE thickness	t_H	0.635	cm	
Capacitor plate length 1 and arc length 1	CP_L, CP_{AL}	5, 5	cm	
Capacitor plate length 2 and arc length 2	CP_L, CP_{AL}	5, 2.54	cm	
Capacitor plate thickness	t_{CP}	0.012	cm	
Air dielectric constant	ε_{AIR}	1	-	
HDPE dielectric constant	ε_H	2.2	-	
Grout dielectric constant	ε_G	52.27	-	At 1 MHz
Grout resistivity	ρ_G	394.19	Ω-m	At 1 MHz
Grout dielectric constant	ε_G	29.56	-	At 10 MHz
Grout resistivity	ρ_G	113.34	Ω-m	At 10 MHz
Grout dielectric constant[B]	ε_G	10	-	At 500 MHz
Grout resistivity[2]	ρ_G	7.66	Ω-m	At 500 MHz
Grout dielectric constant[C][51]	ε_G	7	-	At 500 MHz
Grout resistivity[3]	ρ_G	16.67	Ω-m	At 500 MHz

[B] Grout dielectric constant and resistivity are calculated using Appendix A equations (8,9) for model input which assume a CPE behavior.
[C] Grout dielectric constant and resistivity values are obtained from M.N Soutsos et at.[51]. (NHG) where they conducted research on how dielectric properties of concrete are influenced from radar testing with various frequencies

Table 5.6 – Frequency Variation Exploration

Tendon	Plate Width N or W	Case	Frequency MHz	Dispersion CPE or NHG
1 (Full)	N	1	1	CPE
		2	10	
		3	500	
2 (Outer-Thick)		4	1	
		5	10	
		6	500	
3 (Outer-Thin)		7	1	
		8	10	
		9	500	
4 (Full)	W	10	1	CPE
		11	500	
		12	500	NGH
5 (Outer-Thick)		13	1	CPE
		14	500	
		15	500	NGH
6 (Inner-Thin)		16	1	CPE
		17	500	
		18	500	NGH

Results for the second group of tendons are shown in Figures 5.42 and 5.43. Since the results for Group 1 show little sensitivity to changes from 1MHz to 10 MHz, the Group 2 calculations were limited to 1MHz and 500 MHz, exploring instead two different ways of estimating the grout dielectric behavior (CPE extrapolation and use of literature values for 500 MHz tests (NHG, [51]), Table 5.5). Figure 5.42, based on CPE-estimated grout behavior), shows notable improvement in void detection when going from 1 MHz to 500 MHz. At 1 MHz the inner void (that is, extending only halfway from the strand bundle toward the duct, but not reaching it) produced a much lower impedance hump signature than that of the outer void although both voids were of comparable thickness. That effect had been noted already in Section 3 and was ascribed to shielding by the relatively large admittance of the grout at that frequency. The relative manifestation of the inner void was much improved at 500 MHz; there both the inner and outer voids yielded nearly identical hump signatures, and both were about half of that of the full void. That highly desirable Zratio response sequence amply validating the expectations when exploring the higher frequency regime.

Moreover, the results in Figure 5.43 showed that the improved sensitivity to inner voids was retained when using an alternative means of evaluating the higher frequency dielectric grout properties, indicating that the results in Figure 5.42 were not simply a happenstance. These results are encouraging; the practical implementation of operation at frequencies in the order of 500 MHz or higher that next generation imaging should be explored in follow up work.
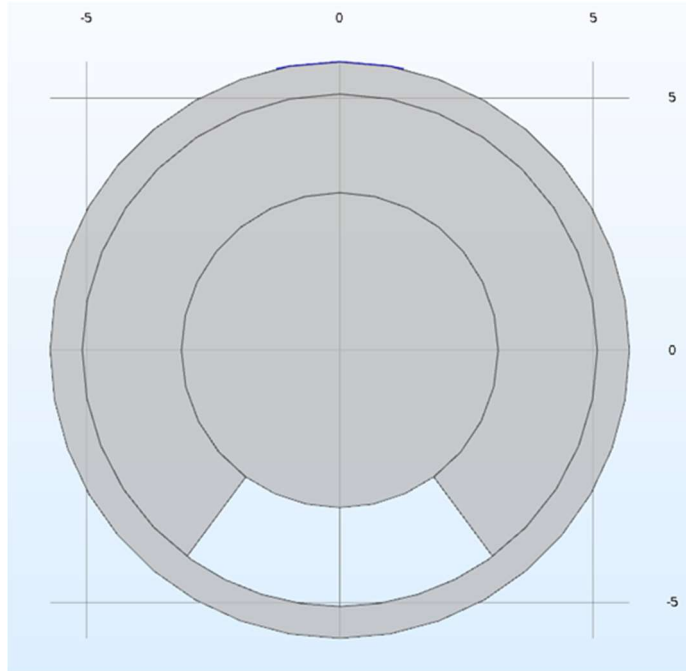
Figure 5.38 Cross-sectional view of 4-inch nominal diameter tendon with a Full ~73° void and a 1 inch wide plate. (Table 5.6, Tendon 1)
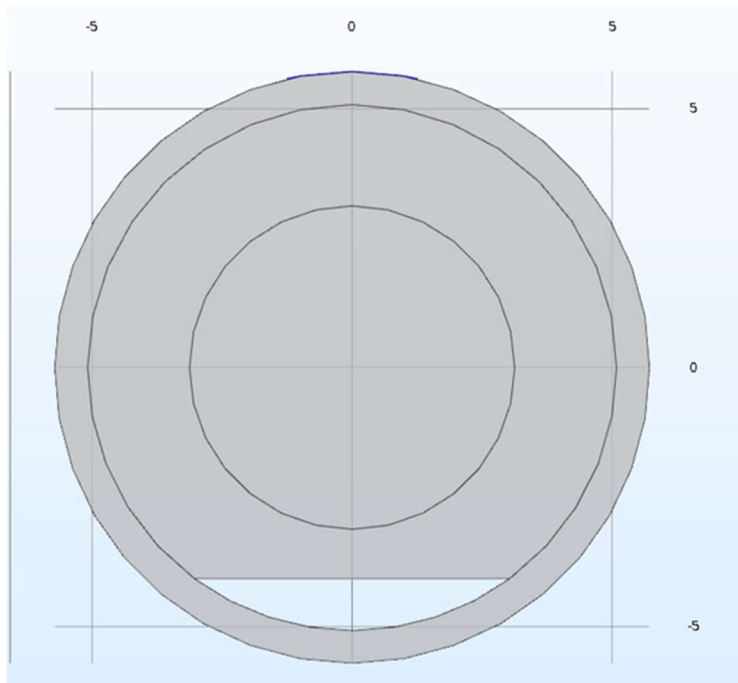
Figure 5.39 Cross-sectional view of 4-inch nominal diameter tendon with Void #1(~73°) and a 1 inch wide plate. (Table 5.6, Tendon 2)
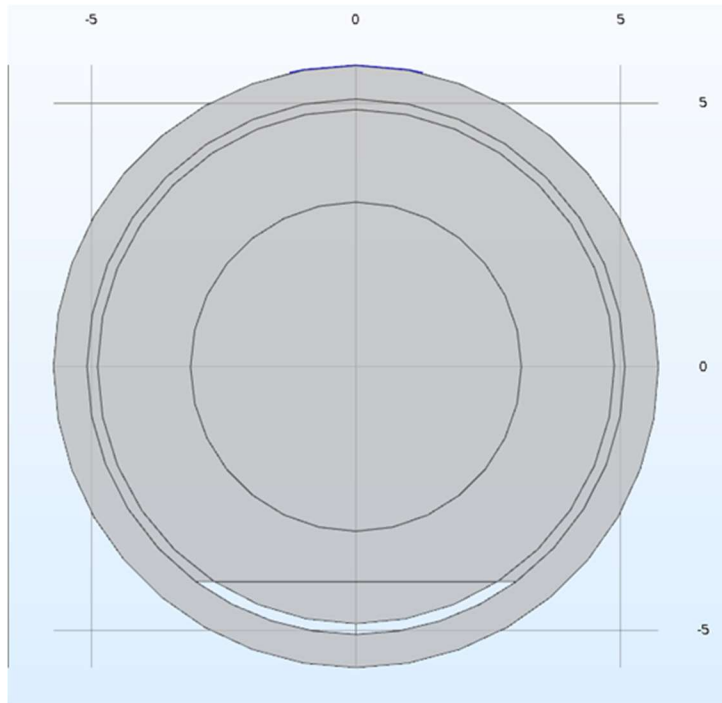
Figure 5.40 Cross-sectional view of 4-inch nominal diameter tendon with a 2-mm -thick (~73º) void and a 1-inch-wide plate. (Table 5.6, Tendon 3)
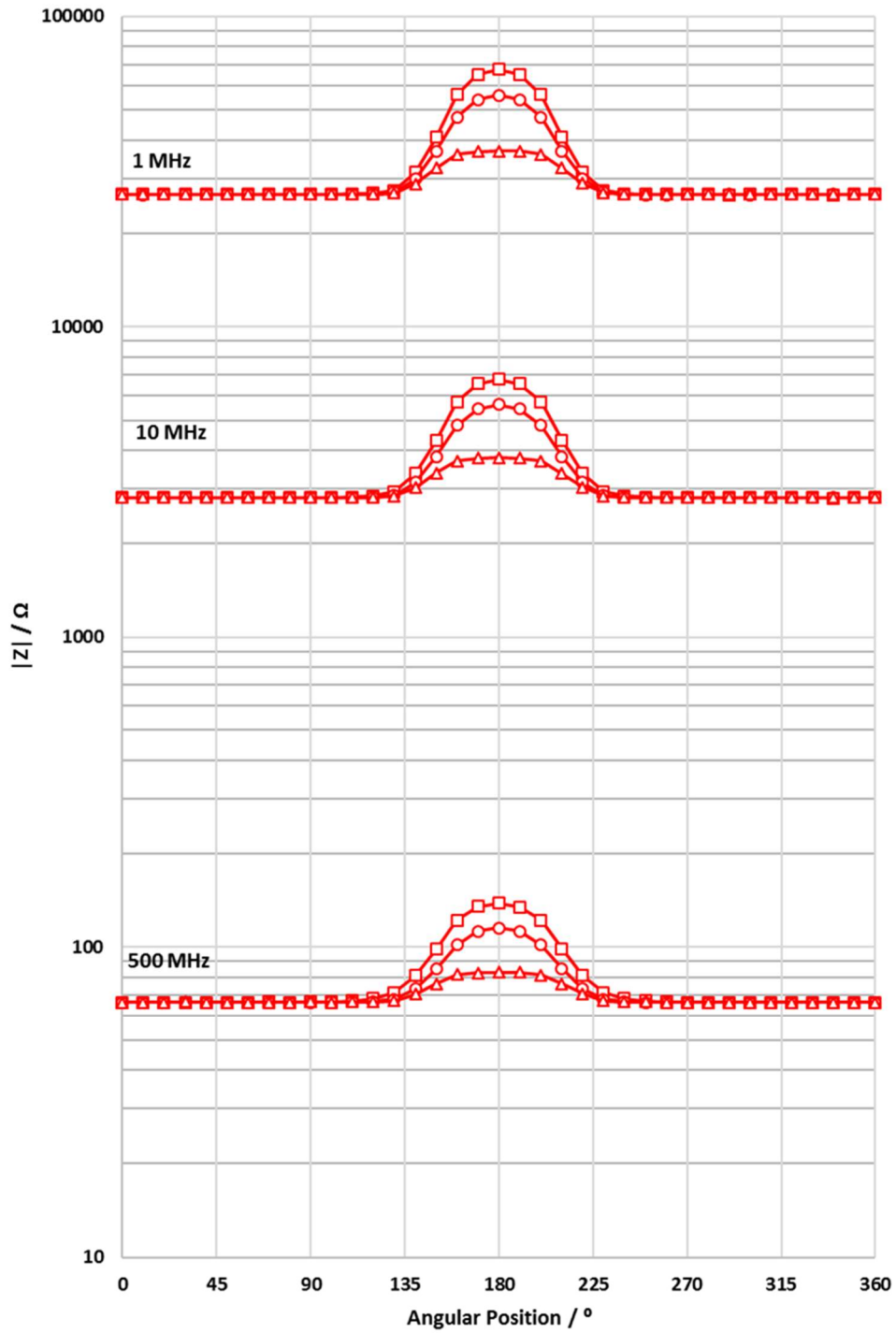
Figure 5.41 Modulus of impedance vs. angular position for Table 5.6; Tendons 1(squares), 2 (circles), and 3 (triangles) at 1 MHz, 10 MHz, and 500 MHz. Log scale is used for the y-axis to show comparison of the output of the frequencies on the same graph. The plates used for these calculations are 2.54 cm (Narrow) x 5 cm.
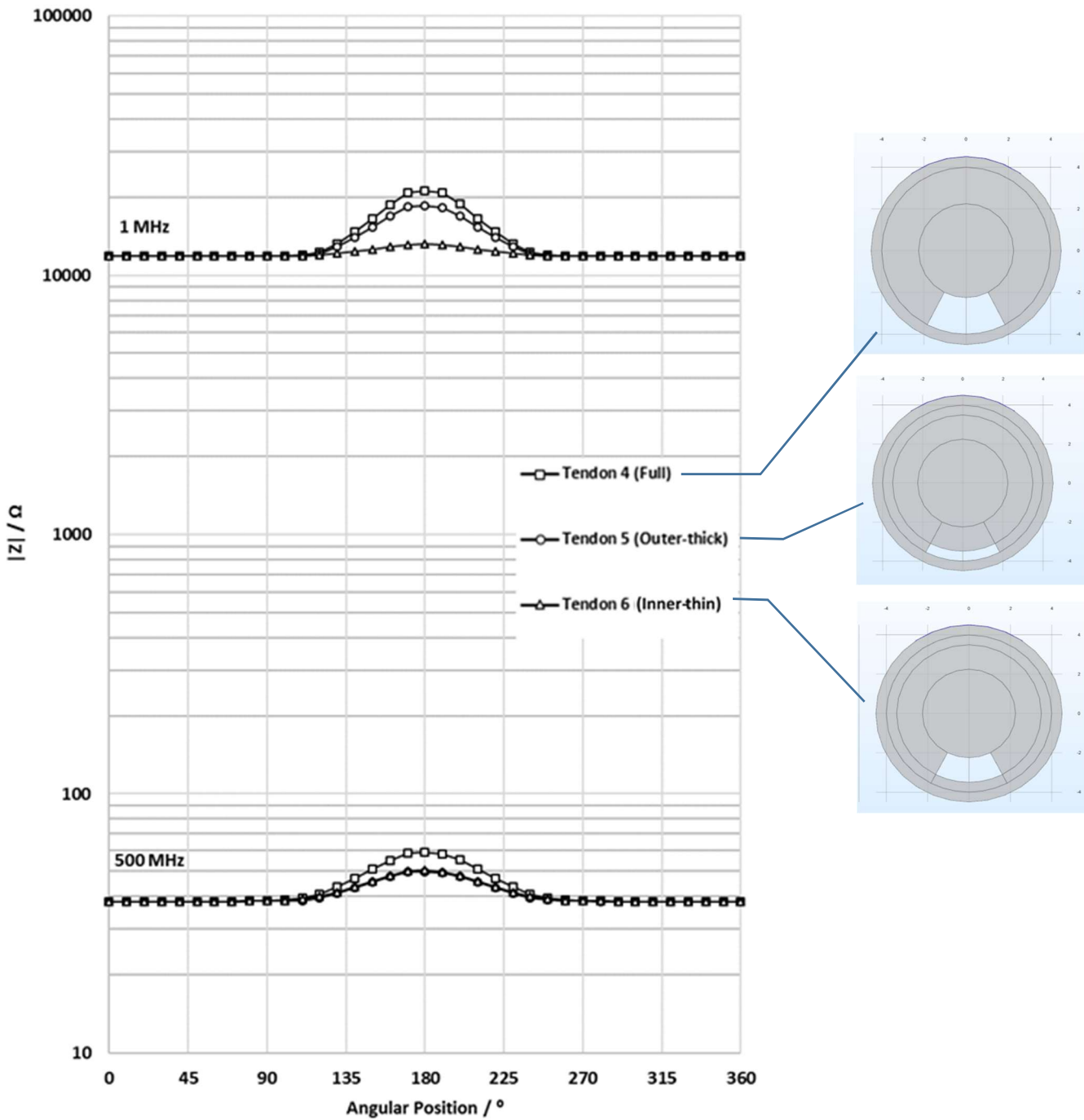
Figure 5.42 Modulus of impedance vs. angular position for Table 5.6; Tendons 4, 5, and 6 at 1 MHz and 500 MHz. Log scale y-axis permits direct comparison of relative descriptors. Note that at 1 MHz, the outer void is strongly apparent, but the inner void is barely detectable. Using 500 MHz instead, the results can identify the void regardless of whether it is on the outer part of the cross-section or buried deeper.
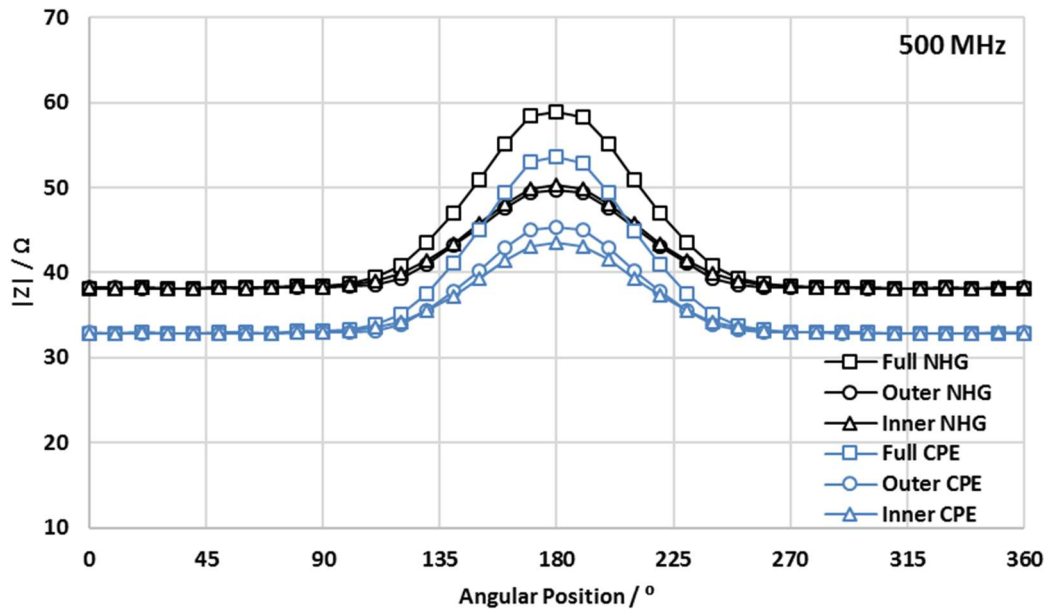
Figure 5.43 Modulus of impedance vs. angular position of the tendons addressed in Figure 5.34, using two alternative means of estimating high frequency grout dielectric behavior. The series in black are calculated using NHG input parameter, and the blue series are from the CPE input parameters.

Chapter Summary

The impedance between an external travelling plate and the strand bundle can be abstracted as the sum of the impedance of the HDPE polymer duct and the grout space, which may include an anomaly. The HDPE polymer duct impedance is normally the dominant term. An impedance sensor (measuring at 1 MHz) shows a clear differentiation between sound grout and grout with an anomaly in the form of a full void, multiple voids, or a void filled with unhydrated grout. Sensitivity to a water-filled void, or the "soft" grout with high water content, was limited to a small decrease in impedance compared to that of sound grout. Future testing is planned to determine whether presence of higher conductivity fluid (more representative of bleed water) has a more detectable effect. Sensitivity to inner voids (voids not extending to the inner wall of the polymer duct) was very limited at the operating frequency of 1 MHz.

Computer modeling showed that changing the plate configuration or using a guard plate method yielded modest increase in sensitivity or resolution compared to those obtained with a simple plate arrangement. Modeling also indicated that increasing operating frequency to much higher values (e.g., 500 MHz) had promising improvement in the ability to detect inner voids and other grout deficiencies. The projected improvement is based on the variation of grout impedance with frequency being different from that of the polymer duct. Operation at 500 MHz or similar high frequency should be explored in follow up investigations.

6. INTEGRATING MAGNETIC IMAGING AND IMPEDANCE SENSOR IN A TENDON IMAGING UNIT (TIU) LABORATORY PROTOTYPE

Introduction

In this chapter the outcomes of chapters 4 and 5 will be used to put together a joint strand positioning information/ grout assessment method concept where the two data are acquired together and processed simultaneously, resulting a tendon cross-section composite image revealing areas of deficiency. The outcome of this chapter will be a design of a prototype unit for sensing and of a data processing procedure/program to obtain a cross-section image.

Development of a Mark I Tendon Imaging Unit Laboratory Prototype (TIU-I)

Development of the laboratory prototype (TIU-I) coincided with the development of an initial unit under project FDOT number BDV25-977-52 [39]. The TIU-I includes the steel strand envelope location sensor and grout deficiency imaging sensor, suitable for laboratory operation of 3.5 nominal inch diameter tendons. Figure 6.1 shows the schematic/ block diagram for the initial prototype developed with collaboration of both projects. The TIU-I is self contained with the laptop and can operate freely without a need for an electrical outlet. All the components in the prototype are connected to a main controller (Arduino Mega 2560 board) which does the following:

1. Powers the signal generator (AD9850 board) which sends a 1 MHz signal for impedance measurements.

2. Powers the two magnetic sensors, and the gyroscope/accelerometer.

3. Transmits all the data from the components, the time, angular position, magnetic forces, and impedance measurements.

4. Sends the data back to the laptop which then analyzes the data via MATLAB code.
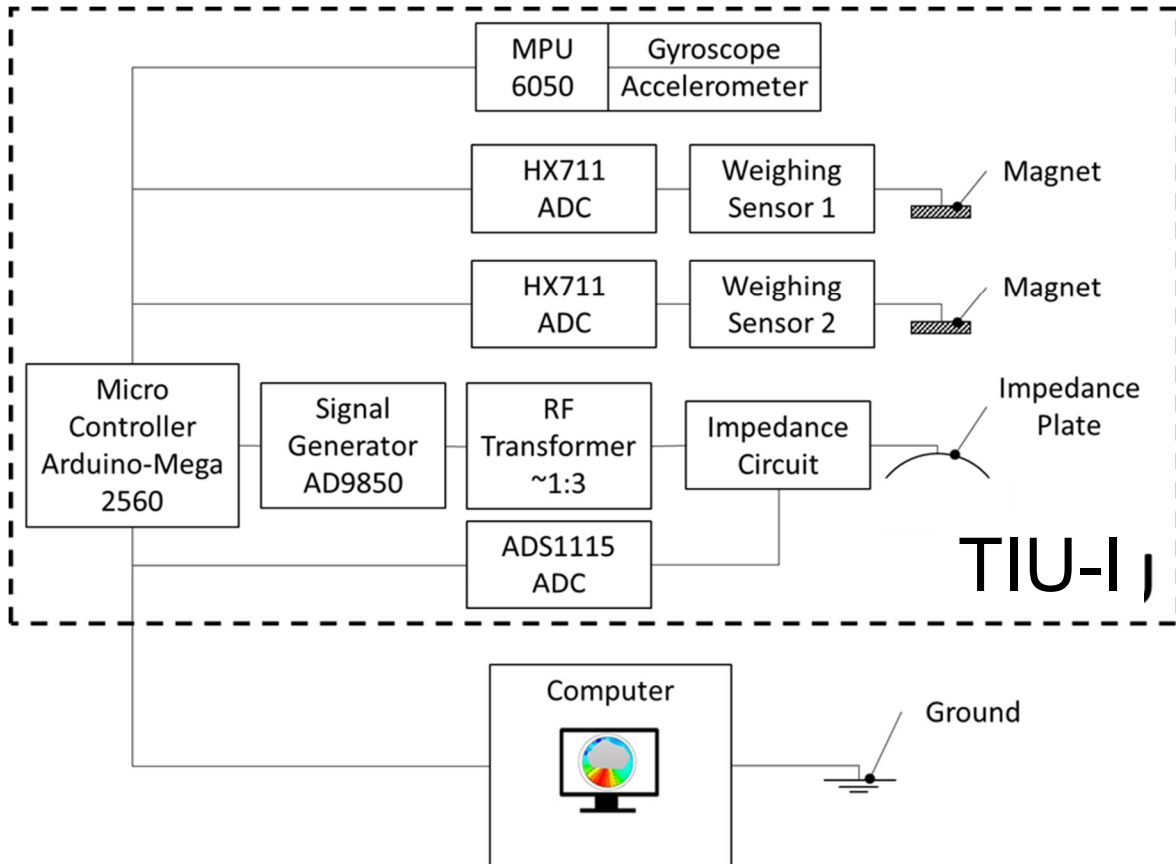
Figure 6.1 Block diagram schematic for the TIU-I laboratory prototype. Patent pending.

The following items are noted as well:

- The operational TIU-I was assembled consisting of a single capacitive high-frequency (1MHz) impedance module and two magnetic strand position detection modules (weighing sensors with magnet attached) assembled on a single 3D printed clamshell frame (Figure 6.2).

- The impedance module consists of a custom-built circuit board and an ADS1115 analog-digital converter.

- The magnetic strand position detection module consists of a HX711 circuit board wired to a micro load cells with a magnet attached to the free end of the load cell. There are two magnetic strand position detection modules present in the prototype (for this embodiment only one of the cells is used, but the two cells will be activated in follow-up development as discussed later).

- The use of 3D printing allowed for rapid prototyping of the clamshell frame during development. The clamshell frame (printed from a polylactide (PLA) thermoplastic filament) also contains the onboard Arduino Mega2650 microcontroller and various electronic circuit boards.

- The angular position of prototype is determined either absolutely with an accelerometer or with the use of a high-precision gyroscope; both are contained on a single MPU6050 circuit board. As a result, no riding wheel is needed for surface position tracking as used in previous version of the magnetic imaging method.

- The driving high frequency (1 MHz) potential source for the capacitive high-frequency impedance module is generated with a dedicated AD9850 signal generator circuit board amplified with a radio frequency transformer (~1:3).

- All the various electronic circuit boards communicate with a single microcontroller (Arduino Mega2650) that can be sent commands through the imaging computer wired or wirelessly (future development) by the operator.

- The outer perimeter of the entire TIU-I is contained within less than ~1.5 inch from the external HDPE duct perimeter.

- This low overburden was deemed to be suitable for the initial field tests of the collaborative project mentioned before, and it is expected to be reduced further as more compact electronic components are used in follow-up versions of the unit.
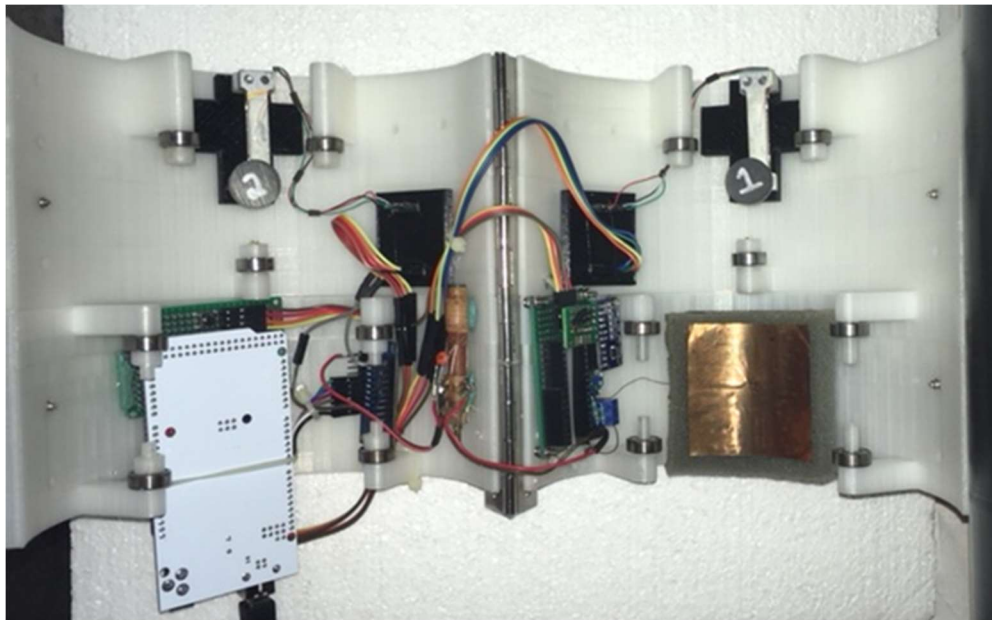
Figure 6.2 TIU-I with the clamshell opened to show internal components. Magnetic sensing load cells (numbered 1 and 2) are at the top. The capacitive sensor plate is at lower right. Roller bearings maintain precise positioning of the sensing elements on the external tendon duct surface. Electronic processing boards fit amply in the remaining gaps. Patent pending.

<u>Operation of The TIU-I laboratory prototype</u>.

The TIU-I was intended for obtaining cross-section images of the tendon at chosen locations along the tendon length, one at a time (Figure 6.3). The operation of obtaining an individual cross-section image is called an Image Acquisition (IA). Further details about interpreting the image will be discussed at the next section.
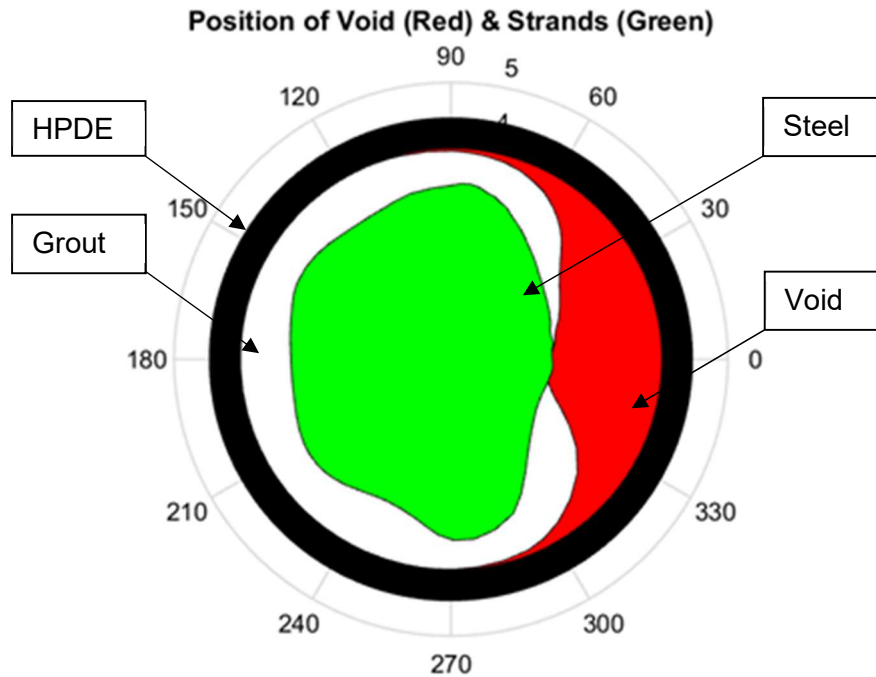
Figure 6.3 Image generated from the TIU-I after scanning an in-house cast tendon with the device centered on an existing void. Patent pending.

To operate the TIU-I, it must be connected with the imaging computer. It consists of a laptop with MATLAB ® and Arduino IDE software installed together with other files previously prepared as part of this project. Information on those files will have been previously customized by the investigators (research team) for the tendons to be tested, based on shop drawings for the bridge. Before the LP can be turned on, a zero-calibration is performed by first placing the unit in a reference condition (Figure 6.4), removed from the tendon to be evaluated and placed vertically on the ground at least 3.5 inch away from any steel mass. This is to be done at the beginning of a testing session each time the unit is powered on. With the unit on the ground operator launches the Arduino IDE installed on the imaging computer, connects computer to the unit (done via a single USB cable) and opens the Arduino Serial Monitor function. The USB connection powers the unit and a series of calibrations (magnetic and gyroscopic) occur automatically. The unit will track its progress and display several messages on the Serial Monitor to be read by the operator. After all the calibrations have been made, the unit will prompt the operator and wait for commands to be sent to start IA on a tendon (Figure 6.5).

Figure 6.4 TIU-I placed in the vertical calibration position away from steel mass. Patent Pending.

Figure 6.5 Screenshot of serial monitor after the TIU-I has calibrated and is ready to obtain an IA pending commands from the operator.

With the unit calibrated and awaiting commands from the operator, operator opens the clamshell, places the unit around the tendon (Figure 6.6), and secures the clamshell to fasten the unit onto the tendon (Figure 6.7). Elastic bands and a closure gap in the shell permit direct adaptation to deviations from ideal circular shape in the tendon cross-section. Once the unit is secured to the tendon, operator types the character "r", which starts, the IA through the serial monitor. When the IA starts a short delay occurs to allow the capacitive high-frequency impedance module to stabilize readings. The serial monitor will start to display data once the readings have stabilized. The operator then rotates the unit manually, in the direction indicated by an arrow on the exterior of TIU-I for at least one full rotation, slightly overshooting a full turn (e.g., a ~370 degrees rotation; the exact amount of overshooting is not critical). The operator then types the character "c" to end the IA and stop the acquisition of new data. The operator then rotates the TIU-I in reverse, back to the initial starting point to get it ready for the next IA. Future versions of the TIU-I can be readily improved to permit IA in both forward and backward directions, as well as only needing half-turn rotations, by use of enabled dual magnetic and impedance sensors. After the IA data has been saved, the unit can remain powered for the IA at the next selected tendon location. That location can be reached by sliding the TIU-I along the tendon or by opening the clamshell and reattaching it at the next selected location.
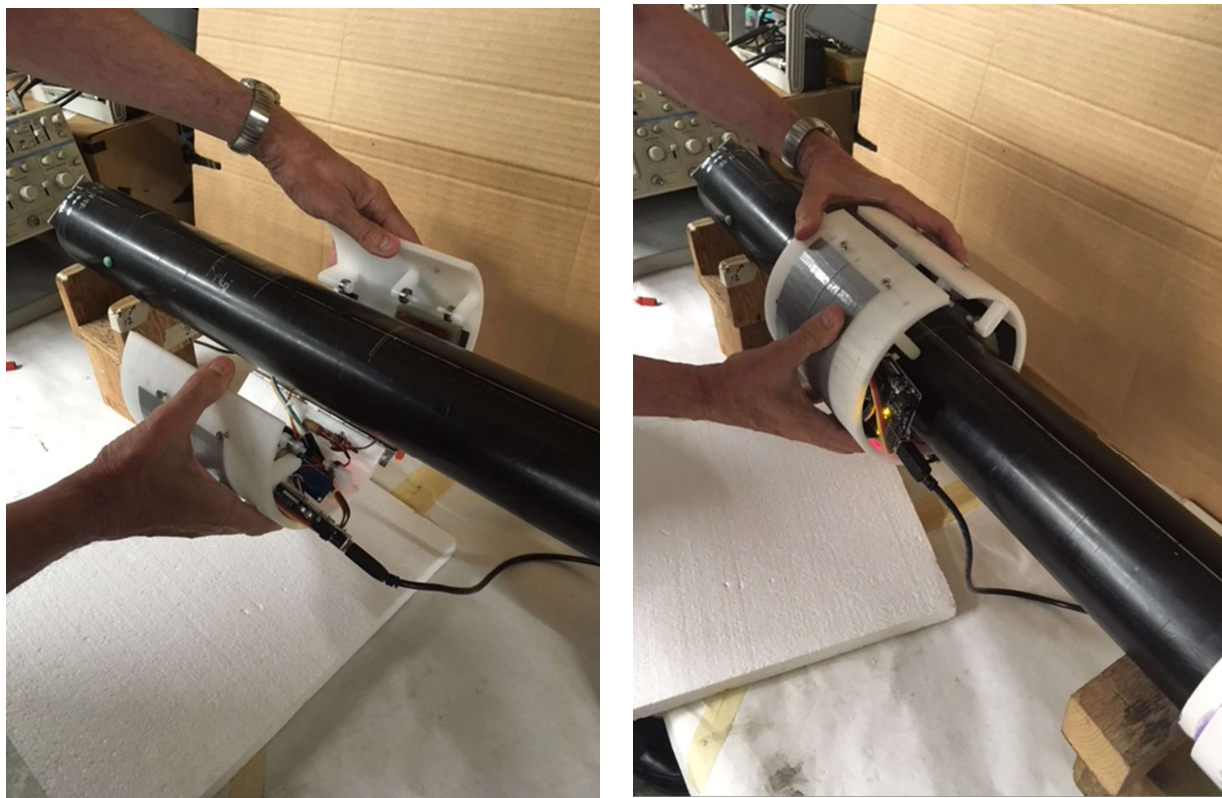
Figure 6.6 Placing the TIU-I around the tendon. Patent pending.
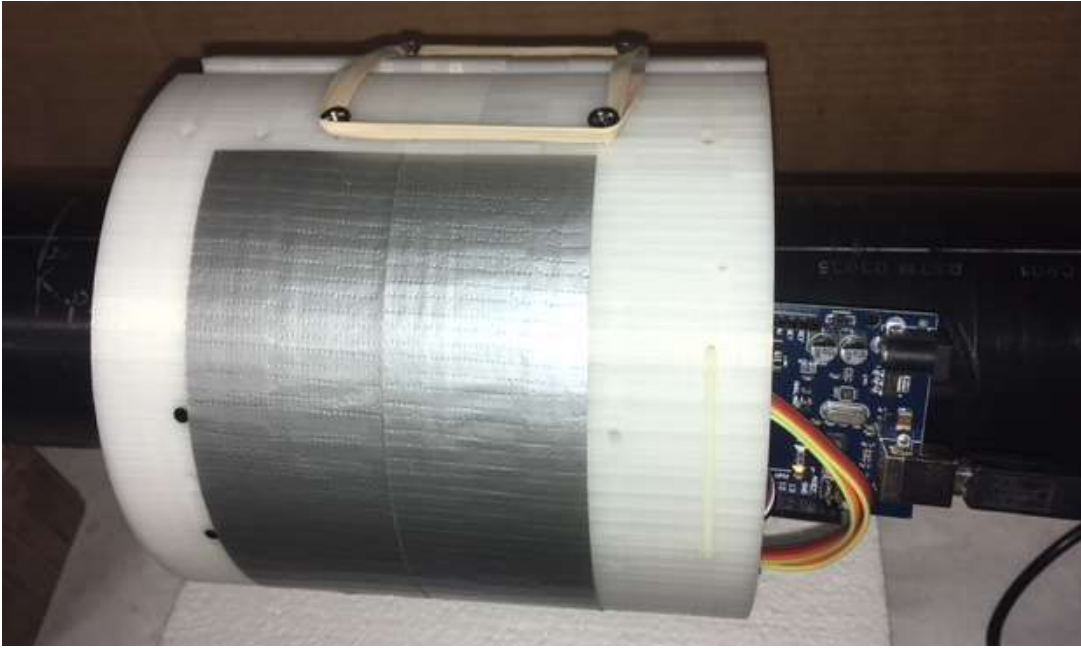
Figure 6.7 TIU-I secured to the tendon with elastic bands.

For the IA just completed, the data, displayed in the Serial Monitor, is copied and pasted by the operator into a "*.txt*" file that is stored in the same directory as the preinstalled MATLAB ® file "TendonImagingTool.m". That file has previously been edited by the research team with the parameters for the tendons being tested (i.e. Radius of Duct, Thickness of Duct, Thickness of Strand, etc.) listed in the "Define Variables" section of the .m file to ensure accurate imaging. Then the operator clicks "Run" in the MATLAB ® window to run the .m file and generate the image (Figure 6.8). The image is color coded as in Figure 6.3 and consists of an outer blue shell representing the HDPE duct material, a green area representing the steel strand envelope, a white area representing sound grout within the tendons cross-section, and a red area representing any void or grout anomaly than was found.
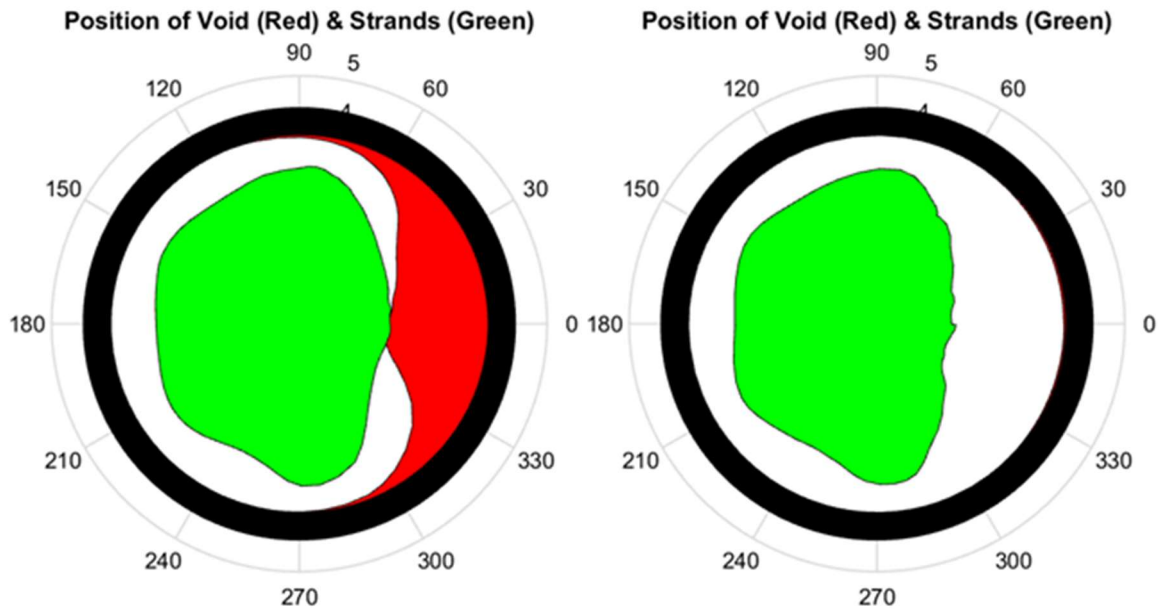
Figure 6.8 IAs generated from two different positions of the same piece of tendon. The left image was taken where a purpose-build void was cast into the tendon. The right image was taken where no void was cast. Patent pending.

The TIU-I was found to be able to detect the steel strand envelope of the tendons (3.5 nominal inch diameter) with a known cross-section cast in the lab as part of Deliverable 3 of this project. The TIU-I also differentiated as anticipated impedance measurements as the capacitive plate travels on top of the void filled with air located within the cross-section of the tendon segment.

Development of a Mark II, second laboratory prototype TIU-II).

As part of the collaborative work with Project BDV25-977-52, Field Demonstration of Tendon Imaging Methods, [39] an advanced version of the TIU (Mark II, TIU-II) was created and operated in the laboratory.

Figure 6.9 shows the TIU-II with the clamshell opened to show internal components. Magnetic sensing load cell is at the top left. The capacitive sensor plate is robust and flexible located to the right of the weighing sensor assembly. Roller bearings maintain precise positioning of the sensing elements on the external tendon duct surface. Electronic processing boards fit amply in the remaining space.
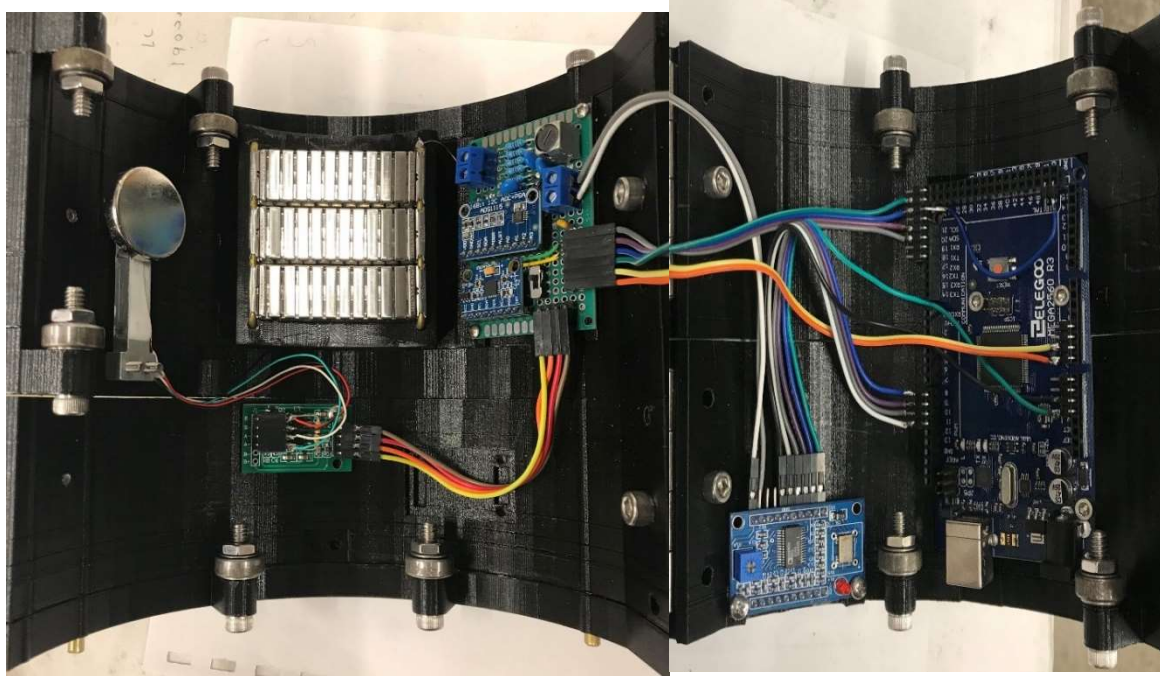
Figure 6.9 TIU-II with clamshell open to show internal components. Patent pending.

The TIU-II included the following new features:

- Redone 3D printed clamshell that allows testing of 4.5 nominal inch diameter tendons.

- New stronger Neodymium magnet for improved force/magnet weight ratio for more accurate compensation for magnet weight in tendons that are not in vertical alignment.

- A capacitive plate made of a more robust reliable material that is more tolerant to the irregular surface of the outer perimeter of the HDPE polymer

- Software includes compensation for magnetic properties of some grouts, which corrects for more accurate measurement of the steel strand envelope.

- The overburden around the duct diameter is < 1 inch as per design goals for minimum interference by nearby tendons or structural walls.

Based on its improved performance, the TIU-II was chosen to generate the images of the 4.5 nominal inch diameter tendon segments that were used for the gamma ray tomography validation tests described in chapter 7. The TIU-II was further improved as a Mark III, TIU-III version, called the Field Tendon Imaging Unit (FTIU). The FTIU is described in detail in the Final Report for FDOT Project Number: BDV25-977-52, Field Demonstration of Tendon Imaging Methods [39].

Figure 6.10 Top view of the TIU-II. Patent pending.

Chapter Summary.

Integration of the strand location magnetic method and the capacitive plate impedance measuring approach was successfully achieved in a practical unit suitable for field measurements under the scope of concurrent FDOT project BDV25-977-52, Field Demonstration of Tendon Imaging Methods [39].

7. LABORATORY PROTOTYPE VS. GAMMA RAY TOMOGRAPHY

Introduction

This chapter presents the comparison between the Tendon Imaging Unit - Mark II (TIU-II) prototype images and the results of Gamma Ray Tomography (GMT) imaging as part of the validations tests in this project. For this comparison 4 different tendon samples (referred to as ducts in the following) were cast in the Corrosion Laboratory at University of South Florida.

Physical Configuration

The tendon segments used had cross-section dimensions representative of those encountered in the field, with a 4.5 inch external diameter and 19 ½-inch 7 wire strands embedded in grout. The duct wall thickness in all cases was 7 mm. The segments were ~23 inches long with various steel strand and grout configurations. The detailed location of grout and steel strand assembly of each tendon segment ("Duct") are shown in Figure 7.1. The voids were created by embedding Styrofoam forms of the desired size and shape, filling the space to create the void. The foam was left in place except for the voids designed to be filled with water. For those locations the foam was first dissolved by injecting acetone in the space, which melted the foam and reduced its volume by > 95%, as determined by external tests in known volume containers. The solvent was then allowed to evaporate before resealing the solvent insertion hole. The grout used in these ducts was "EUCO Cable Grout PTX High Performance Cable Grout". Unless otherwise specified, the grout is cast in the "sound" (regular) grout manner, with a water-to-grout ratio of 0.25. All tests were performed in the lab after the grout had cured inside the sealed ducts at ambient temperature for a period of 105 days. For water-filled voids the water was injected in the void opening and allowed to sit in place for 2-4 minutes before scanning the place with the FTIU-II. The water was removed afterwards before shipping the ducts to the GRT laboratory. The GRT tests were conducted approximately 135 days after casting.

Duct A has a half moon steel arrangement (Figure 7.2) meaning the strands are bundled to one side of the tendon segment and has four different grout conditions (Figure 7.1). Measurements were performed on five different locations longitudinally named P1-P5 (Figure 7.3).

Duct B has a uniform steel strand arrangement (Figure 7.2) with two different air voids and two different water to grout ratios. The top grout is a "soft" grout with water-to-grout ratio of 0.375 (50% more water than the sound grout), and the bottom is "sound" grout. Measurements were performed on four different locations longitudinally named P1-P4 (Figure 7.3)

Ducts C and D have an asymmetrical steel strand assembly (Figure 7.2) with only one difference. Duct C has external voids, whereas Duct D has three internal voids (Figure 7.1). Measurements were performed on five different locations longitudinally for each duct named P1-P5 (Figure 7.3)
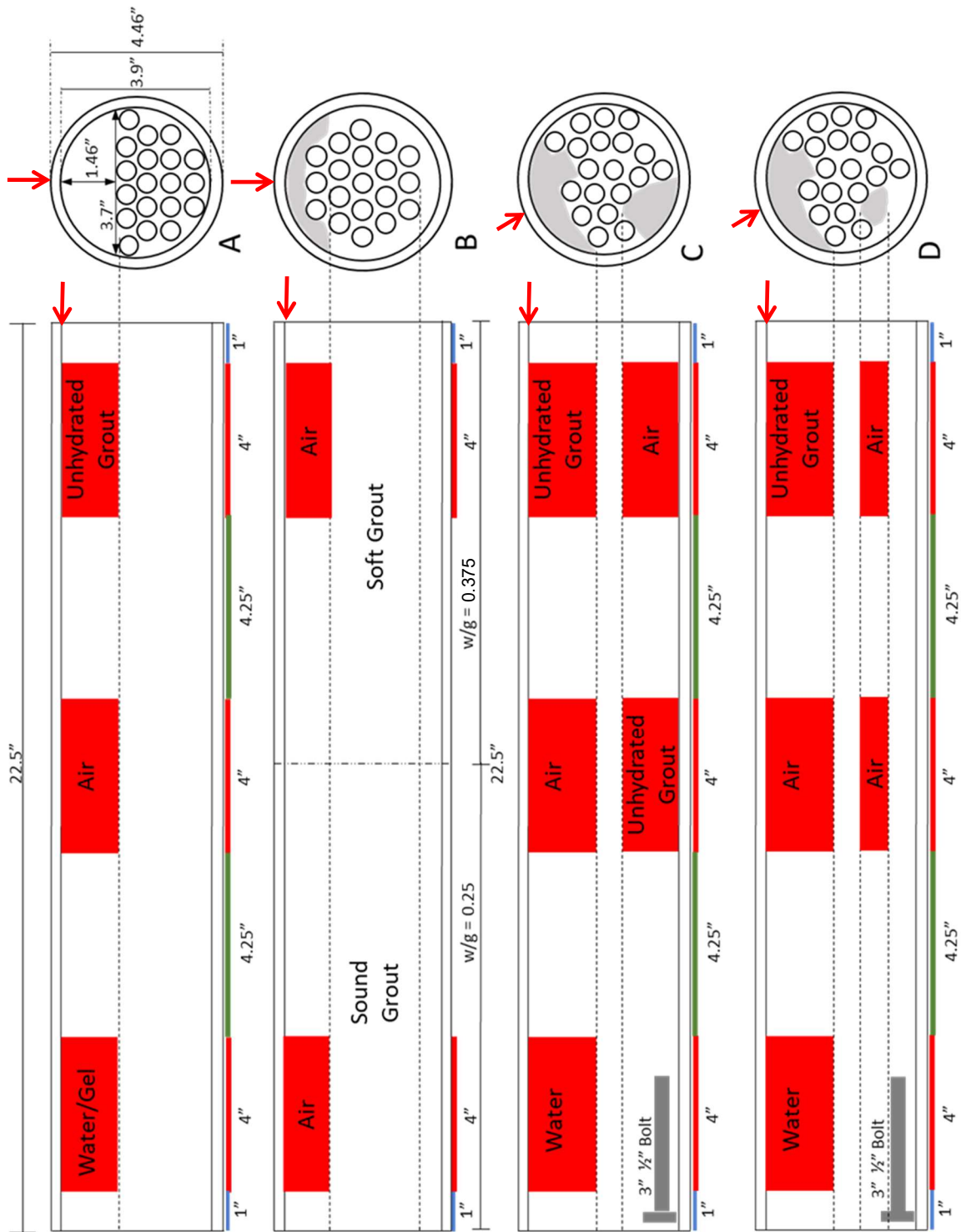
Figure 7.1 Approximate configuration for Ducts A-D.
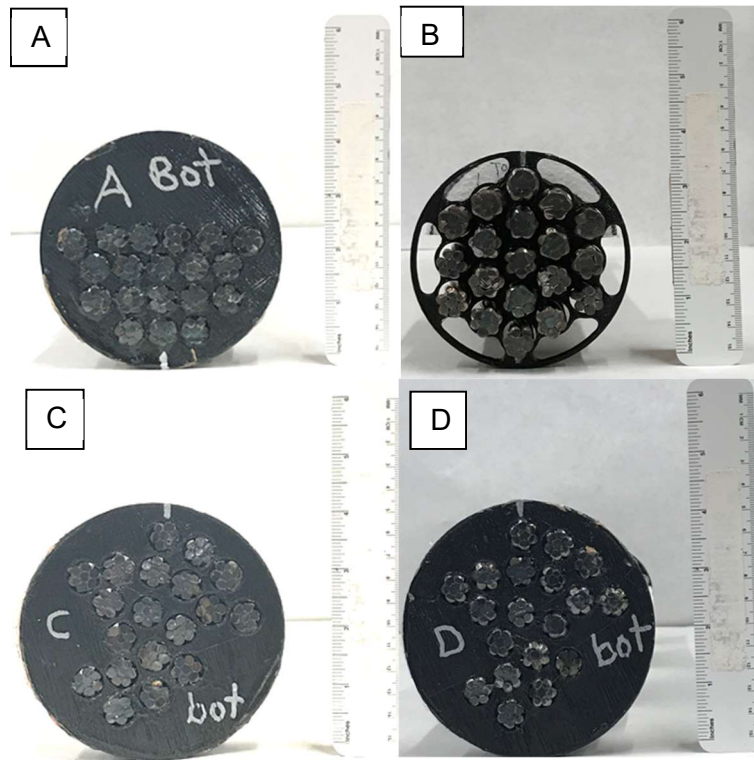
Figure 7.2 End cross-section of steel strand assembly for each Duct A-D cast.

Figure 7.3 Side view of ducts A-D showing the locations of P1-P5 (different grout configurations). Arrows are keyed to positions shown in Figure 7.1

Results of the TIU-II imaging.

The cross-sectional images for Ducts A-D are shown below at the locations described earlier P1-P5. These measurements were taken by the TIU-II described in chapter 6. In each image the display has been oriented so that the red arrow matches the arrow positions in Figure 7.1
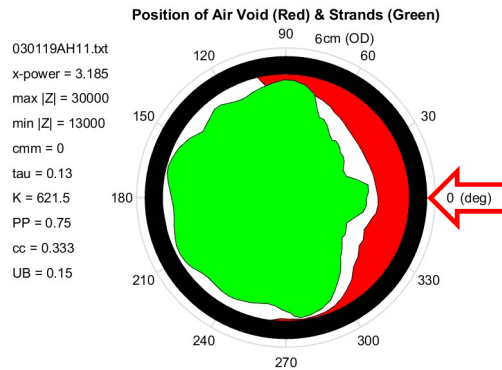
Figure 7.4 Cross-sectional image of P1-unhydrated grout in Duct A.
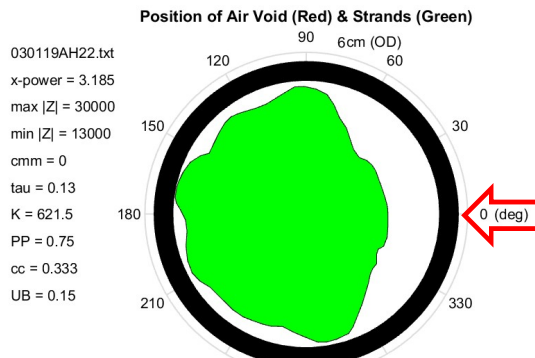
Figure 7.5 Cross-sectional image of P2-sound grout in Duct A
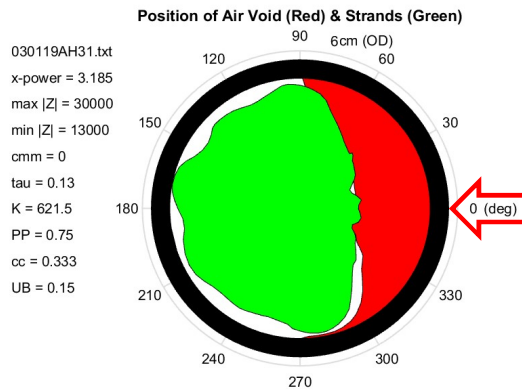
Figure 7.6 Cross-sectional image of P3-air void in Duct A.

79
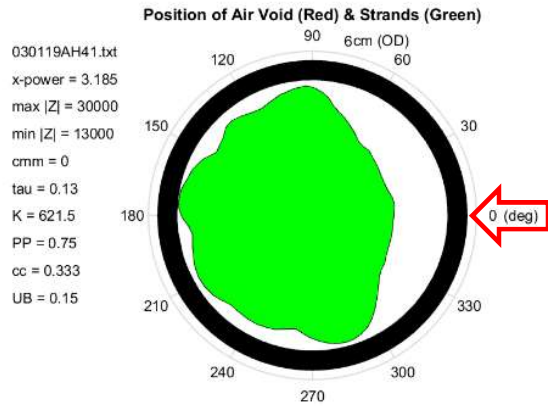
Figure 7.7 Cross-sectional image of P4-sound grout in Duct A.
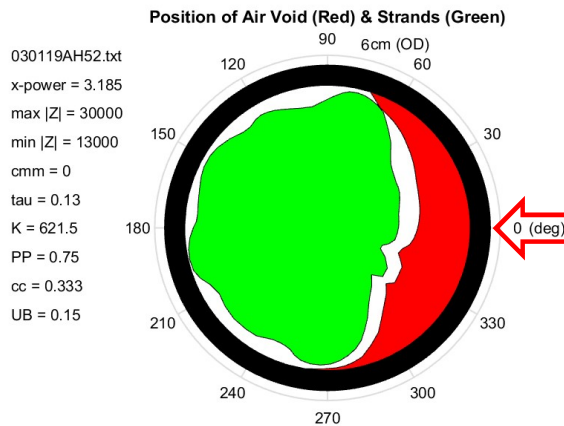
Figure 7.8 Cross-sectional image of P5-air void (before adding water) in Duct A.
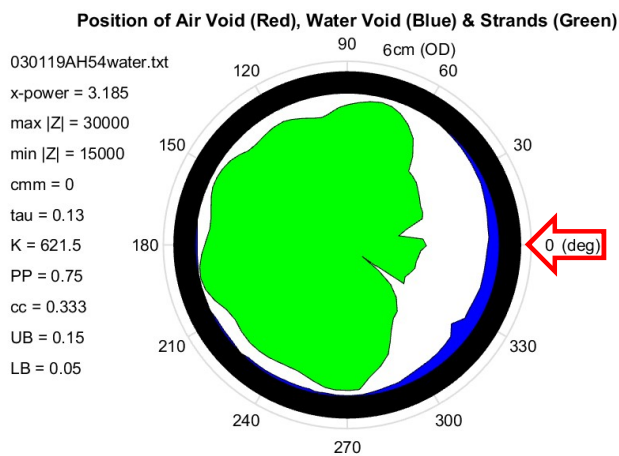
Figure 7.9 Cross-sectional image of P5-water void (after adding water) in Duct A.

Note: The cross-sectional images of P5 (and P4 in Duct B) are flipped across the horizontal axis since the TIU-II had to be inverted to perform the measurements at these locations since the capacitor plate is at the top of machine.

Position of Air Void (Red) & Strands (Green)

030119BH12.txt
x-power = 3.185
max |Z| = 30000
min |Z| = 13000
cmm = 0
tau = 0.13
K = 621.5
PP = 0.75
cc = 0.333
UB = 0.15
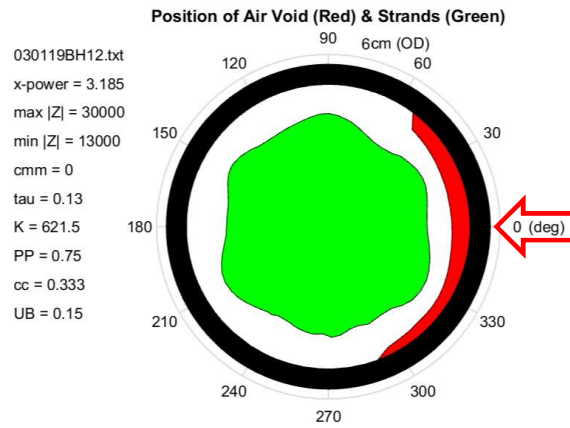
Figure 7.10 Cross-sectional image of P1-air void in Duct B.

Position of Air Void (Red) & Strands (Green)

030119BH22.txt
x-power = 3.185
max |Z| = 30000
min |Z| = 13000
cmm = 0
tau = 0.13
K = 621.5
PP = 0.75
cc = 0.333
UB = 0.15
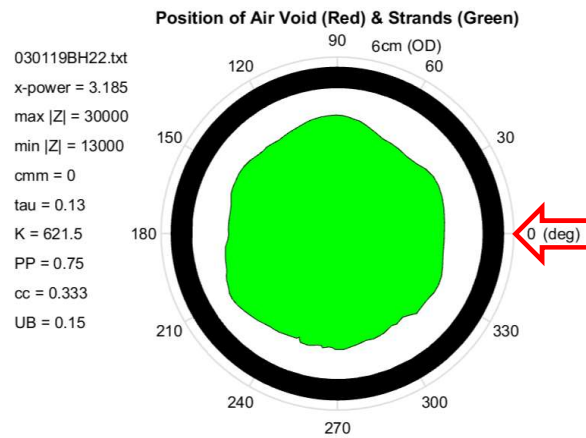
Figure 7.11 Cross-sectional image of P2-soft grout in Duct B.

Position of Air Void (Red) & Strands (Green)

030119BH32.txt
x-power = 3.185
max |Z| = 30000
min |Z| = 13000
cmm = 0
tau = 0.13
K = 621.5
PP = 0.75
cc = 0.333
UB = 0.15
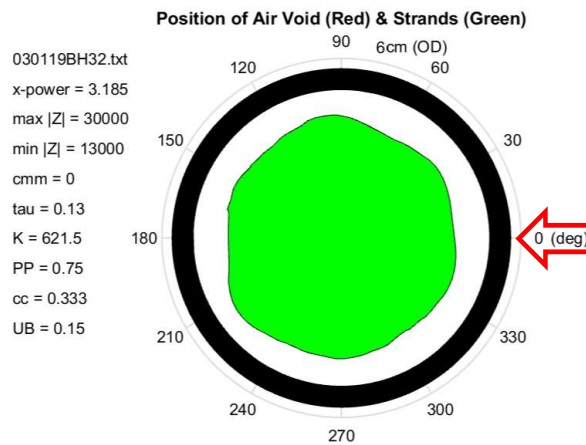
Figure 7.12 Cross-sectional image of P3-sound grout in Duct B.

81
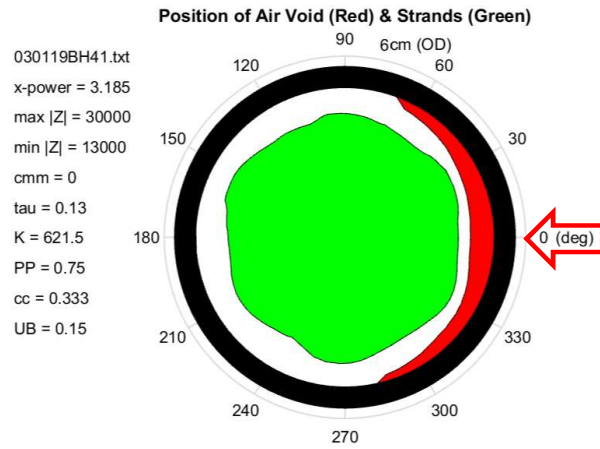
Figure 7.13 Cross-sectional image of P4-air void in Duct B.
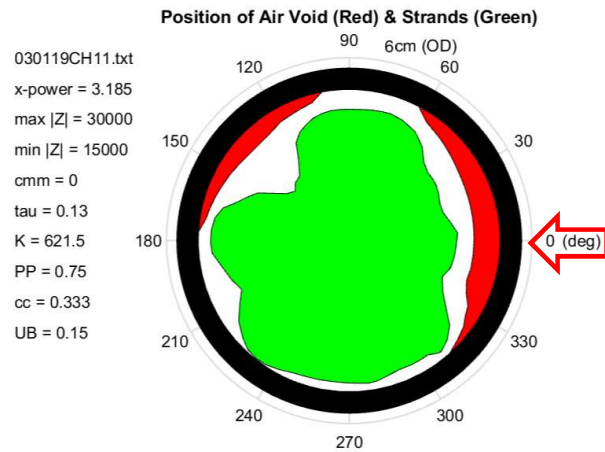
Figure 7.14 C ross-sectional image of P1-unhydrated grout in Duct C.
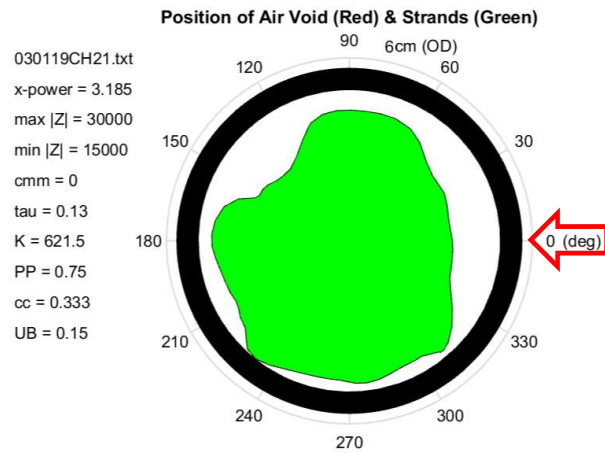
Figure 7.15 Cross-sectional image of P2-sound grout in Duct C.
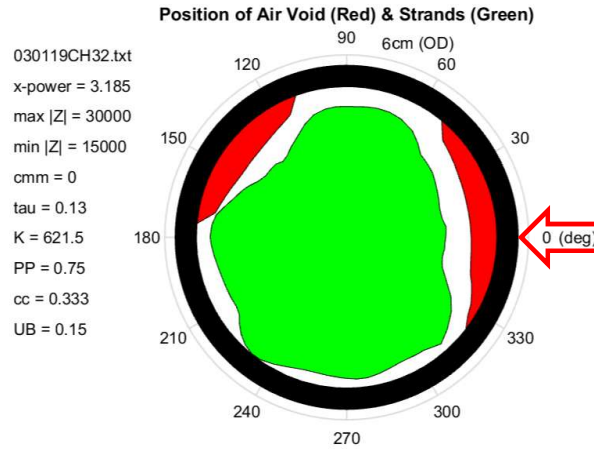
Figure 7.16 Cross-sectional image of P3-air void in Duct C.
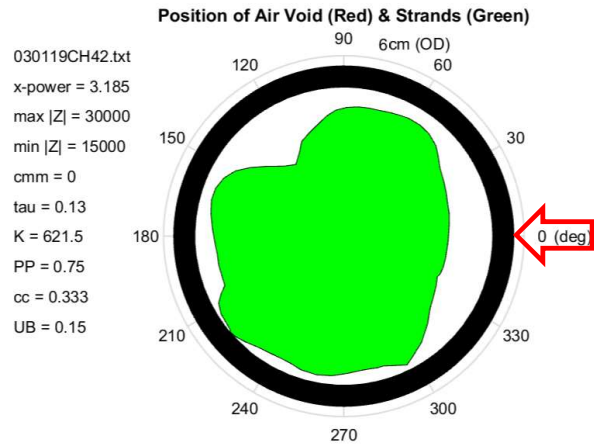
Figure 7.17 Cross-sectional image of P4-sound grout in Duct C.
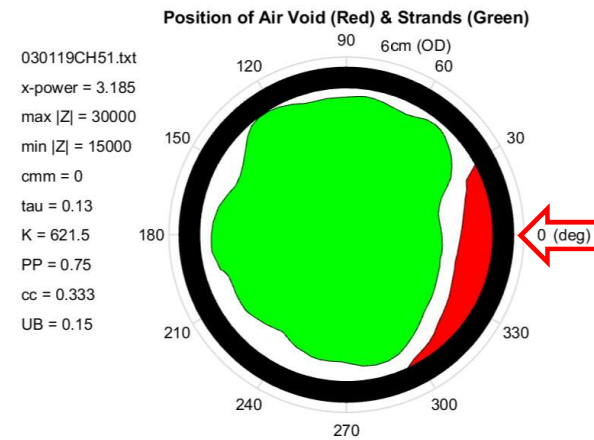
Figure 7.18 Cross-sectional image of P5-air void (before adding water) in Duct C. The TIU-II captured the 3"-long ½" bolt.
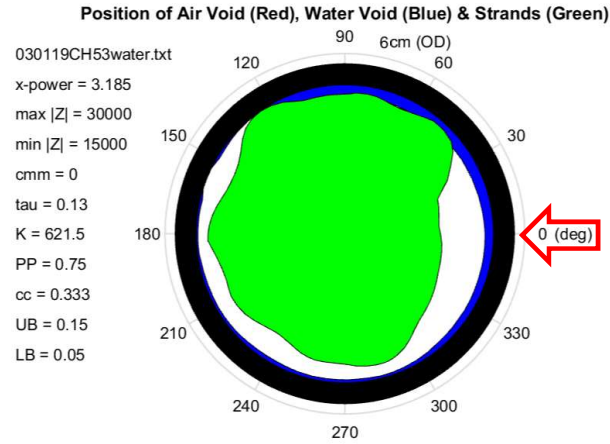
Figure 7.19 Cross-sectional image of P5-water void (after adding water) in Duct C. The TIU-II captured the 3"-long ½" bolt.
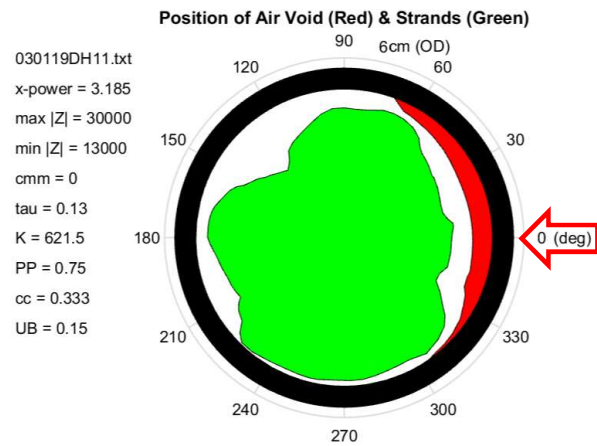
Figure 7.20 Cross-sectional image of P1-unhydrated grout in Duct D. The TIU-II did not capture the internal void.
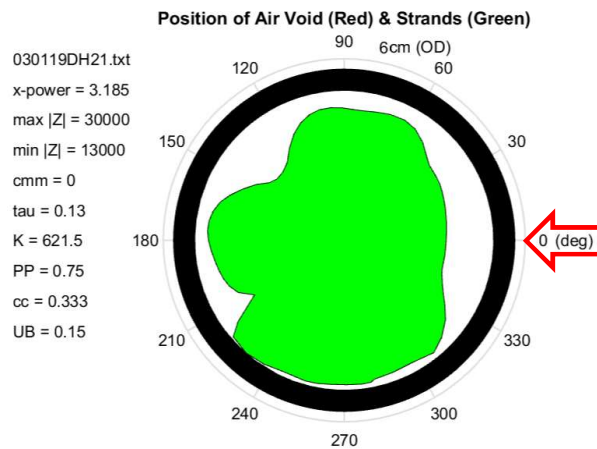
Figure 7.21 Cross-sectional image of P2-sound grout in Duct D.
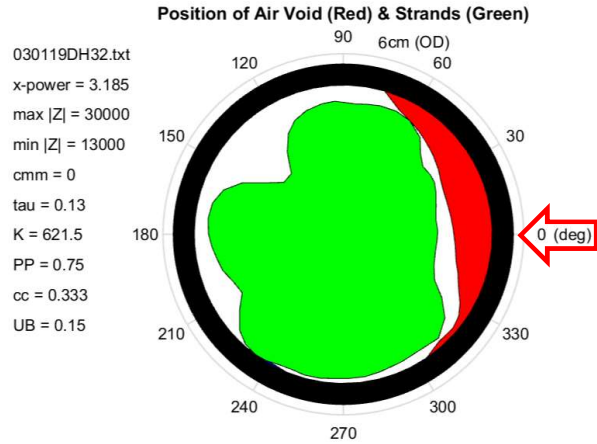
Figure 7.22 Cross-sectional image of P3-air void in Duct D.
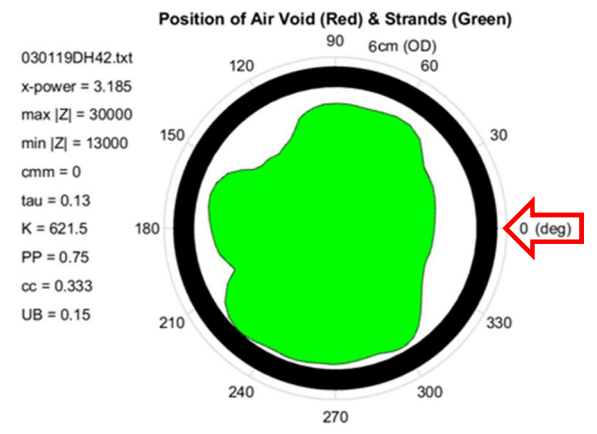
Figure 7.23 Cross-sectional image of P4-sound grout in Duct D.
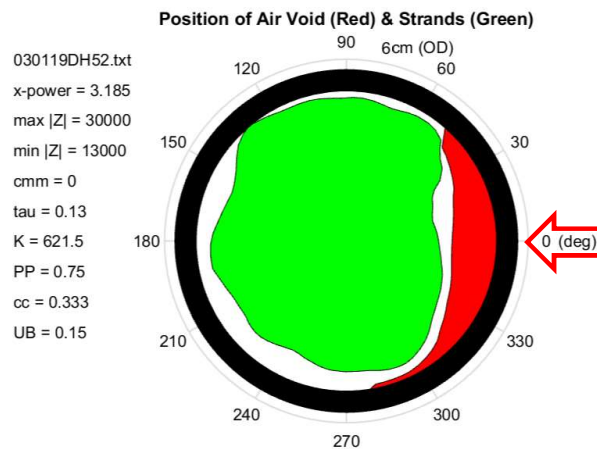
Figure 7.24 Cross-sectional image of P5-air void (before adding water) in Duct D.
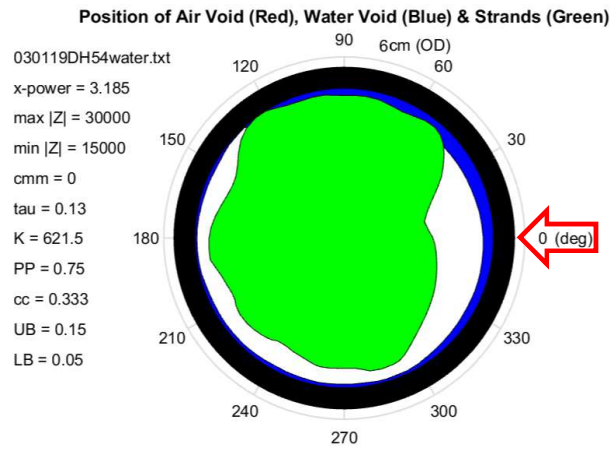
Figure 7.25 Cross-sectional image of P5-air void (after adding water) in Duct D.

GRT/TIU-II Results Comparison and Discussion

The company THASA S.A. was subcontracted to conduct the GRT tests. Detailed description of the methodology and test results is presented in Appendix C, that includes the main set of results and an addendum with further information. Reference is made to that material with some summary observations made below.

Pictorial excerpts of corresponding images obtained with the TIU-II and the GRT reconstruction of the same selected cross-sections are shown side by side in Figure 7.26. This figure, with minor modifications, is equivalent to that shown in the Addendum in Appendix C. The red arrows indicate the same angular positions as the red arrows in Figures 7.4-7.25, with the figures rotated accordingly to match the orientation of the design drawings and GRT results.

Row "A" corresponds to section P3 (air void) imaged in Figure 7.6 of Duct A. For this duct the GRT system was able to identify positions of individual strands, which agree quite closely with the design drawing and the strand envelope section reported by the TIU-II. The GRT also identified an entire portion of the cross-section with very low (0.2 g/cm^3) density, in agreement with the presence of the Styrofoam-filled void at that location, and consistent as well with the void flagging provided for the same region by the TIU-II. The rest of the cross-section was associated with normal grout by the GRT (indicating a density of 1.8 g/cm^3, consistent with that of sound grout) and by the TIU-II, both with corresponding white color coding.

Row "B" corresponds to section P4 imaged in Figure 7.13 for Duct B. In this and the other ducts C and D, GRT identified only the outline of the strand bundle. Otherwise GRT correctly identified a near-zero density region for the narrow void present there, and sound grout elsewhere. TIU-II identified the same strand and grout regions as well, with clear but somewhat reduced flagging of the narrow void region. Neither GRT nor TIU-II provided clear differentiation between soft (higher water-to-grout ratio) and normal grout

Row "C Top" pertains to sections P1 for Duct C. The larger of the two voids there is filled with unhydrated grout, while the smaller void contains only Styrofoam. GRT identified an irregular strand pattern and provided clear differentiation between both voids, and in the expected direction (density near 1 g/cm^3 in the unhydrated case, consistent with direct measurements of volume- averaged unhydrated grout density of ~1.08 g/cm^3. TIU-II (from Figure 7.14) revealed the main features of the irregular strand pattern, consistent with the GRT indications. TIU-II also identified the presence of both voids but did not provide clear differentiation, other than indicating lesser signals than in the case of full voids.

P3 – 11,6"

P4 – 20"

P1 – 4.6"

P5 – 18.1"

P3 – 10.8"

🟩 strand	⚫ bolt	🟥 density 0 g/cm³	🟧 density 1-1.1 g/cm³
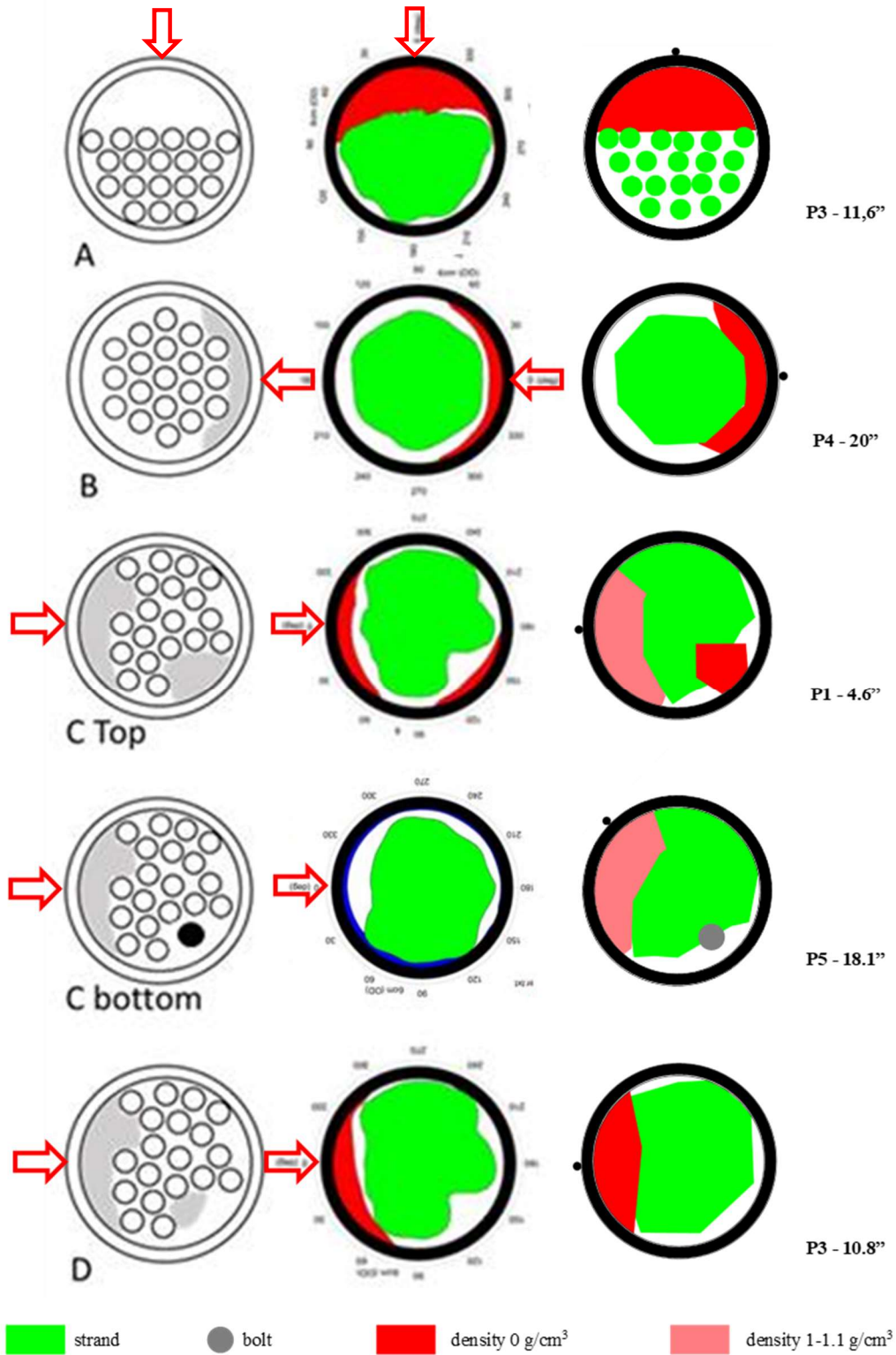
Figure 7.26 Comparison of selected cross-sections per design (left) obtained with the Laboratory Prototype (center) and GRT (right). Arrows indicate orientation per Figures 7.4-7.25. Adapted from information in Appendix C.

88

Row "C bottom" pertains to section P5 for Duct C. The void is full of water and a ½ inch diameter steel bolt is present as well. GRT identified the presence of the bolt, and correctly identified as well a region the size of the larger void, as being filled with a medium of density ~1 g/cm^3 - thus consistent with the presence of water. The presence of the smaller void where the bolt was located was not clearly flagged, however. The TIU-II (from Figure 7.19) showed a fuller strand profile than in P1, consistent with a source of additional magnetic attraction in the region where the bolt had been placed. However, the TIU-II showed only a weak indication of the presence of the water, best seen in the higher magnification display in Figure 7.19. The water acted as a medium of low impedance, but of little contrast with the similarly low impedance grout on the rest of the cross-section, thus not clearly flagging an abnormality in that region. It is noted that the TIU-II did clearly sense the filling of the void with water: Figure 7.18 shows the image before water filling with the full void conspicuously flagged, that no longer being the case in Figure 7.18 after filling; the limitation is the low differentiation between sound grout and water.

Row "D" concerns the central void in section P3 of Duct D. This region contained an irregular strand pattern with a large void on one side and an inner void elsewhere. GRT provided relatively low resolution imaging of the strand bundle, and identified correctly the large void. However, no clear flagging of the small void was produced. The TIU-II provided a more resolved image of the strand pattern than the GRT, identified the presence of the large void, but did not flag the presence of the smaller inner void.

The above comparison and rest of the information obtained with both imaging techniques provide a significant extent of validation of the TIU-II instrument application, and by extension of the relevance of the combined use of strand position and impedance measurements for detection of grouting deficiencies. While TIU cannot match the single-strand resolution to which GRT is capable with dedicated processing, TIU provided viable and reliable strand envelope information, usually comparable to that provided by GRT in its normal resolution. Concerning grout deficiencies, the TIU method in its present form is best at detecting voids that extend to the inner surface of the polymeric duct. For that application it has shown, at a much lower cost and simplicity, results comparable to those obtained via GRT. TIU could detect the presence of unhydrated grout fill in an otherwise full void, as did GRT. However, TIU provided only a limited indication of irregularity in a water filled void, while GRT indicated the presence of a fill with the density of water. GRT nevertheless is sensitive only to mass density so it could not discern between water and unhydrated grout, both of which have densities near 1 g/cm^3. It is noted also that the TIU method provides nearly instantaneous imaging with minimum operator requirements, while GRT in its present form of a custom service requires multiple exposures (some as long as 18 seconds) and customized post-processing by a specialist.

Concerning the use of GRT as a calibration means for TIU field operations, joint deployment for that purpose may be an attractive option under some circumstances. A likely scenario would be application in case of a large bridge with a large number of replicate external tendons (e.g., hundreds or even thousands), where there could be known instances of deficient grout tendons. Those instances could serve as a one or more calibration points for the TIU system at the start of a bridge-wide survey, providing high value information with the cost of short-time GRT application distributed as a small overburden over a large number of tests. It is noted that in project BDV25-977-52, Field Demonstration of Tendon Imaging Methods, a calibration procedure has been incorporated in the field unit operation to take advantage of knowledge of the presence of known deficiencies (or of known sound grout condition) at specific tendon places, so as to use the impedance signature at those locations to set the limits for color flagging of voids or other deficiencies.

Chapter Summary

Tendon cross-section imagen information obtained with the tendon imaging unit (TIU) and gamma ray tomography (GRT) provided a significant extent of validation of the TIU instrument application, and by extension of the relevance of the combined use of strand position and impedance measurements for detection of grouting deficiencies. While TIU cannot match the single-strand resolution to which GRT is capable with dedicated processing, TIU provided viable and reliable strand envelope information, usually comparable to that provided by GRT in its normal resolution.

The TIU method in its present form is best at detecting voids that extend to the inner surface of the polymeric duct, providing comparable results to those of GRT. Sensitivity was more limited for smaller voids or voids filled with unhydrated grout. Neither TIU nor GRT adequately sensed a small inner void. TIU provided only a limited indication of irregularity in a water filled void, while GRT indicated the presence of a fill with the density of water. GRT nevertheless is sensitive only to mass density so it could not discern between water and unhydrated grout, both of which have densities near 1 g/cm^3.

The TIU method provides nearly instantaneous imaging with minimum operator requirements, while GRT in its present form of a custom service requires multiple exposures and customized post-processing by a specialist. GRT calibration of a TIU may be desirable in cases that include large tendon inventories.

8. ACHIEVEMENTS AND CONCLUSIONS

1. An integrated imaging procedure concept for external tendons was created, consisting of a magnetic strand position imaging base and a simultaneous impedance assessment of condition of the grout in the space between the strand and the inner tendon duct perimeter.

2. The strand position imaging concept was demonstrated with a prototype that was successfully designed, constructed, and operated. The unit features movable magnetic sensors that quickly obtain reproducible records of acting force as function of angular position in a manner suitable for imaging processing.

3. Two consecutive deconvolution procedures for strand position detection were developed and successfully implemented. The first procedure took the sensor response as function of time and corrected for time response delay using a Fourier transform approach, yielding recovery of the force corresponding to a given sensor angular position that would have taken place under nearly static conditions.

4. The second deconvolution procedure for strand position detection converted the force readings into radial distance between the external duct surface and the strand bundle envelope, using a power law approximation of the magnet force - strand distance relationship. The power law approximation was abstracted from finite element simulations of a simplified version of the system, and from the behavior of idealized magnet / ferromagnetic medium systems.

5. Application of the deconvolution procedures resulted in recovery of the strand bundle envelope that was validated against the known configuration of the tendon test segments evaluated with the method produced here. The recovery is reproducible and accurate to the extent that integration with grout condition assessment was deemed practicable.

6. An alternative exploratory strand position imaging method was implemented using standard rebar location equipment. Initial tests produced encouraging results in the form of semi-quantitative information of strand position and arrangement. This method is promising for future development of systems with fewer moving parts.

7. Review of the literature confirmed that electromagnetic wave evaluations that sample the dielectric and ionic admittance/impedance of the duct-strand space held the most promise for successful implementation of the integrated imaging sensor concept.

8. In combination with the magnetic strand position information, impedance measurements reported as a function of rotational angle from a start place clearly identified the presence of voids fully extending from the inner wall of the duct to the strand envelope ("full voids"). The full-void region was manifested by impedance values that were typically two or more times higher than those of regions of sound grout.

9. Integration of strand position and impedance information was processed to produce an image of the tendon cross-section that distinctly flags the presence of the full void and provides immediate visual differentiation between sound and deficient grout locations.

10. Voids extending from the inner surface of the duct to 2 mm or more inward, followed by sound grout, produced a signature pattern comparable to that of full voids.

11. Voids in the grout between the inner surface of the duct and the strand envelope, but including a grout layer immediately next to the inner surface of the duct ("inner voids") produced a signature pattern intermediate between that of full voids and sound grout.

12. Portions of un-hydrated grout fully extending between the inner surface of the duct and the strand envelope produced a signature pattern intermediate between that of full voids and sound grout.

13. Full voids filled with water (analogous to high water content "soft grout" resulted in impedance values somewhat lower than those observed with sound grout. The resulting modest differentiation was usable to flag that condition with proper independent calibration.

14. Computer modeling was implemented to predict the tendon response to impedance measurement excitation via the external sensor at changing angular positions. The model used grout parameters accurately reproducing experimental measurements for both sound condition and void filled with air. Different frequencies and plate configurations were explored and assessed. Operation at 500 MHz shows promise for better grout deficiency detection.

15. A laboratory prototype was successfully implemented, with collaboration from project BDV25-977-52, Field Demonstration of Tendon Imaging Methods, to produce a graphical color-coded image that displayed grout anomalies on a tendon's cross-section, based on the patterns of differentiation obtained experimentally and with the computer simulations.

16. Tendon cross-section imagen information obtained with the tendon imaging unit (TIU) and gamma ray tomography (GRT) provided a significant extent of validation of the TIU instrument application, and by extension of the relevance of the combined use of strand position and impedance measurements for detection of grouting deficiencies.

17. While TIU cannot match the single-strand resolution to which GRT is capable with dedicated processing, TIU provided viable and reliable strand envelope information, usually comparable to that provided by GRT in its normal resolution.

18. The TIU method in its present form is best at detecting voids that extend to the inner surface of the polymeric duct, providing comparable results to those of GRT. Sensitivity was more limited for smaller voids or voids filled with unhydrated grout.

19. Neither TIU nor GRT adequately sensed a small inner void. TIU provided only a limited indication of irregularity in a water filled void, while GRT indicated the presence of a fill with the density of water. GRT nevertheless is sensitive only to mass density so it could not discern between water and unhydrated grout, both of which have densities near 1 g/cm^3.

20. The TIU method provides nearly instantaneous imaging with minimum operator requirements, while GRT in its present form of a custom service requires multiple exposures and customized post-processing by a specialist. GRT calibration of a TIU may be desirable in cases that include large tendon inventories.

REFERENCES

[1] K.K. Krishna Vigneshwaran, S. Permeh, M. Echeverría, K. Lau, I. Lasa, "Corrosion of Post-Tensioned Tendons with Deficient Grout, Part 1: Electrochemical Behavior of Steel in Alkaline Sulfate Solutions", CORROSION, Vol. 74, No. 3 p.362-371, 2018.

[2] S. Permeh, K.K. Krishna Vigneshwaran, M. Echeverría, K. Lau, I. Lasa, "Corrosion of Post-Tensioned Tendons with Deficient Grout, Part 2: Segregated Grout with Elevated Sulfate Content", CORROSION, Vol. 74 No. 4, p. 457-467, 2018.

[3] S. Permeh, K.K. Krishna Vigneshwaran, K. Lau, I. Lasa, "Corrosion of Post-Tensioned Tendons with Deficient Grout, Part 3: Segregated Grout with Elevated Sulfate and Vestigial Chloride Content", CORROSION, Vol. 75, No. 7, p. 848-864, 2019.

[4] A. Azizinamini and J. Gull, "Improved Inspection Techniques for Steel Prestressing/Post-Tensioning Strands", Vol. I. Final Report to Florida Department of Transportation, Project BDK80 977-13, p 111, June 2012.

[5] A. Azizinamini and J. Gull, "FDOT Protocol for Condition Assessment of Steel Strands in Post-Tensioned Segmental Concrete Bridges", Vol. II. Final Report to Florida Department of Transportation, Project BDK80 977-13, p. 25, June 2012.

[6] S. Im, S. Hurlebaus, and D. Trejo, "Inspection of Voids in External Tendons of Posttensioned Bridges", Transportation Research Record, Vol. 2172, p. 115-122, 2010.

[7] S. Im, and S. Hurlebaus, "Non-Destructive Testing Methods to Identify Voids in External Post-Tensioned Tendon", KSCE Journal of Civil Engineering, Vol. 16, p. 388-397, 2012.

[8] S. Iyer, A.J. Schokker, and S. K. Sinha, "Ultrasonic Imaging – A Novel Way to Investigate Corrosion Status in Post-Tensioned Concrete Members", J. Indian Inst. Sci., Vol. 82, p. 197-217, December 2002.

[9] Corven Engineering, Inc., "Mid-Bay Bridge Post-Tensioning Evaluation", report submitted to Florida Department of Transportation, Tallahassee, FL, October 10, 2001.

[10] B. Fernandes, M. Titus, D. K. Nims, A. Ghorbanpoor, and V. Devabhaktuni, "Field Test of Magnetic Methods for Corrosion Detection in Prestressing Strands in Adjacent Box-Beam Bridges", ASCE Journal of Bridge Engineering, Vol. 17, No. 6, p. 984-988, 2012.

[11] F.J. Presuel-Moreno, A.A. Sagüés, "Bulk Magnetic Susceptibility Measurements for Determination of Fly Ash Presence in Concrete", Cement and Concrete Research, Vol. 39, p. 95-101, 2009.

[12] A. A. Sagüés, S.C. Kranc, and T.G. Eason, "Vibrational Tension Measurement of External Tendons in Segmental Post-Tensioned Bridges", ASCE Journal of Bridge Engineering, Vol. 11, No.5, p.582, 2006.

[13] A. A. Sagüés, T. Eason, C. Cotrim, J. Lopez-Sabando, "Validation and Practical Procedure for Vibrational Evaluation of Tendons", Final Report to Florida Department of Transportation,

Report No. BC353-44, 188 pp., March 31, 2008.

[14] W. Liu, R. Hunsperger, M. Chajes, and E. Kunz, "An Overview of Corrosion Damage Detection in Steel Bridge Strands Using TDR", Proc. of the 2nd International Symposium on TDR for Innovative Applications, Evanston, Illinois, 2001.

[15] M. Krause, B. Milmann, F. Mielentz, D. Streicher, B. Redmer, K. Mayer, K. J. Langenberg, and M. Schickert, "Ultrasonic Imaging Methods for Investigation of Post-tensioned Concrete Structures: A Study of Interfaces at Artificial Grouting Faults and Its Verification", Journal of Nondestructive Evaluation, Vol. 27, Issue 1, p. 67-82, September 2008.

[16] B. Milovanovic, and I. B. Pecur, "Review of Active IR Thermography for Detection and Characterization of Defects in Reinforced Concrete", Journal of Imaging, Vol 2, Issue 2, p. 27 April 2016.

[17] D. G. Pollock, K. J. Dupuis, B. Lacour, and K. R. Olsen, "Detection of Voids in Prestressed Concrete Bridges Using Thermal Imaging and Ground-Penetrating Radar", WSDOT report No. WA-RD 717.1, Pullman, WA, December 2008.

[18] M. Cabeza, M. Keddam, X.R. Novoa, I. Sanchez, and H. Takenouti, "Impedance Spectroscopy to Characterize the Pore Structure During the Hardening Process of Portland Cement Paste", Electrochimica Acta, Vol. 51, p. 1831-1841, January 2006.

[19] S.J. Ford, T.O. Mason, B.J. Christensen, R.T. Coverdale, and H. M. Jennings. Electrode Configurations and Impedance Spectra of Cement Pastes. Journal of Materials Science. Vol. 30. P 1217-1224, 1995.

[20] M. Hallaji, A. Seppanen, and M. Pour-Ghaz, "Electrical Impedance Tomography-Based Sensing Skin for Quantitative Imaging of Damage in Concrete", IOP Publishing, Smart Materials and Structures, Vol. 23, No. 8, 2014.

[21] B. Elsener, and M. Buchler, "Quality Control and Monitoring of Electricity Isolated Post-tensioning Tendons in Bridges", Final Report to Transport Research and Innovation Monitoring and Information System, Project AGB 2004/010, July 2011.

[22] J. Lampinen, A. Vehtari, and K. Leinonen, "Application of Bayesian Neural Network in Electrical Impedance Tomography", IEEE Xplore, Vol. 6, p. 3942-3947, July 1999.

[23] T.T. Grove, M. F. Masters, and R.E. Miers, Determining Dielectric Constants Using a Parallel Plate Capacitor, American Journal of Physics, Vol. 73, p. 53, 2005.

[24] W. Yang, "Design of Electrical Capacitance Tomography Sensors", IOP Science Measurement Science and Technology , Vol. 21, No. 4, p. 14, 2010.

[25] W.Q. Yang, "Modelling of Capacitance Tomography Sensors", IEEE Xplore, Vol. 144, No. 5, p. 203-208, September 1997.

[26] Y. Ru, C. Pradeep, and S. Mylvaganam, "Neural Networks in Electrical Capacitance Tomography (ECT)-Based Interface Detection", IOP Science Measurement Science and Technology, Vol. 22, p. 104006-104019, October 2011.

[27] Z. H. Dughaish, "Variation of the Dielectric Properties of Low Density Polyethylene (LDPE)

with Heat Treatments and UV-Irradiation", Journal of Natural Sciences and Mathematics, Qassim University, Vol. 6, p. 63-72, January 2013.

[28] Q. Marashdeh, Y. Alghothani, G. Legg, B. Seavey, and B. Hunter. "Electrical Capacitance Volume Tomography Sensor For Inspection of Post-Tensioned Tendons", United States Patent 9,535,026 B2. January 03, 2017. See also: TendonScan® Online posting at: https://www.infrastructurepc.com/maintaining-our-infrastructure-with-tendonscan-post-tension-tendon-inspection-service/

[29] L. V. Taveira, A. A. Sagüés, J. Lopez-Sabando, and B. Joseph, "Early Warning Corrosion Detection in Post Tensioned Tendons", Final Report to Florida Department of Transportation, Contract No. BD544-08, p. 71, October 31, 2007.

[30] L. V. Taveira, B. Joseph, and A. A. Sagüés, "Electrochemical Noise Corrosion Monitoring of Post Tensioned Tendons", ECS Transactions Vol. 13, Issue 13, p. 129-138, 210th ECS Meeting, 3October 29-November 3, 2006, Cancun, Mexico, "Corrosion of Infrastructure", The Electrochemical Society, Pennington, NJ, 2007.

[31] L. V. Taveira, A. A. Sagüés, J. Lopez-Sabando and B. Joseph, "Detection of Corrosion of Post-Tensioned Strands in Grouted Assemblies", Paper No. 08398, p. 20, Corrosion/08, NACE International, Houston, 2008.

[32] U. Klein, W. Vollmann, and P.J. Abatti, "Contact Potential Differences Measurement: Short History and Experimental Setup for Classroom Demonstration", IEEE Transactions on Education 46, p. 338–344, 2003.

[33] A. A. Sagüés and M. Walsh, "Kelvin Probe Electrode for Contactless Potential Measurement on Concrete – Properties and Corrosion Profiling Application", Corrosion Science, Vol 56, p. 26-35, 2012.

[34] M. Mariscotti, F. Jalinoos, T. Frigerio, M. Ruffolo and P. Thieberger, "Gamma-Ray Imaging for Void and Corrosion Assessment", Concrete International, p. 48-53, November 2009.

[35] M. Mariscotti, F. Jalinoos, T. Frigerio, M. Ruffolo and P. Thieberger, "Gamma-Ray Imaging for Void and Corrosion Assessment in PT Girders, NDE/NDT for Highways and Bridges" – Structural Materials Technology (SMT), Oakland, CA, September 2008.

[36] M. Mariscotti, P. Kelly, J. Boselli, T. Frigerio, M. Ruffolo and P. Thieberger, "Determination of Grouting Defects in "Deep" PT Ducts Using Gamma Rays", Paper Summary, 2014 FWHA/ASNT SMT Conference, Washington, DC, August 25-27, 2014.

[37] S. Hurlebaus, M.D. Hueste, M.M. Karthik, and T. Terzioglu. "Condition Assessment of Bridge Post-Tensioning And Stay Cable Systems Using NDE Methods". Final Report for National Cooperative Highway Research Program, Project No. 14-28. p. 810, September 2016.

[38] S. Hurlebaus, M.D. Hueste, M.M. Karthik, and T. Terzioglu, "Inspection Guidelines for Bridge Post-Tensioning and Stay Cable Systems Using NDE Methods". Research Report 848 for National Cooperative Highway Research Program, Transportation Research Board, National Academics of Sciences, Engineering and Medicine, Washington, DC, The National Academies Press, 2017.

[39] D. Dukeman, H. Freij, and A. A. Sagüés, C. Alexander. "Field Demonstration of Tendon

Imaging Methods", Final Report to Florida Dept. of Transportation, Contract BDV25-977-52, 44 pp, June 2019.

[40] N. Li, M. Cao, K. Liu, C. He, and B. Wu, "A boundary detecting method for post-tensioned pre-stressed ducts based on Q-factor analysis", Sensors and Actuators A: Physical, Vol. 248, p. 88-93, 2016.

[41] S. Schorn, "Grout Evaluation of External PT Tendons", National Bridge Preservation Partnership Conference Orlando, Florida, 2018.

[42] A.A. Sagüés, "Systems and methods for determining strand position in a post-tensioned tendon" Patent No.: US 9,651,357 B1, May 16, 2017.

[43] S. Goldman, Transformation Calculus and Electrical Transients, Prentice-Hall, Englewood Cliffs, NJ, p. 113, 1995.

[44] R. S. Davis, Using Small, Rare-Earth Magnets to Study the Susceptibility of Feebly Magnetic Metals, Am. J. Phys. 60 (4), April 1992.

[45] M.E. Orazem, and B. Tribollet. Electrochemical Impedance Spectroscopy, Wiley, Hoboken, NJ. 2008.

[46] CRC Handbook of Chemistry and Physics, 53rd edition, CRC Press, Cleveland, 1972

[47] McCarter W.J., Garvin S., Bouzid N. "Impedance Measurements on Cement Paste", Journal of Materials Science Letters, Vol. 7, Issue 10, pp.1056-1057.1988.

[48] McCarter W.J. "The a.c. impedance response of concrete during early hydration", Journal of Materials Science, Vol 31, Issue 23, pp. 6285-6292. 1996.

[49] Euclid Chemical, "EUCO Cable Grout PTX High Performance Cable Grout", viewed July 2 2018,
<https://www.euclidchemical.com/fileshare/ProductFiles/TDS/Euco_Cable_Grout_PTX.pdf>.

[50] S. C. Kranc, and A.A. Sagüés, "Polarization Current Distribution and Electrochemical Impedance Response of Reinforced Concrete When Using Guard Ring Electrodes", Electrochimica Acta, Vol. 38, No. 14 p. 2055-2061, 1993.

[51] M. Soutsos, J.H. Bungey, S.G. Millard M.R. Shaw, and A. Patterson, "Dielectric properties of concrete and their influence on radar testing". NDT & E International. 34. 419-425. 10.1016/S0963-8695(01)00009-3. 2001.

APPENDIX A: GROUT PARAMETERS AND TEST TENDONS

A.1 Grout Electric Properties

Portions of the two grout batches were used to fill two tendon segment specimens (Figure 5.2a) and a four small cylinders (Figure A.1) for assessment of resistivity by a conventional method (MILLER 400D soil resistance meter, which operates at a frequency of 97 Hz), and of electrochemical impedance spectroscopy (EIS, Gamry 600 potentiostat) over a 1Hz to 1 MHz frequency range. Both techniques used a 4-point Wenner array configuration.

The Wenner array electrodes were configured by drilling four equispaced holes in the cylinder mold and inserting 10-24 stainless steel screws penetrating ~3 mm into the grout (Figure A.1). The electrodes were connected in a 4-point configuration to the soil resistance meter (I and E indicate current and potential terminals respectively) or connected in left-to-right order in Figure A.1 as working-working sense-reference-counter electrode to the EIS potentiostat.

The meter resistance reading Rm, or the complex impedance measurement Zm reported by the EIS instrument, both in ohms (Ω), were converted to resistivity ρ or volumetric impedance (sometimes called impeditivity as being the complex analog of the resistivity) Z respectively, both in Ω-cm, by:

$$\rho = Rm * 2 * \pi * a * \frac{1}{k} \tag{1}$$

$$Z = Zm * 2 * \pi * a * \frac{1}{k} \tag{2}$$

Where:

a is the inter-electrode spacing

k is the cell constant that accounts for the medium not being the semi-infinite domain of a

traditional Wenner test [1].
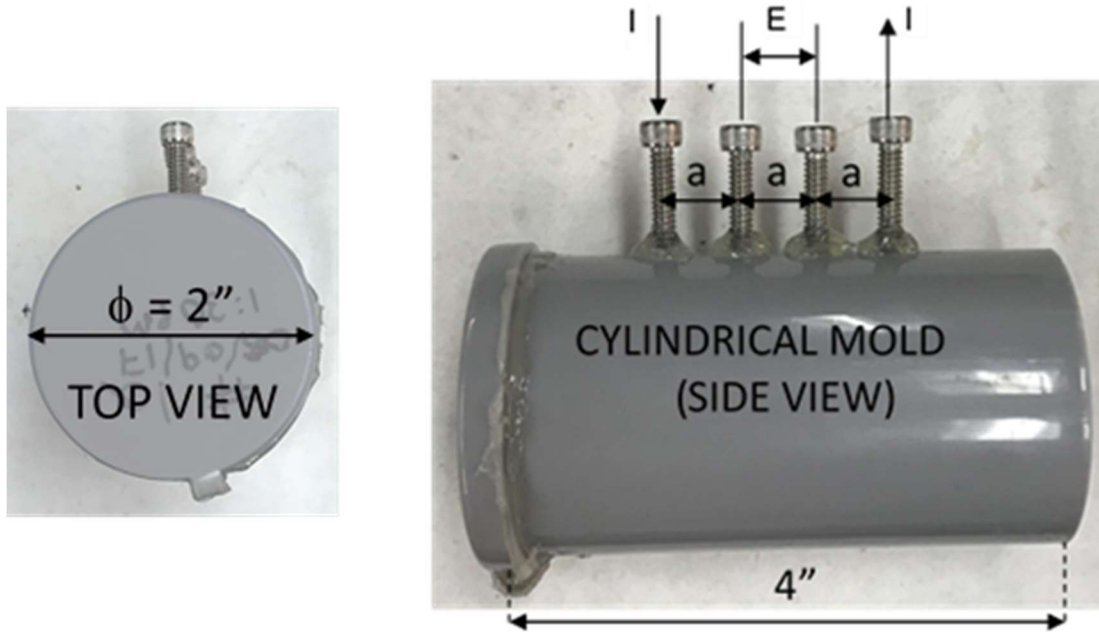
Figure A.1 Top and side view of cylindrical mold used for EIS, resistivity Wenner array test. Mold dimensions are internal.

The volumetric impedance of the grout is numerically (disregarding dimensions) equal to the value of impedance that would be obtained if measuring the impedance of a cube of the grout 1 cm on the side, with electrodes placed at opposite faces and while maintaining an ideal one-dimensional current flow between the two electrodes. A similar relationship applies to the resistivity and the resistance of a 1 cm cube. The EIS results per Eq. (2) are the real (Z') and imaginary (Z'') components of the volumetric impedance, which can be expressed as a complex phasor:

$$Z = Z' + j\,Z''$$ (3)

where:

$$j = \sqrt{(-1)}$$

The inverse of the Z phasor is the volumetric admittance $Y = 1/Z$ (sometimes called admittivity), expressed as:

$$Y = Y' + j\,Y''$$ (4)

The combined results for each frequency are displayed as Nyquist plots in Figures A.2 and A.3, exemplifying two of a set of four tests made approximately 193 days after the specimens were cast, illustrating typically reproducible behavior.

The shape of the Nyquist diagrams in Figures A.2 and A.3 indicates that the high frequency complex impedance behavior (of interest to the imaging application) can be represented as being equivalent to a parallel combination of a constant phase element (CPE) of admittance with a resistor R_P.

The CPE admittance is expressed as:

$$Y = Yo * j \omega^n \tag{5}$$

where:

Yo and n are the CPE parameters.

$$\omega = 2 \pi f$$

f is the frequency at which the measurement was made.

At the low frequencies a constant imaginary component behavior is observed, but that feature is not important to the imaging data interpretation and will not be considered further here.

The values of Yo, n and R_P were abstracted from the EIS results by least square fit of the data for the frequency range 15.89 kHz to 1 MHz with results shown in Table A.1.

Table A.1 – EIS results for grout specimens

Specimen	Yo (S/cm)	Rp (kΩcm)	n
1a	5.81E-10	89.5	0.701
2b	5.38E-10	79.1	0.695
3a	3.01E-10	79.8	0.743
3b	2.38E-10	88.5	0.754

Figure A.2 Nyquist diagrams (Left: Impeditivity; Right: Admittivity) for grout in test cylinder 1a using the Wenner array test to determine impedance behavior of grout. Frequency range shown, 5 points/decade. Specimen age after casting: 193 days.

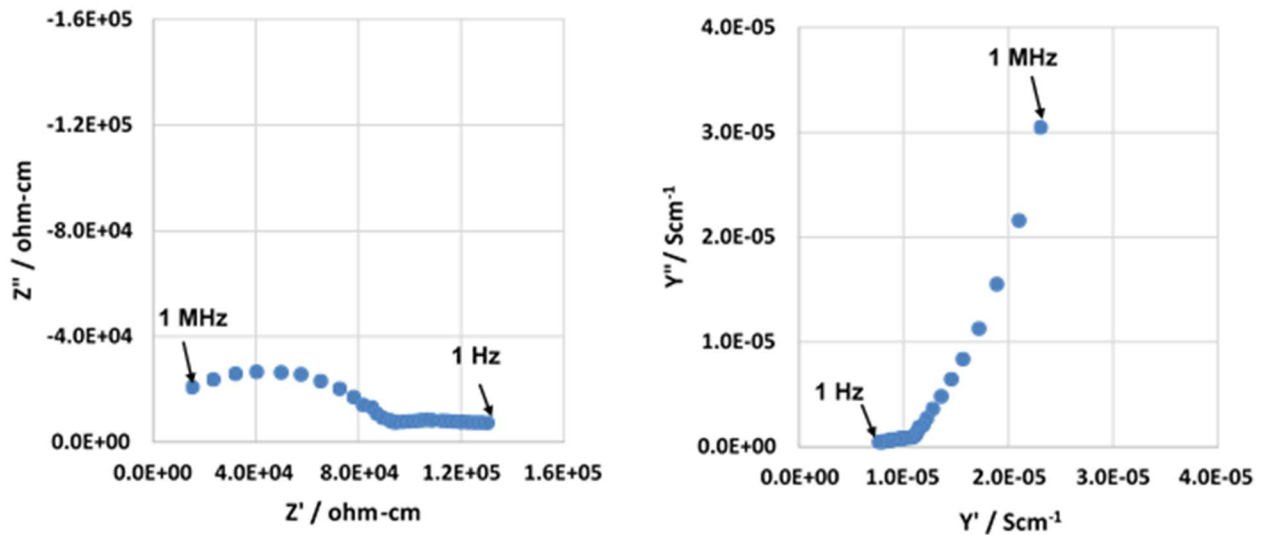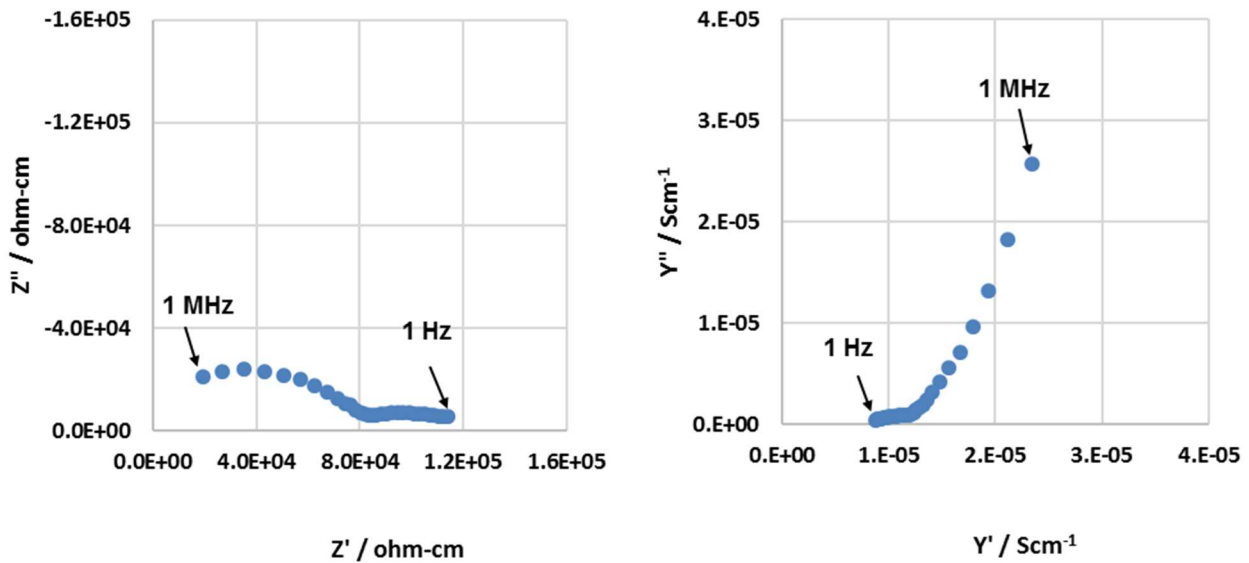Figure A.3 Nyquist diagrams (Left: Impeditivity; Right: Admittivity) for grout in test cylinder 2b using the Wenner array test to determine impedance behavior of grout. Frequency range shown, 5 points/decade. Specimen age after casting: ~193 days.

For the COMSOL model simulations platform used the materials dielectric constant and conductive properties must be entered in terms of an electric relative permittivity ε_{eq} and an electric conductivity σ_R. Those parameters are related to the EIS parameters in Eqs. (3-4) by the following conversions:

$$\sigma_R = \frac{1}{R_P} + Y' \tag{6}$$

$$\varepsilon_{eq} = \frac{jY''}{\varepsilon_o * 2 * \pi * f} \tag{7}$$

where,

ε_o is the permittivity of free space with a value of ~8.854 x 10^{-12} F/m.
To obtain the parameters for a given tendon imaging test frequency the above equations are adapted to account for the CPE behavior by:

$$Z = \frac{1}{Yo * (j\omega)^n} \tag{8}$$

$$Y = Yo * (j\omega)^n = Yo * \omega^n * \cos\left(\frac{n*\pi}{2}\right) + Yo * \omega^n * \sin\left(\frac{n*\pi}{2}\right) \tag{9}$$

For model (COMSOL):

$$\sigma_R = \frac{1}{R_P} + Yo * \omega^n * \cos\left(\frac{n*\pi}{2}\right) \tag{10}$$

$$\varepsilon_{eq} = \frac{Yo * \omega^{n-1} * \sin\left(\frac{n*\pi}{2}\right)}{\varepsilon_o} \tag{11}$$

Using Table A.1 parameters and Eqs. (10 and 11) the average resulting values were used for the exploratory simulations shown in the modeling section.

The single-frequency geometry-corrected resistivity measurements were not used for the COMSOL parameter abstraction but were useful to assess the evolution of the grout during the curing period, and to estimate when the grout had reached to a stable regime representative to that encountered in the field. Figure A.4 shows the characteristic resistivity (inverse of average inverse resistivity) of four replicate cylinders from the two grout batches as function of curing time. The data were corrected for temperature. The reference temperature chosen was 24 ºC assuming that 1 degree increase in temperature decreased the measured resistivity by 3 percent [2].
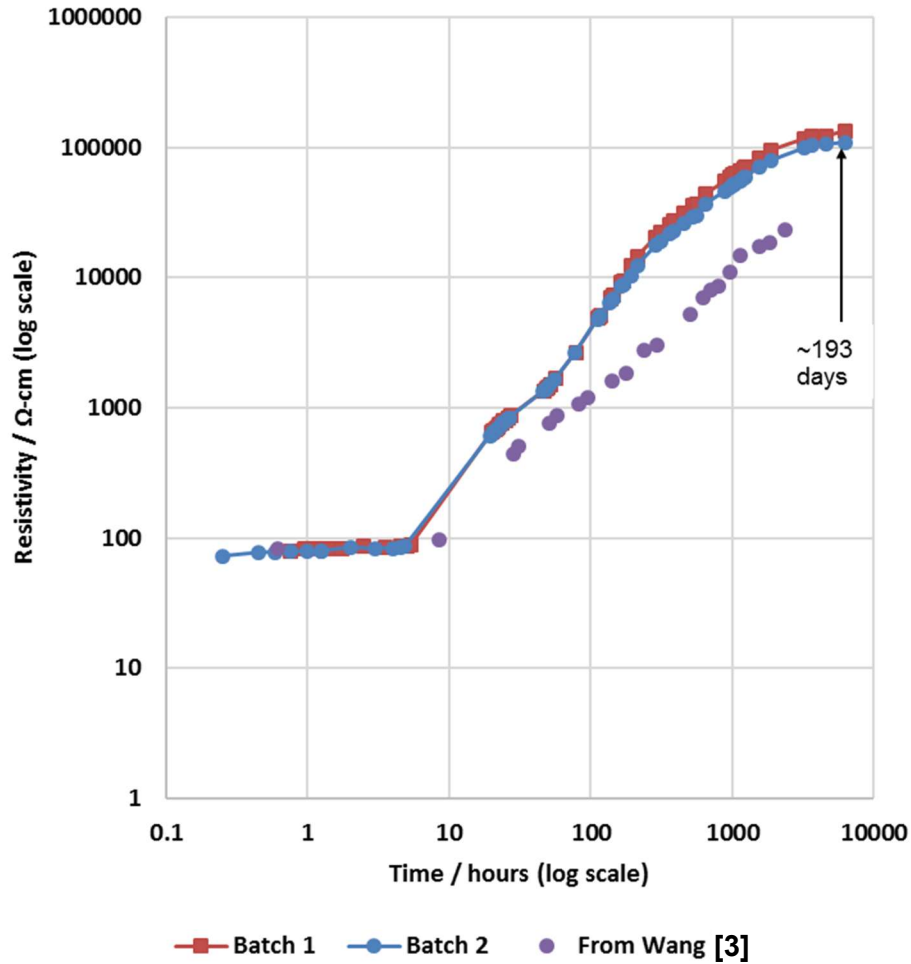
Figure A.4 – Average resistivity of grout cylinders vs. time corrected for geometry and temperature. Shown for comparison are data for a representative grout from an earlier investigation of modern grouts [3]

The trend of increasing resistivity with age toward values that can be >> 10 kΩ-cm is as expected from prior work for modern low bleed grouts with low w/grout ratios as reported by Wang [3]. This is evidenced by the data from that investigation for a grout (identified there as "B") that had behavior in the middle of the range of a group of similar products.

The arrow in the figure above indicates the resistivity value at 193 days which corresponds to the same time the EIS test were conducted (Figures A.2 and A.3). All three graphs (impedance and single-frequency resistivity) are in good agreement indicating a value of ~100,000 Ω-cm at ~100Hz for that test date. The curves in Figure A.5 indicate also that a mature regime is being approached by that age, which suggests that the results for that condition are relevant for aged grouts in actual tendons in service.

A.2 References

[1] W. Morris, E.I. Moreno and A.A. Sagüés, "Practical Evaluation of Resistivity of Concrete in Test Cylinders Using a Wenner Array Probe", Cement and Concrete Research, Vol. 26, No. 12, p. 1779-1787, 1996.

[2] M. Dugarte, and A.A. Sagüés, "Accounting for Temperature Effects on an Evolving Galvanic Anode Cathodic Protection System for Steel in Concrete", Corrosion 72, p. 1462-1469, 2016.

[3] H. Wang, and A.A. Sagüés, "Corrosion of Post-Tensioning Strands", Final Report to Florida Dept. of Transportation, Contract No. BC353 RPWO#33, November 1,2005.

Part 1: Tests with Tendon #1 replicating the sequence shown for Tendon #2 in Chapter 5.
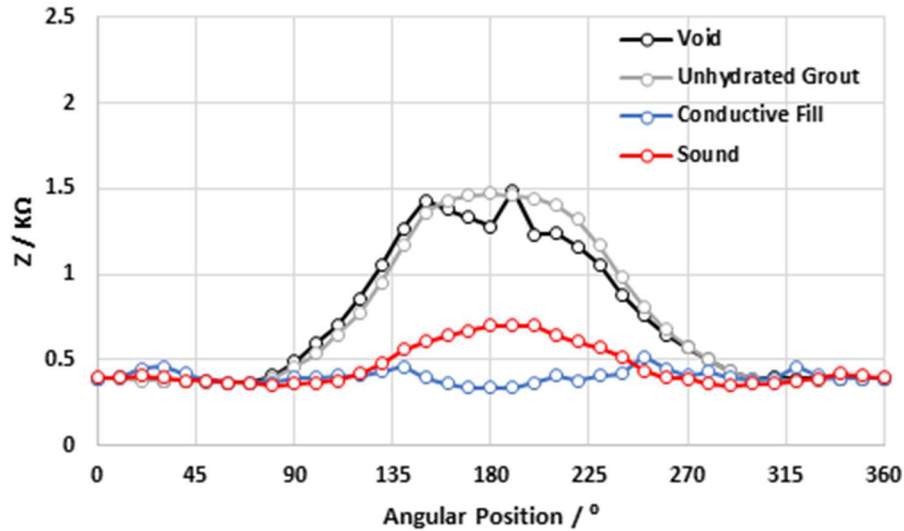
Figure B.1 Real part of the complex impedance vs. angular position for Tendon #1 (age 705 days) at center with section filled with air, unhydrated grout, and conductive fill. Impedance results for a sound cross-section also included.
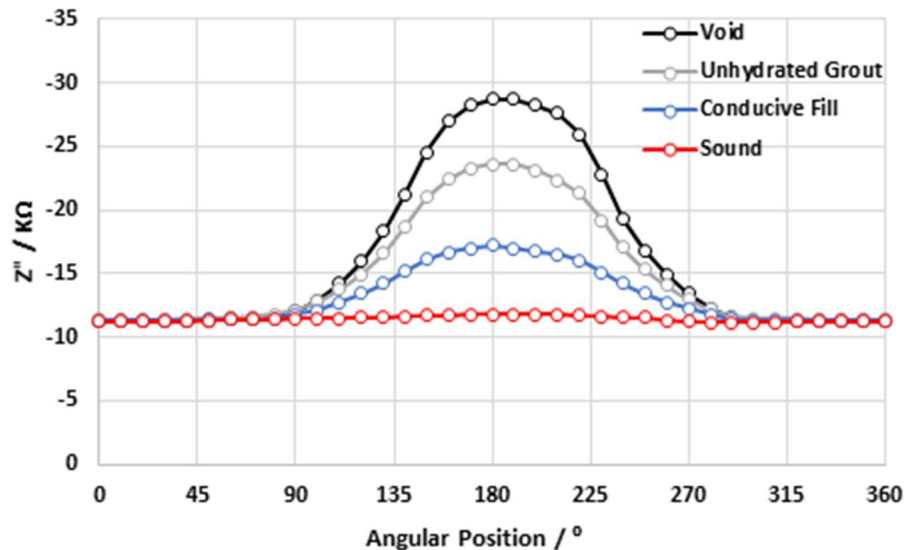
Figure B.2 Imaginary part of the complex impedance vs. angular position for tendon segment #1 (age 705 days) at center with section filled with air, unhydrated grout, and conductive fill. Impedance results for a sound cross-section also included.
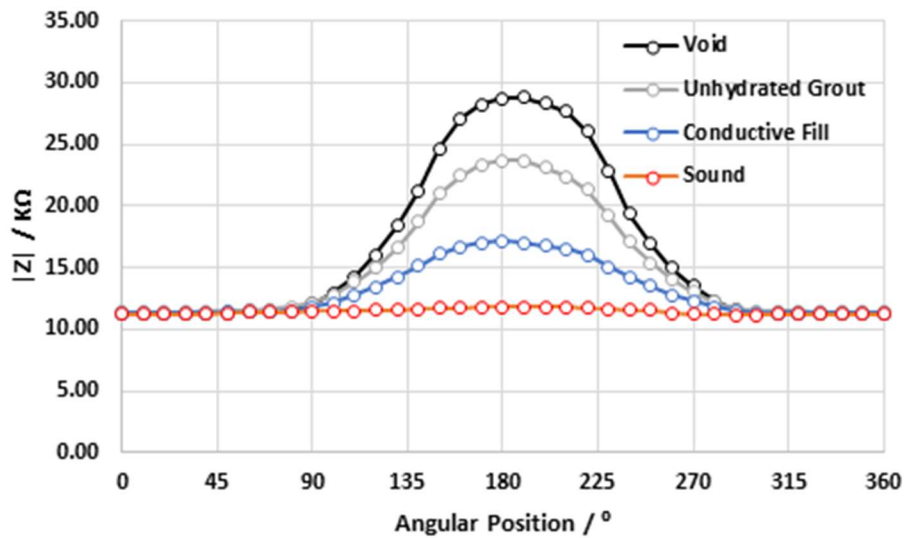
Figure B.3 Modulus of impedance vs. angular position for tendon segment #1
(age 705 days) at center with section filled with air, unhydrated grout, and
conductive fill. Impedance results for a sound cross-section also included.

Part 2: Repeatability/Reproducibility tests showing comparable behavior at early ages in
Tendons #1 and #2, and repeatable results in subsequent early age dates for the same
specimens.
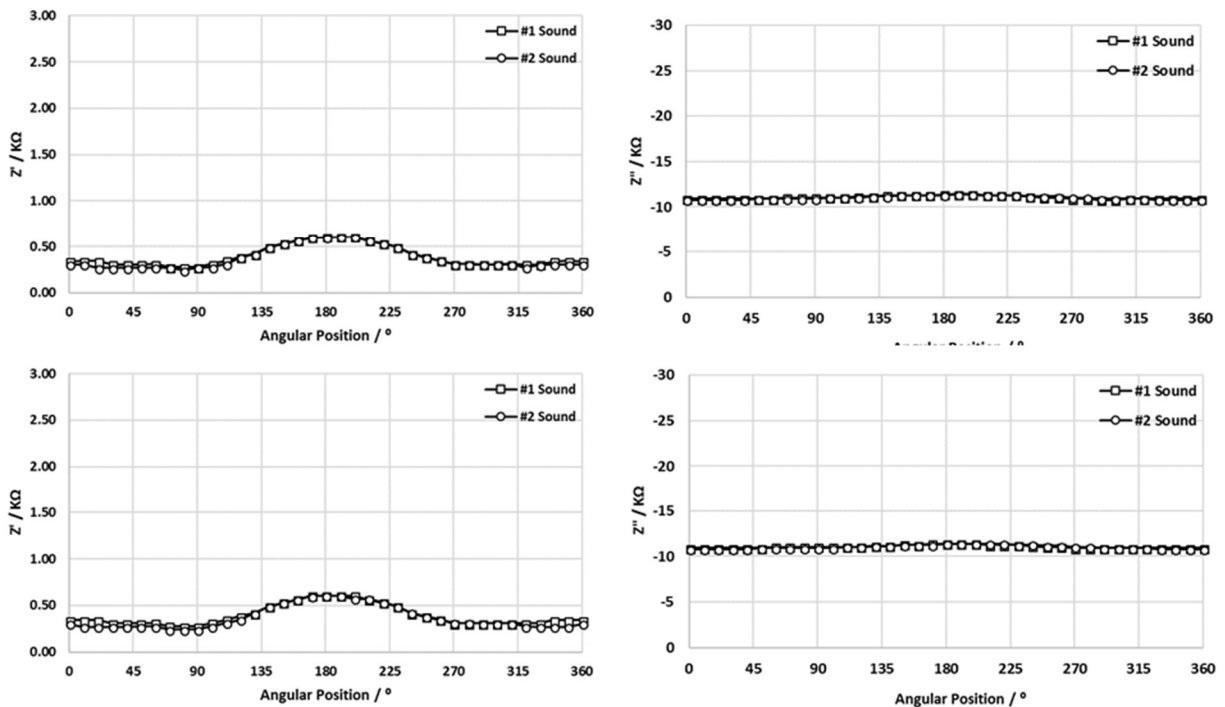
Figure B.4 Complex components of impedance, real (left) imaginary (right), for
tendons #1 and #2 plotted as function of angular position for a cross-section
containing Sound grout. Top and bottom: repeat measurements at ages 64 and
65 days respectively.

105
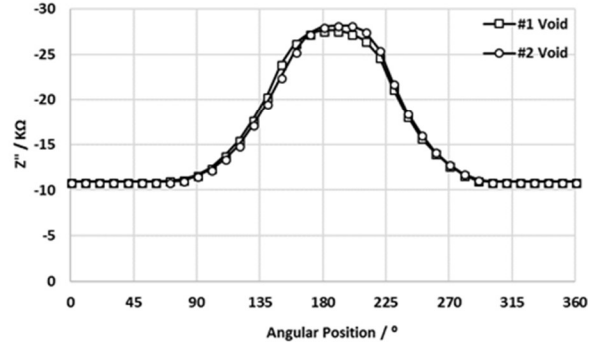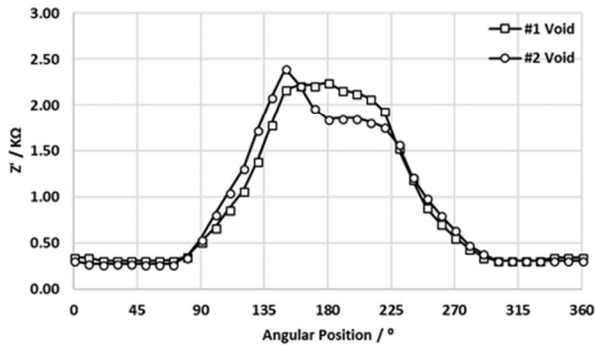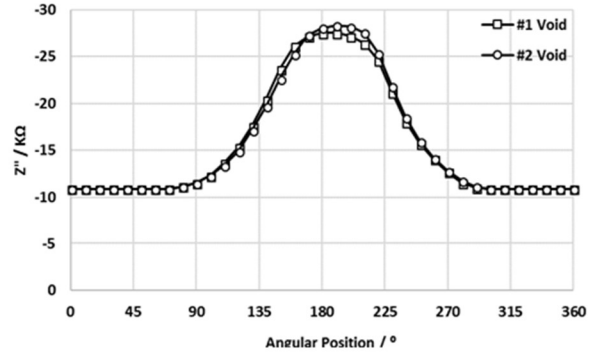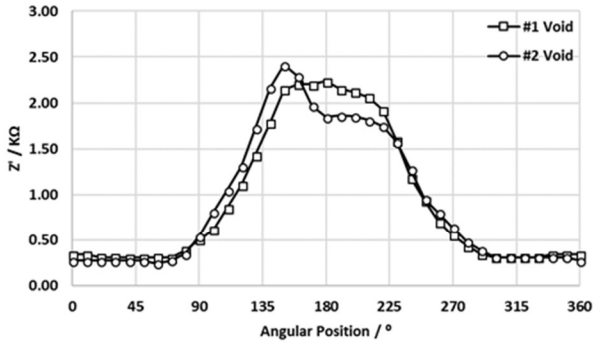
Figure B.5 Complex components of impedance, real (left) imaginary (right), for tendons #1 and #2 plotted as function of angular position for a cross-section of the central Void. Top and bottom: repeat measurements at ages 64 and 65 days respectively.

THASA
TOMOGRAFÍA DE HORMIGÓN ARMADO S.A.

AR Pat. 57580 - US Pat. 8564571 - JP Pat. 4968656 - Mex. Pat. 302854 - China Pat. appl. ZL200780042401.1

Report on

Gamma Ray Tomography Validation Test of

Mock Up Tendons provided by the

University of South Florida

Federal Award No. TWO 977.24
Subawards No. 2104-1245-00-A
Project Title:
Development of Tendon Imaging Sensor.

May 2019

EXECUTIVE SUMMARY

The work described in this report was requested by Prof. Alberto A. Sagues, PhD, P.E., Distinguished University Professor in the Dept. of Civil and Environmental Engineering of the University of South Florida, and is part of a contract between this University and the Florida Department of Transportation.

The purpose of this work is to apply THASA´s Gamma-Ray Tomography techniques to perform validation tests of measurements carried out using a Tendon Imaging Sensor developed by Prof. Sagues and his collaborators as a tool for diagnosing grouting defects and tendon condition of external post-tensioned ducts.

In total 4 samples A, B, C and D, at various sections were studied with gamma rays at different angles, totaling 157 gammagraphies. Special software for this application was developed to analyze these gammagraphies and obtain sectional maps of tendons and grouting densities.

Results are compared with the construction drawing information provided by USF showing good agreement in most cases. We did not observe density differences between "soft" and "sound" grout. Also small voids in areas designated as "water" were found, probably due to incomplete water filling of the samples after arrival at our premises. There is some doubt as to the agreement between density measurements and drawings in connection to the areas designated as "unhydrated".

The present work was carried out with a ^{192}Ir source (10 and 30 Ci) and a Digital Radiography system. Radiological protection measures were taken, following the rules established by the Argentina Nuclear Regulatory Authority (ARN).

* * * * *

METHODOLOGY

THASA uses 3 gamma-ray technologies for the study of reinforced concrete structures. One of these, RCT (Reinforced Concrete Tomography), is applied to the determination of diameters and positions of rebars and PT ducts, with the precision required for structural verification. Another, DVC (Determination of voids and corrosion), is a technique developed to assess the (X, Y, Z) extension of voids, corrosion and other defects as well as densities of the materials traversed by the gamma rays. The third method, DRCT (Deep Reinforced Concrete Tomography), in which gammagraphic plates are substituted by small gamma-ray spectrometers, is used for the inspection of rebars and ducts located "deep" in large concrete samples where gammagraphy is not applicable.[4]

The process of analysis of the gammagraphies applied in this work entails the first two of the mentioned techniques and the data analysis involves two steps: 1) the determination of the area occupied by the strands and, 2) the determination of the grouting (or lack of) densities outside the tendon area.

1. Tomography (RCT)

As mentioned, RCT is applied to obtain positions and diameters of cylindrical objects such as rebars and ducts and for this purpose usually two irradiation angles suffice to get these quantities.

Fig. 1 illustrates how this is done by measuring the position of the steel bar shadows projected on the gammagraphic plates in two separate irradiations with the source displaced horizontally 5-10". The position of the shadow is a function of the size of the bar and its position in the Z axis. Given the source and plate position in each case, the shadows define "cones". These cones intersect at the bar location with the same width. Thus rebar position *and* diameter are determined univocally by measuring size and position of the shadows.

---

[4] See for example Determination of Grouting Defects in "Deep" PT Ducts Using Gamma Rays, Mario A. J. Mariscotti, Paul Kelly, Joaquín Boselli, Teresita Frigerio, Marcelo Ruffolo, Peter Thieberger. ASNT 2014 NDE/NDT for Highways and Bridges: Structural Materials Technology Conference. Washington DC, USA. August, 2014. The results of this work were presented in a meeting that took place at Florida State Department offices in Gainesville, on Oct 2013.

Actually, THASA owns a US Patent, which shows that by using the penumbra concept, only one irradiation may be enough to obtain this same result if the gammagraphy quality is good.[5]
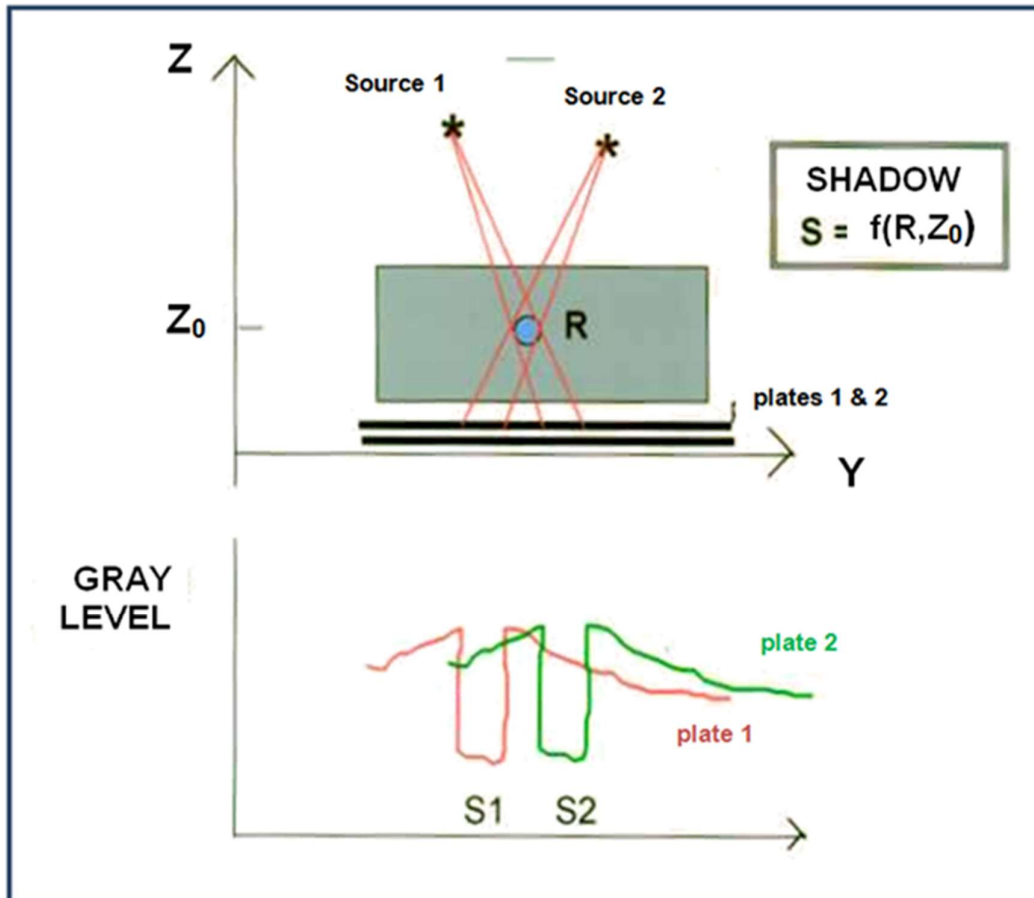
Fig. 1. Illustration of how position and diameters of steel bars are determined by RCT performing 2 irradiations at different angles.

The procedure applied in this work for step 1 (location of strand/tendon and grouting defects) includes:

1) Load positions of source, sample and plates. Fig. 2 shows the program screen corresponding to this action for a particular duct.

---

[5] Process for determining the internal three-dimensional structure of a body opaque to visible light by means of radiations from a single source, especially suitable for reinforced concrete parts.US Patent # 5,828,723,oct 27, 1998.
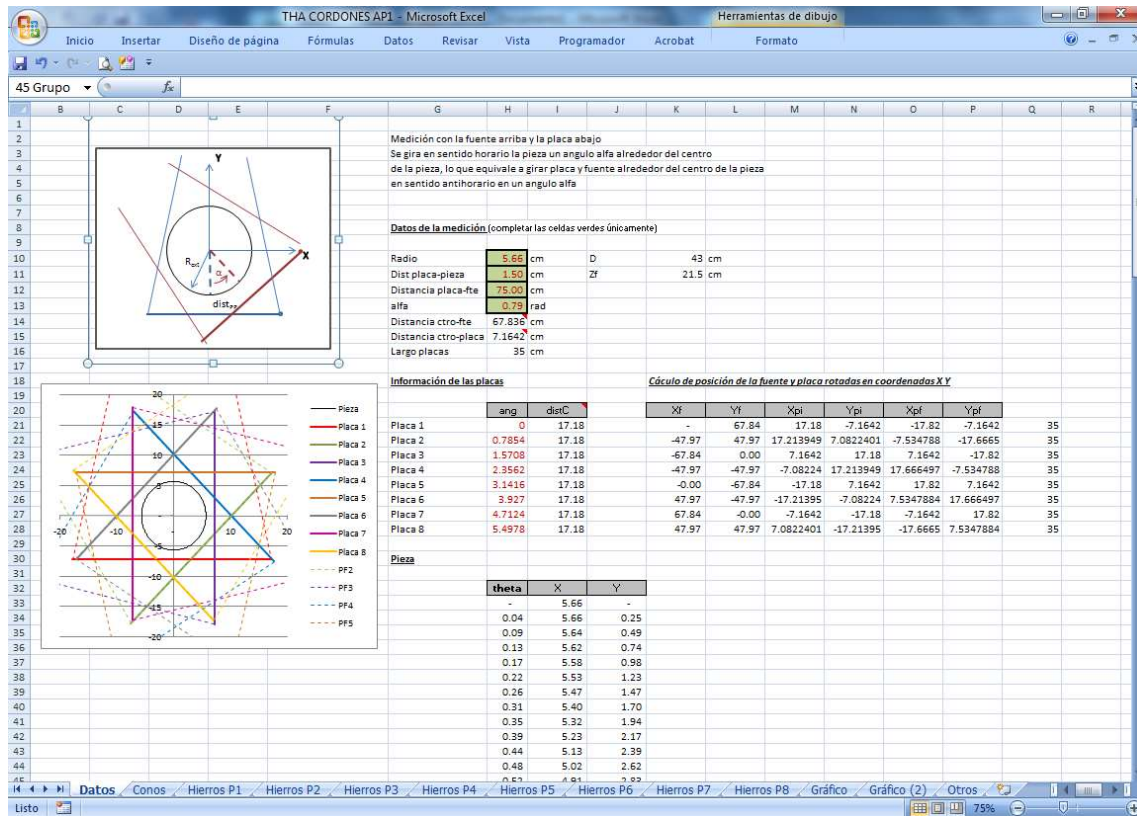
Fig. 2. Program screen with the data and drawings of sample and plate orientations. The upper graph is used to define coordinates and parameters.

2) Read off and input the X1 and X2 values of each strand in the program. These values are the X coordinates of the edges of the strand projection on the plate (Fig. 3). Given the source and plate position, each pair of these values defines a cone which is calculated and drawn by the program (Fig. 4).
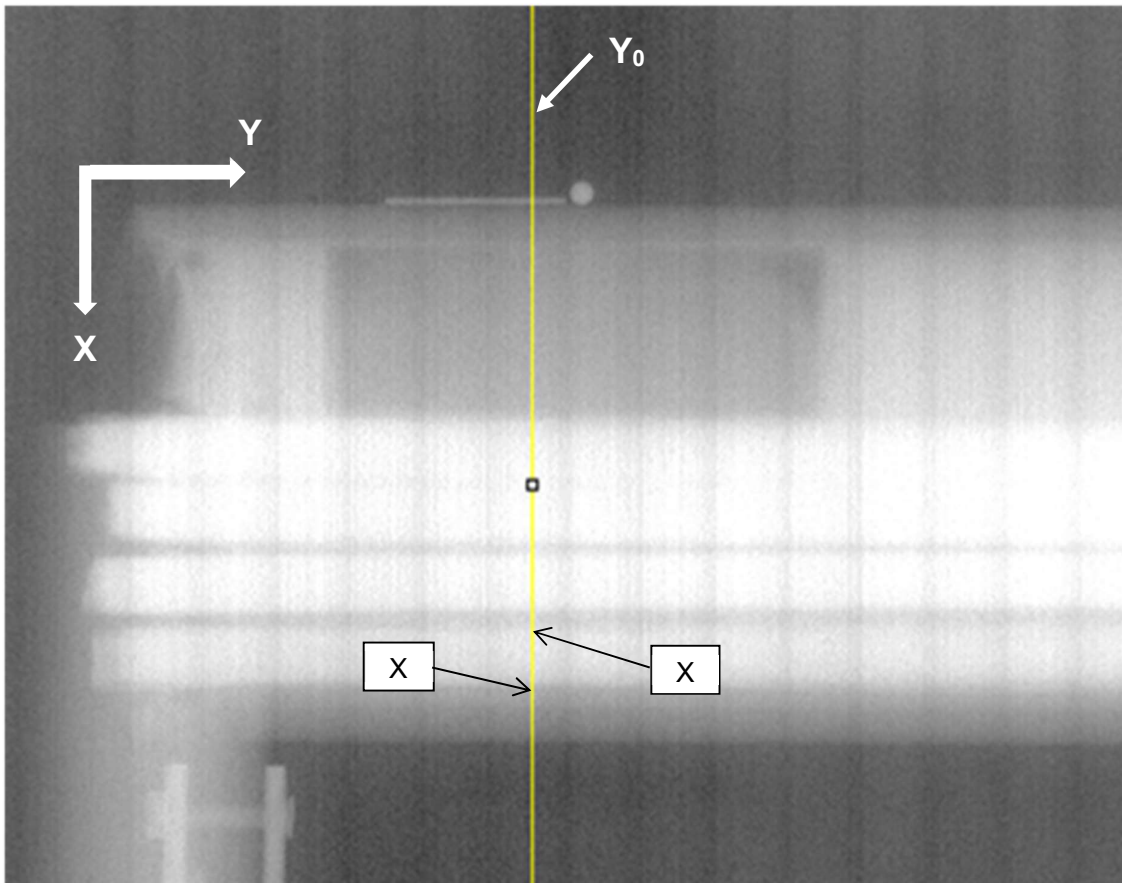
Fig. 3. Gammagraphy of a duct. The whiter horizontal bands are the strands. The X1 and X2 values indicate the pixel position along the X axis (yellow vertical line) of the edges of the strand shadow projected onto the plate. (The vertical dark lines are an instrumental defect).

3) Subsequently, the program draws the cones corresponding to all strands seen in all the gammagraphies taken at different angles for a given sample (Fig. 4).
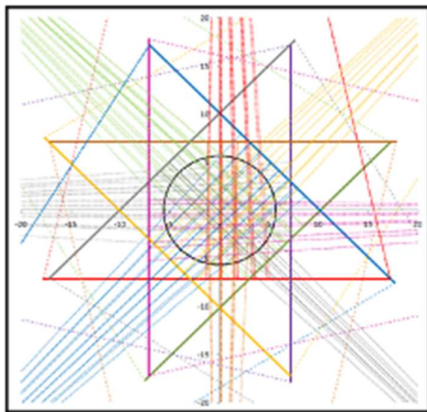
Fig. 4. Program drawing of all cones resulting from the set of X-values for every strand observed in the gammagraphies taken at different angles (shown in different colors).

4) Since the width of a cone defines the diameter of the corresponding strand and this is a

function of the position of the strand along the cone axis, the position and diameter of a strand is determined when two or more cones intersect with the same widths (Fig. 5).
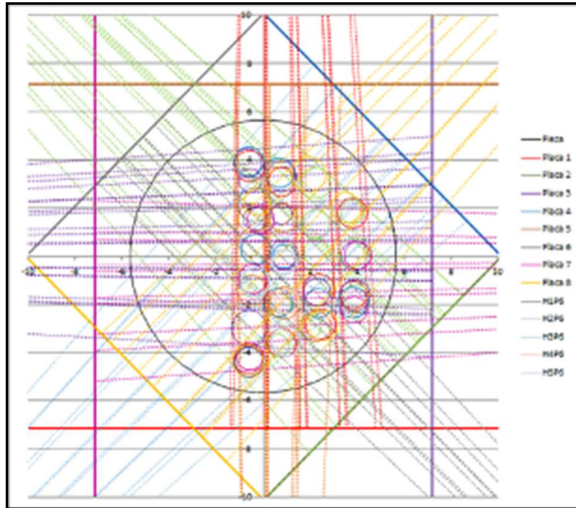
Fig. 5. Program drawing of all cones and intersections defining strands (case of Duct A).

5) Owing to the large number of strands in the present case and taking into account that the purpose of the present work is to determine densities of grouting defects outside the tendon area, only for Duct A we obtained the full tomographic reconstruction of the strands as shown in Fig.5. For the other ducts results are presented showing the area occupied by the whole tendon.

2. Grouting Densities (DVC method)

Step 2 of the data analysis (determination of grouting densities) implies selection of those gammagraphies taken at angles where grouting defects are most noticeable, and perform a fitting procedure in order to determine the density of the grouting in the area of the defect. In this fitting procedure we have left aside the zones where the strands are projected on the gammagraphies to reduce uncertainties.

The gamma-ray intensity calculated using the known physical law of radiation attenuation in matter is compared to the measured photographic density observed in the gammagraphies. The photographic density is, in the case of digital plates, proportional to gamma-ray intensity. Hereafter we use *gray level* G as equivalent to photographic density. The measured gray levels $G_m(Y_0, X)$ are fitted to the calculated G_c function

$$G_c(Y_0, X) = K \exp(-\mu.\Sigma\delta_i.\tau_i), \tag{1}$$

where K is a constant, μ is a known gamma-ray attenuation coefficient and δ_i and τ_i are the densities and thicknesses of the materials *i* traversed by the gamma radiation, respectively. Y_0 is the Y coordinate of the data line along the X-axis. An example of this procedure is given in Fig. 6. The gammagraphy on the left shows two ducts, the upper one with a severe grouting defect in the upper part of the duct (dark band). The photographic density along the vertical dotted line indicated on the gammagraphic image is plotted on the right as a function of the X position along that line. The "bowl shape" between points A and B corresponds to the larger absorption due to higher density of the tendon inside de lower duct. Same between D and E for the upper duct. The "peak" between E and F is due to the void in the upper part of the upper duct. By fitting these data to the expected value of photographic density due to the gamma intensity falling onto the gammagraphic plate it was possible to determine a void "depth" $\tau = 5$ cm assuming density $\delta = 0$ (air).[6]

Fig. 6. Gammagraphy of a severe void in a PT duct and its quantitative determination.

---
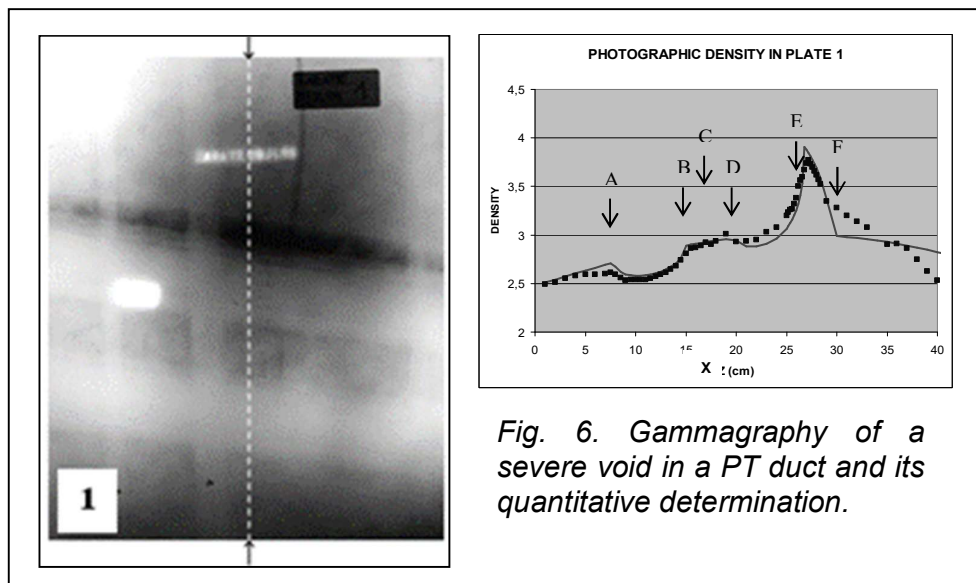
[6] Gamma-ray imaging for void and corrosion assessment in PT girders, M.A.J. Mariscotti, F. Jalinoos, T. Frigerio, M. Ruffolo and P. Thieberger, ASNT, NDE/NDT for Highways and Bridges Conference, Oakland, Sep 2008 and CONCRETE INTERNATIONAL, November 2009.

In the present work, the samples were irradiated in several angles because, unlike previous studies performed by THASA to detect grouting defects, in this case the orientation of these defects could not be presumed, and the goal of this work is to achieve data comparable to that obtained with the USF sensor. The number of measuring angles in each case varied, but it was around 8. A much larger number of angles (as in a medical tomography) would allow the use of conventional tomographic software but it would make it difficult to use this technique for practical purposes in the field. For this reason, in only one case, the detailed tomography of strands is given. In the other cases, we report the area occupied by the tendon as a whole. The thickness of each component is acquired in step 1. By varying δ until the best fit is achieved one obtains the density values.

Fig. 7. Set up used in the present work. The picture shows a sample and the digital plate behind it. The source is 30" to the left of the sample and plate (not shown). On the right hand side is the schematics of this arrangement indicating coordinates and reference.
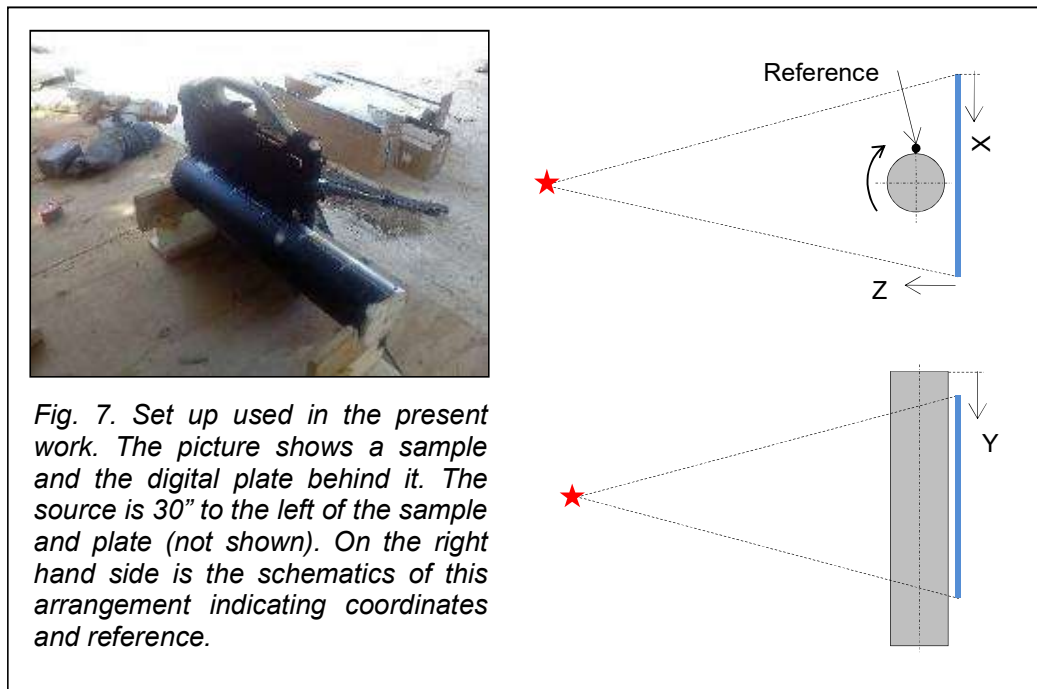
MEASUREMENTS

A total of 157 gammagraphies (see Table I) were taken using an ^{192}Ir source and a Vidisco Flash X digital radiography system with a pixel spacing of 0,141 mm. Each gammagraphy is identified by the sample name (A, B, C or D), the mark (P1, P2, …) at which it was centered and the angle ϕ. Thus AP1–45 means sample A, centered at P1, irradiated at 45 degrees. Irradiation times varied between 1 and 18 sec. Fig. 7 shows the set up and coordinates.

Table I – Gamma-ray scans performed on samples A, B, C and D

	angle (°)	T (s)
AP1	0	3
AP1	45	5
AP1	90	1
AP1	135	1
AP1	180	1
AP1	225	1
AP1	270	1
AP1	315	1
AP1	360	1
AP2	0	1
AP2	45	1
AP2	90	1
AP2	135	1
AP2	180	10
AP2	225	10
AP2	270	15
AP2	315	15
AP3	0	15
AP3	45	15
AP3	90	15
AP3	135	15
AP3	180	15
AP3	225	15
AP3	270	15
AP3	315	15
AP4	0	15
AP4	45	15
AP4	90	15
AP4	135	15
AP4	180	15
AP4	225	15
AP4	270	15
AP4	315	15
AP5	0	15
AP5	22,5	15
AP5	45	15
AP5	67,5	15
AP5	90	15
AP5	112,5	15

	angle (°)	T (s)
AP5	135	15
AP5	157,5	15
AP5	180	15
BP1	0	15
BP1	45	15
BP1	90	15
BP1	135	15
BP1	180	15
BP1	225	15
BP1	270	15
BP1	315	15
BP2	0	15
BP2	45	15
BP2	90	15
BP2	135	15
BP2	180	15
BP2	225	15
BP2	270	15
BP2	315	15
BP3	0	15
BP3	45	15
BP3	90	15
BP3	135	15
BP3	180	15
BP3	225	15
BP3	270	15
BP3	315	15
BP4	0	15
BP4	45	15
BP4	90	15
BP4	135	15
BP4	180	15
BP4	225	15
BP4	270	15
BP4	315	15
CP1	0	15
CP1	22,5	15
CP1	45	15
CP1	67,5	15
CP1	90	15
CP1	112,5	15

	angle (°)	T (s)
CP1	135	15
CP1	157,5	15
CP1	180	15
CP2	0	15
CP2	45	15
CP2	90	15
CP2	135	15
CP2	180	15
CP3	0	15
CP3	45	15
CP3	90	15
CP3	135	15
CP3	180	15
CP4	0	15
CP4	45	15
CP4	90	15
CP4	135	15
CP4	180	15
CP5	0	15
CP5	45	15
CP5	90	15
CP5	135	15
CP5	180	15
CP1	225	6
CP1	270	6
CP1	315	6
CP2	225	6
CP2	270	6
CP2	315	6
CP3	225	6
CP3	270	6
CP3	315	6
CP4	225	6
CP4	270	6
CP4	315	6
CP5	225	6
CP5	270	6
CP5	315	6
DP1	0	6
DP1	45	6
DP1	90	6

	angle (°)	T (s)
DP1	135	6
DP1	180	6
DP1	225	6
DP1	270	6
DP1	315	6
DP2	0	6
DP2	45	6
DP2	90	6
DP2	135	6
DP2	180	6
DP2	225	6
DP2	270	6
DP2	315	6
DP3	0	6
DP3	45	6
DP3	90	6
DP3	135	6
DP3	180	26
DP3	225	6
DP3	270	6
DP3	315	6
DP4	0	6
DP4	45	6
DP4	90	6
DP4	135	6
DP4	180	6
DP4	225	6
DP4	270	6
DP5	0	6
DP5	45	6
DP5	90	6
DP5	135	6
DP5	180	6
DP5	225	6
DP5	270	6
DP5	315	6

RESULTS

The gamma-ray technique provides density values, not the elemental composition of the material traversed by the radiation. Hence, our results are limited to indicate the densities obtained following the procedure explained above for different sections of the samples. Table 2 summarizes the results of all the measurements carried out. Since the purpose of this work is to test the validity of the results obtained with USF technology, Table 2 includes a column with the indication of the defect as designated by USF group (unhydrated grout, air, water, etc.) in order to facilitate the comparison of both sets of results.

The results compared with the construction drawing information provided by USF are also graphically displayed in Figs. 8 to 13 below. In each case, the duct cut views of both USF construction drawings and THASA results are shown. These exhibit the tendon distribution and areas of defects "as built", in the case of the USF drawings, and "as measured", in the case of THASA results (gray for tendon and purple for grouting defects). Below these cut views, the figures show the USF drawings of the defects along the duct, and the corresponding sections of THASA gammagraphies taken at the angle where the defects are most clearly seen. Defects are labeled a_i and b_i to ease identification.

The angle defines the orientation of source and plate with respect to the sample, and the sense and direction of the X coordinate. The plots display the $G_m(Y_0,X)$ values (green solid line) and the fitted ones, $G_c(Y_0,X)$ (red solid line), with the indication of the density values (in g/cm^3) resulting from the fitting procedure. The $G_m(Y_0,X)$ values are those along the horizontal dotted green lines shown on the gammagraphy image. Defect areas are displayed in color.

As mentioned, $G_c(Y_0,X)$ (Eq (1)), depends on the density and thickness of the material traversed by the gamma beam. The thicknesses are known from the previous tomographic analysis using the data from all the gammagraphies at different angles. Hence, by varying the density value until the best fit between G_m and G_c is achieved, the density in the area of the defect, is deduced. As explained above, in this fitting procedure the zones where the strands are projected on the gammagraphies were left aside to reduce uncertainties.

Table II–Summary of the results

Sample	Y_0 value[a] (inches)	Measured densities[b] (g/cm³)	Correspondence with USF data		Comments (see Fig. 8 – 13)
			marks	labels	
A	4.3	1.1 / 1.8	P1	Unhydrated / grout	? / ✓
	7.6	1.8	P2	Grout	✓
	11.6	0.2 / 1.8	P3	Air / grout	✓
	20.9	0 [c]-1.35 / 1.8	P5	Water, gel / grout	We find air (faulty filling?)[c]
B	4.5	0 / 1.8	P1	Air / soft grout	We do not detect grout differences
	6.3	1.8 / 1.8	P2	Soft grout	
	15.5	1.8 / 1.8	P4	Sound grout	✓
	20.0	0 / 1.8	P5	Air / sound grout	✓
C	4.7	1.1 / 0	P1	Unhydrated / air	? / ✓
	12.3	0 / 1.4	P3	Air / unhydrated	✓ / ?
	18.1	1	P5	Water	✓
	19.9-23.6	bolt	P5	Bolt	✓
D	2.9	1.05 / 1.8	P1	Unhydrated / air	Air at center of duct not measured
	10.8	0 / 1.8	P3	Air / air	
	21	0 [c]-1.35 / 1.8	P5	Water / grout	We find air (faulty filling?)[c]
	19.8-23.4	bolt	P5	Bolt	✓

a) Y_0 is the Y-value of the data line selected to perform the fitting procedure. It is measured from the origin of the duct (see Fig. 8 - 13).

b) Density values correspond to areas labeled a_i and b_i in the cut views, gammagraphic images and plots.

c) "Faulty filling" refers to the fact that samples were shipped without water and water was poured in after arrival. It is possible that this process was not properly completed.
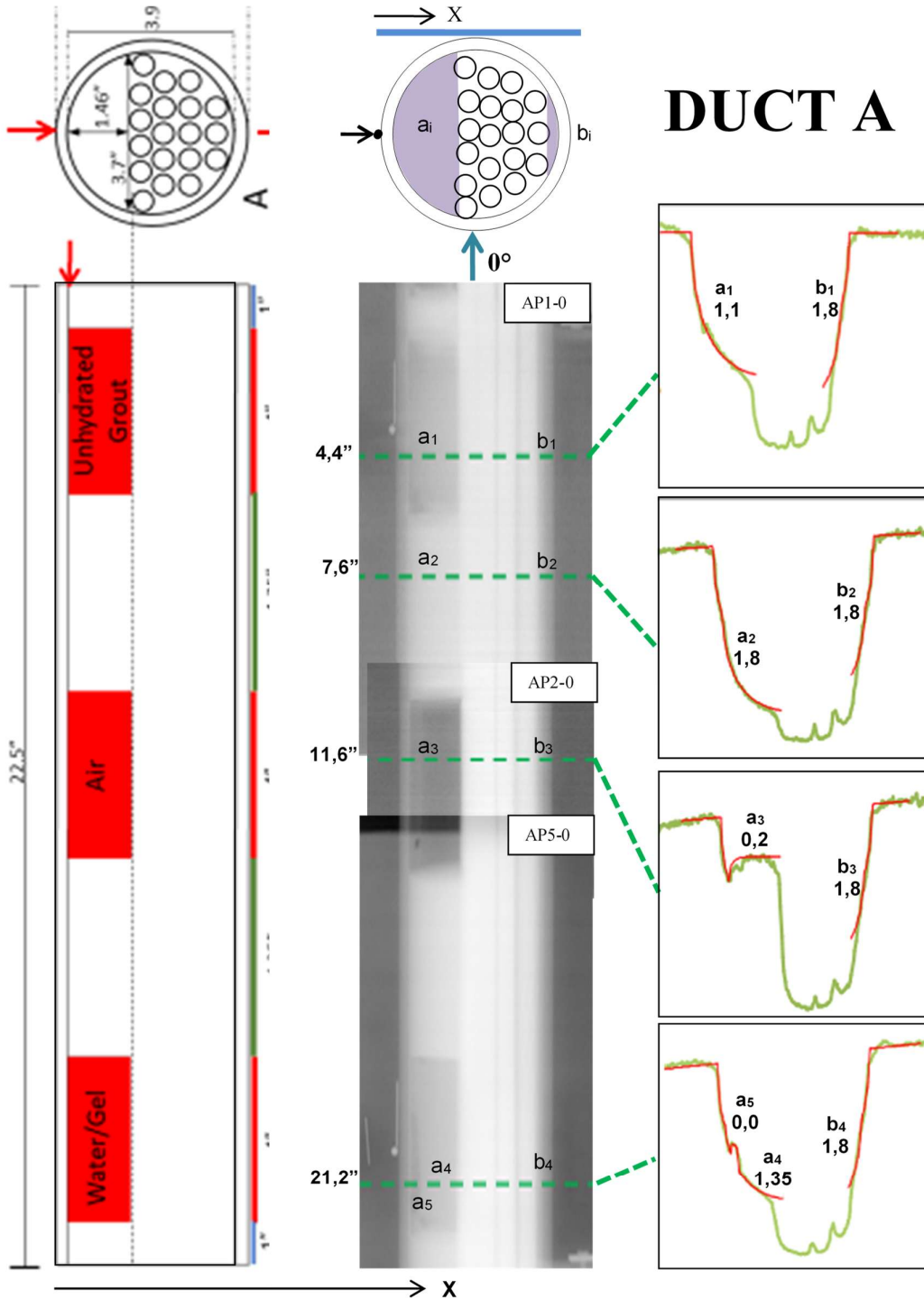
DUCT A

Fig. 8. Results for Duct A. Left: USF construction drawings; Center and right: Results of measurements performed by THASA, (circles indicate strands location; purple, areas of measured grouting defects, see text)
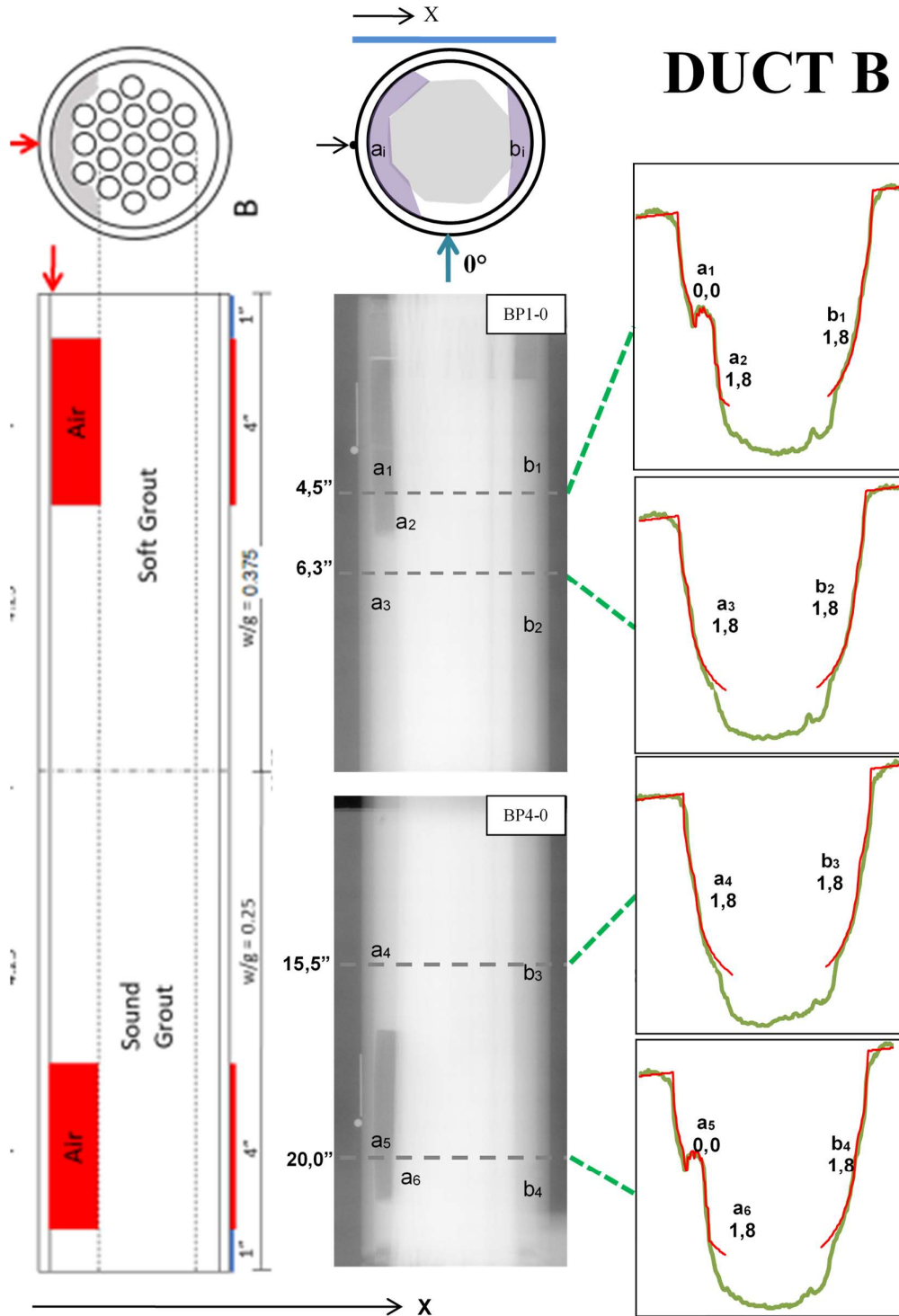
DUCT B

Fig. 9. Results for Duct B. Left: USF construction drawings; Center and right: Results of measurements performed by THASA, (gray indicate tendon location; purple, areas of measured grouting defects, see text).
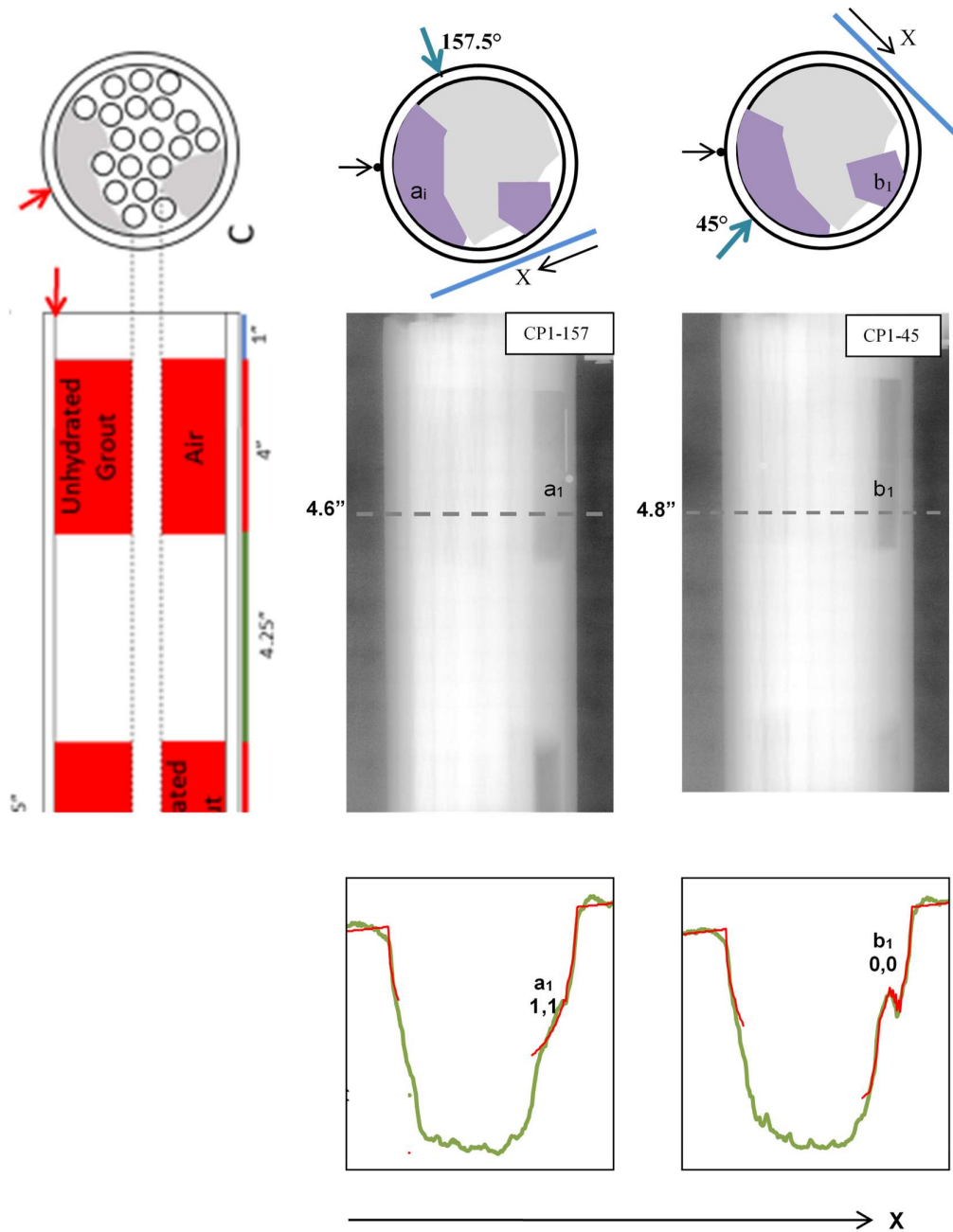
DUCT C (top)

Fig. 10. Results for Duct C. Left: USF construction drawings; Center and right: Results of measurements performed by THASA, (gray indicate tendon location; purple, areas of measured grouting defects, see text).

DUCT C (center)

Fig. 11. Results for Duct C (center). Left: USF construction drawings; Center and right: Results of measurements performed by THASA, (gray indicate tendon location; purple, areas of measured grouting defects, see text).
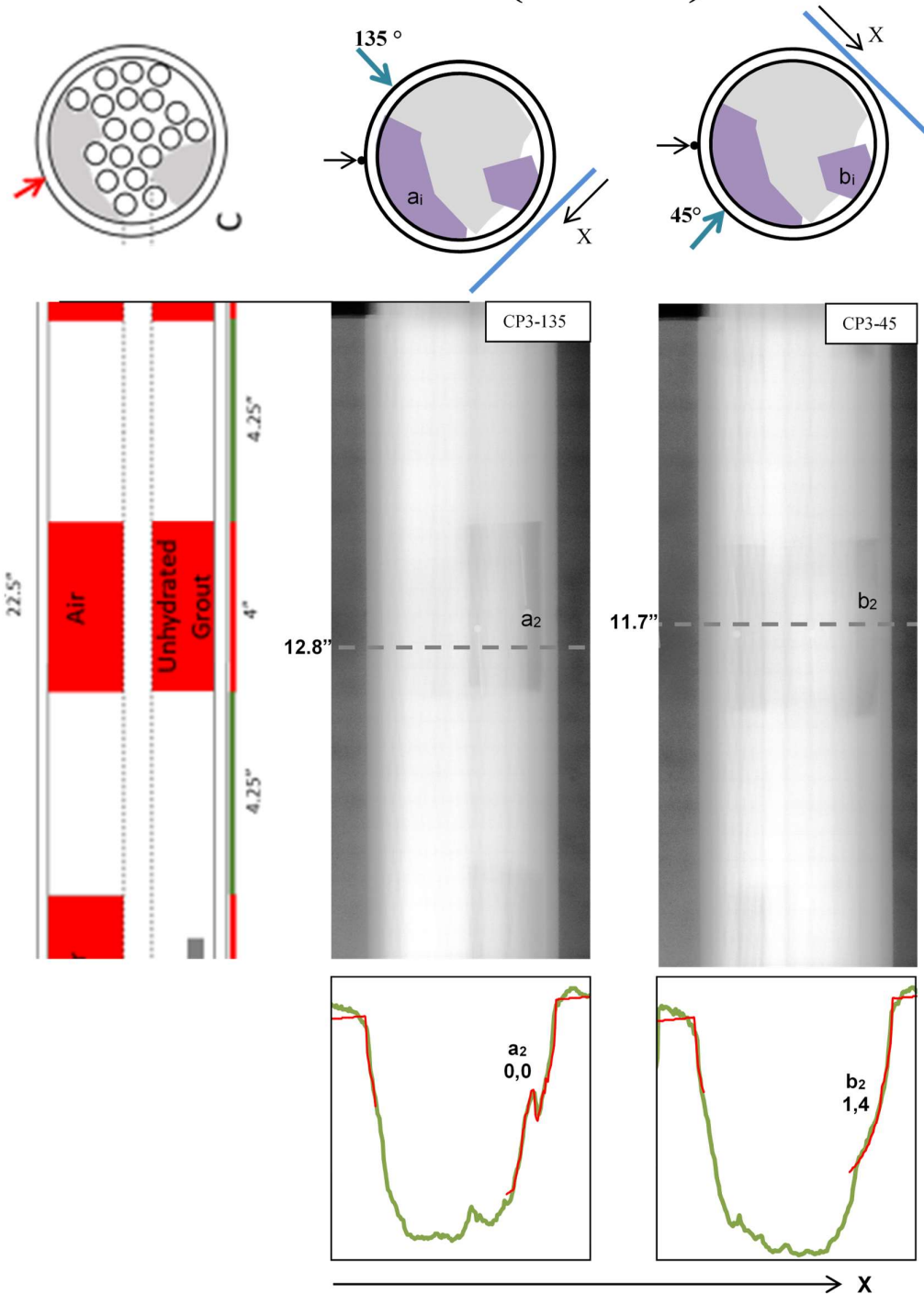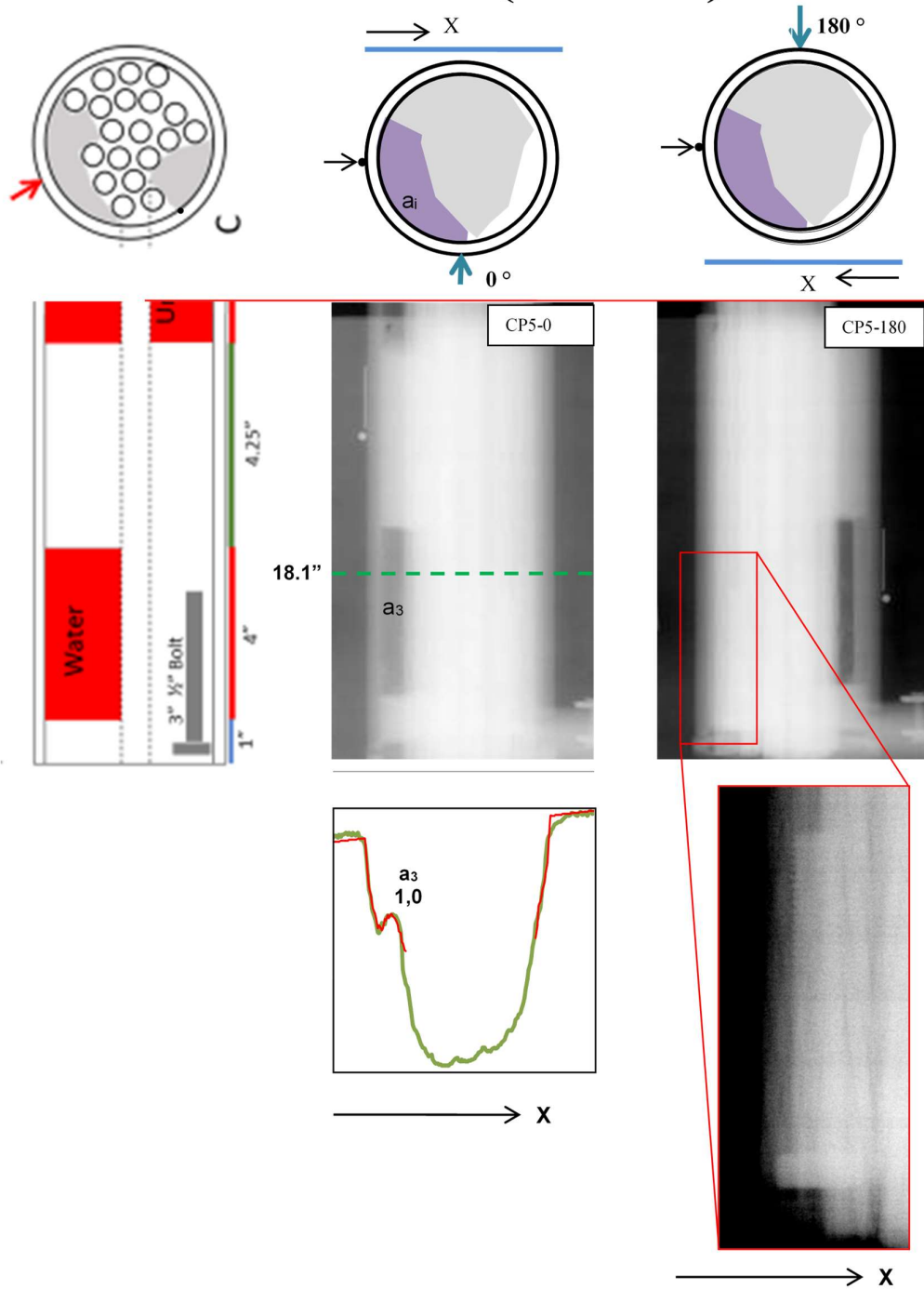
DUCT C (bottom)

Fig. 12. Results for Duct C (bottom). Left: USF construction drawings; Center and right: Results of measurements performed by THASA, (gray indicate tendon location; purple, areas of measured grouting defects, see text).
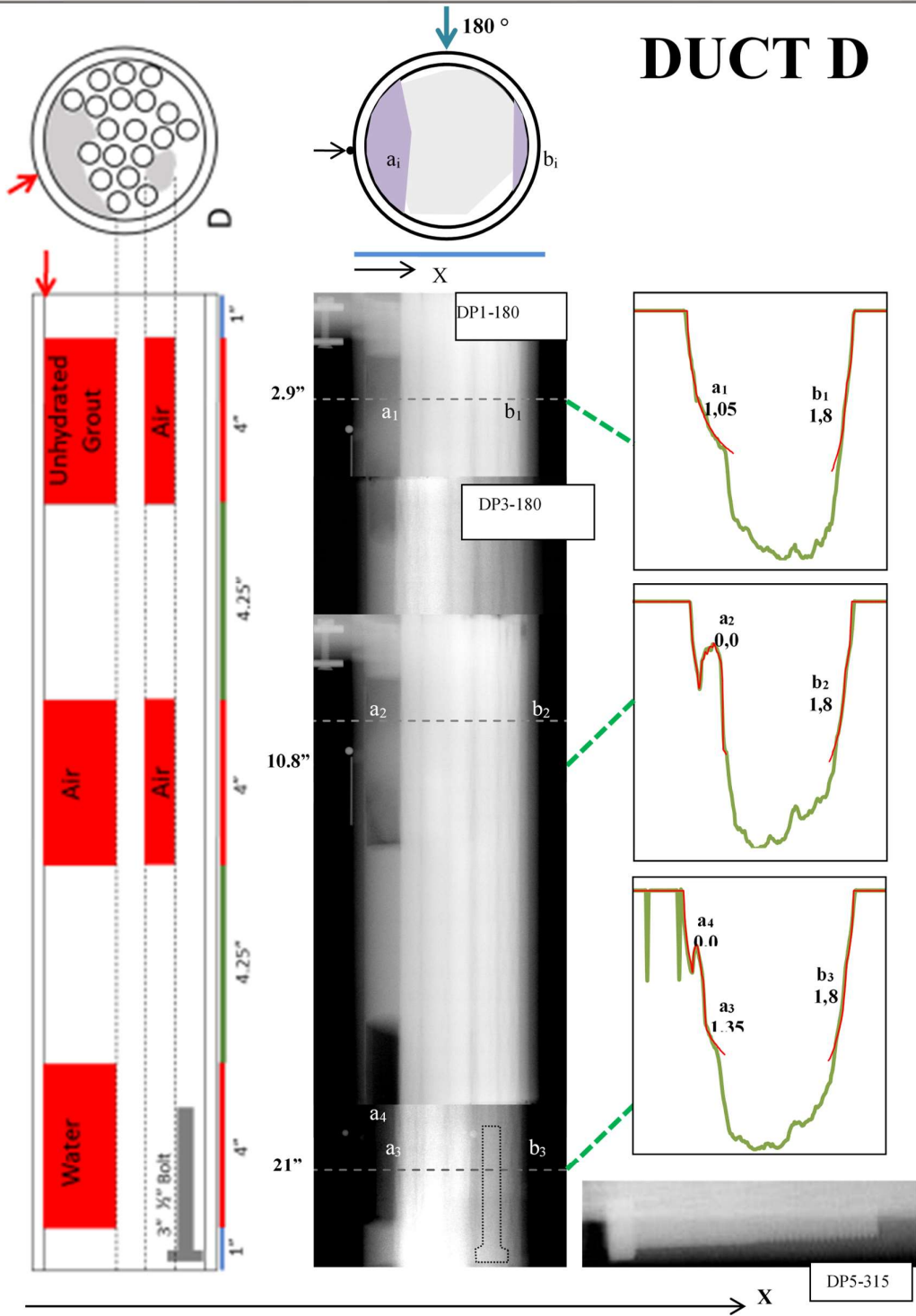
DUCT D

Fig. 13. Results for Duct D. Left: USF construction drawings; Center and right: Results of measurements performed by THASA, (gray indicate tendon location; purple, areas of measured grouting defects, see text). Green spikes in the lowest plot correspond to reference marks used in the measurements.

CONCLUSIONS

The purpose of the present work was to provide a validation test of measurements performed using the Tendon Imaging Sensor developed by USF. To this end we applied THASA´s RCT (Reinforced Concrete Tomography) methodology, based on the analysis of gamma-ray images obtained by exposing the samples to radiation from a radioactive source. This technique effectively yields a measure of thickness times density of the material traversed by the gamma rays.

The gamma-ray images were analyzed following a two step process: 1) performing tomographies to locate both the tendon and the grouting defects, and 2) least squares fitting of gamma-ray intensity profiles of selected sections to determine density values where grouting defects were identified. Grouting densities in the interstices between the strands were not measured.

Results are compared with the construction drawing information provided by USF. The following conclusions can be drawn:

1) The gamma-ray imaging technique applied in the present work has been shown to be an effective tool to check results obtained with other methods, such as the one developed by USF, to determine grouting defects in PT ducts. In addition, the technique allows observation of details with photographic fidelity, such as individual strands, foreign elements (bolts) and small air bubbles as in the present case.
2) The tendon and grouting defect distributions obtained through THASA tomographic analysis is in accordance with those shown in the USF drawings.
3) We do not detect density differences between "soft" and "sound" grout.
4) Small voids in areas designated as "water" in the drawings were found, probably due to incomplete water filling of the samples after arrival at our premises.
5) There is some doubt as to the agreement between density measurements and drawings in connection to the areas designated as "unhydrated".

ADDENDUM

to

Report on

Gamma Ray Tomography Validation Test of

Mock Up Tendons

of May 2019

Federal Award No. TWO 977.24
Subawards No. 2104-1245-00-A
Project Title:
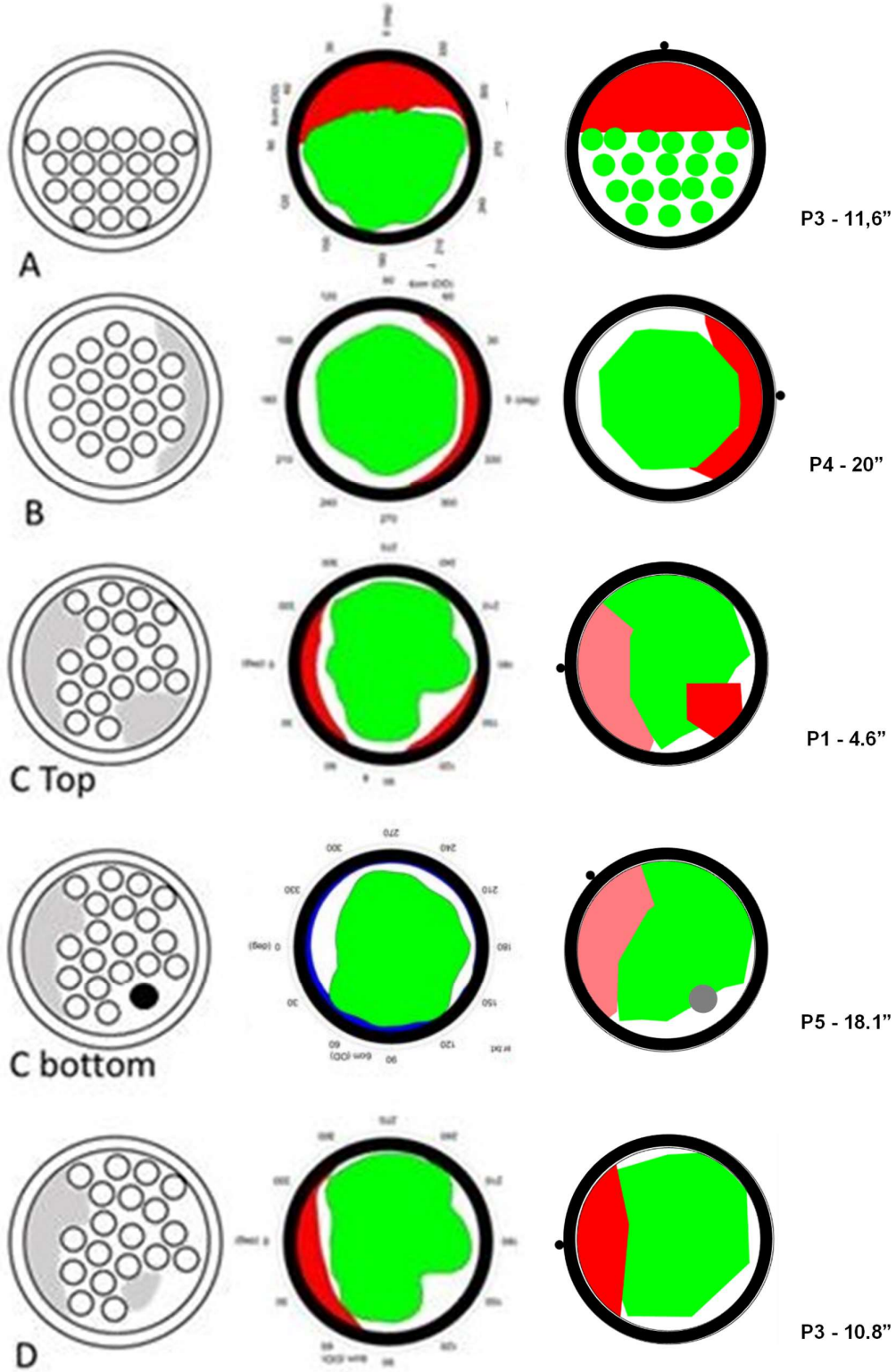Development of Tendon Imaging Sensor.

June 2019

ADDENDUM

The present document complements THASA´s report on "Gamma Ray Tomography Validation Test of Mock Up Tendons provided by the University of South Florida" issued in May 2019, and its purpose is to facilitate the comparison between THASA´s results and those obtained by Prof. Alberto A. Sagues and his collaborators who applied a new sensor developed at their laboratory for the inspection of external PT ducts,

The comparison is shown in the figure next page where cut views of selected sections of the duct designs (left hand side), USF sensor´s results (central column) and THASA´s results (right hand side) are exhibited.

The cut views shown here are only a selection of the many sections studied in the five duct samples labelled A, B, C and D. The sections are identified as PX D" where PX (X = 1, 2, 3, 4 and 5) is the section indicated on the sample surfaces and D" is the distance from the top end of each sample (next to P1).

The gammagraphic method only measures densities. These are indicated in the figure with colors: green denotes strands; red, void (density close to 0 g/cm^3); pink, density near 1 g/cm^3 (such as water); and no color means good grout (approx. 1.8 g/cm^3). These results were obtained using the methodology described in the Report and involved 155 gammagraphies and the corresponding analysis.

It must be pointed out that, as explained in the Report, the full tomography of individual strands was worked out in the case of Duct A. For the other ducts, only the area occupied by the whole tendon was determined.

A

B

C Top

C bottom

D

P3 - 11,6"

P4 - 20"

P1 - 4.6"

P5 - 18.1"

P3 - 10.8"

strand ● bolt density 0 g/cm³ density 1-1.1 g/cm³

128